Expanding the fracture limits in bulk metal forming to biaxial tension states

Rui Filipe Vieira Sampaio

Thesis to obtain the Master of Science Degree in

Mechanical Engineering

Supervisors: Prof. Carlos Manuel Alves da Silva
                  Prof. Ivo Manuel Ferreira de Bragança

Examination Committee

Chairperson:	Prof. Rui Manuel dos Santos Oliveira Baptista
Supervisor:	Prof. Carlos Manuel Alves da Silva
Members of the Committee:	Prof. Chris Valentin Nielsen
	Prof. Paulo António Firme Martins

November 2021

We favor the simple expression of the complex thought.

Mark Rothko

Resumo

Os limites de enformabilidade na massa nos planos das extensões principais e da triaxialidade são caracterizados por uma região de incerteza na qual fissuras podem ser desencadeadas por tração (modo I) ou corte fora-do-plano (modo III). A obtenção de dados experimentais nesta região é um problema há muito conhecido, pelo que esta dissertação tem como objetivo principal a apresentação de uma nova geometria para um provete de massa que possa efetivamente contribuir para a caracterização dos limites de enformabilidade na massa em estados de tração biaxial, completando a caracterização destes limites para toda a gama de estados de tensão nos quais ocorra fratura em superfícies livres. Além disso, esta dissertação apresenta uma expressão analítica para a transformação da curva limite de enformabilidade à fratura no modo III (OSFFL) no plano das extensões principais numa curva hiperbólica de limite à fratura no plano da triaxialidade. A metodologia utilizada combina experimentação com modelação analítica e numérica. Esta dissertação representa um avanço no sentido de reduzir a atual falta de conhecimento sobre a fissuração de peças obtidas por deformação plástica na massa sujeitas a valores de triaxialidade para lá da tração uniaxial. Os resultados mostram que um novo critério de dano dúctil não-acoplado construído sobre a combinação das funções integrandas dos critérios de dano de Cockcroft-Latham normalizado e de McClintock pode ser usado com sucesso para modelar os limites à fratura na deformação plástica na massa para toda a gama de valores de triaxialidade correspondente à iniciação de fraturas em superfícies livres.

Palavras chave: Enformabilidade na Massa, Tração Biaxial, Mecânica da Fratura Dúctil, Mecânica do Dano, Trabalho Experimental, Método dos Elementos Finitos.

Abstract

Bulk formability limits in the in-plane principal strain space and in the space of effective strain vs. stress triaxiality are characterized by an uncertainty region in which cracks may be triggered by tension (mode I) or by out-of-plane shear (mode III). The obtainment of experimental data in this region is a long-known problem, hence this thesis has as main objective the presentation of a new upset bulk formability test geometry that can effectively contribute to the characterization of the formability limits of bulk metal forming in states of biaxial tension, completing the characterization of these limits for the whole range of stress states in which cracking on free surfaces may occur. Moreover, this thesis also presents an analytical expression for transforming the fracture forming limit line for mode III (OSFFL) in the in-plane principal strain space into a hyperbolic fracture limit curve in the effective strain vs. stress-triaxiality space. The overall utilized methodology combines experimentation together with analytical and numerical modelling. This thesis is a step towards reducing the current lack of knowledge regarding failure by fracture in bulk metal forming parts subject to stress triaxiality values beyond uniaxial tension. Results show that a new uncoupled ductile damage criterion built upon the combination of the integrands of the normalized Cockcroft-Latham and the McClintock damage criteria can be successfully used to model the physics of bulk metal forming limits to fracture for the entire range of stress triaxiality values corresponding to fracture initiation on free surfaces.

Keywords: Bulk Formability, Biaxial Tension, Ductile Fracture Mechanics, Damage Mechanics, Experimentation, Finite Element Method.

Acknowledgements

Contents

List of figures

List of tables

Nomenclature

Abbreviations and acronyms

AA	Aluminum Association
AISI	American Iron and Steel Institute
CNC	Computer Numeric Control
EDS	Energy dispersive X-ray spectrometer
FEM	Finite Element Method
FFL	Fracture forming limit line
FFLD	Fracture forming limit diagram
FLC	Forming limit curve
FLD	Forming limit diagram
OSFFL	Out-of-plane shear fracture forming limit line
SEM	Scanning electron microscope
SFFL	In-plane shear fracture forming limit line

Symbols

Latin symbols

A, B, C, C_i	Material constants used in uncoupled ductile damage criteria
d	Average void diameter, or minor specimen diameter
D	Major specimen diameter
D_{crit}	Critical value of damage for the mode I of fracture mechanics
D_i	Barreled ring specimen inner ellipse diameter
D_n	Ductile damage variable according to Lemaitre
D_{crit}^i	Critical ductile damage according to a generic i criterion
D_{crit}^s	Critical value of damage for the mode II of fracture mechanics
D_{crit}^{ts}	Critical value of damage for the mode III of fracture mechanics
E	Elastic modulus
$\tilde{E}$	Elastic modulus of the damaged material
f_v	Void volumetric fraction
g	Nondimensional weighting function
h	Barreled ring specimen inner ellipse height
H	Specimen height
I_1	First invariant of the stress tensor
J_1, J_2, J_3	First, second, and third invariants of the deviatoric stress tensor
k	Shear flow stress
l	Inter-hole spacing, or square grid line height after deformation
l_0	Square grid line height prior to deformation
m	Friction factor
$O(x)$	Order of magnitude of x
r	Anisotropy factor
$\bar{r}$	Normal anisotropy
r_α	Anisotropy factor at a degree α
R_a	Average roughness
t	Thickness
w	Square grid line width after deformation

w_0	Square grid line width prior to deformation
w^e	Elastic damage strain energy release rate
w_d^e	Elastic damage strain energy release rate due to distortional effects
w_H^e	Elastic damage strain energy release rate due to dilatational effects
w^p	Total plastic work per unit volume

Greek symbols

α	Ratio between the intermediate and major principal stresses
β	Slope of a general proportional strain loading path
γ	Shear strain
δ_{ij}	Kronecker delta
$\bar{\varepsilon}$	Effective strain
$\bar{\varepsilon}_0$	Damage initiation strain
$\varepsilon_1, \varepsilon_2, \varepsilon_3$	Principal strain components
$\bar{\varepsilon}_f$	Effective strain at fracture
ε_{zf}	Strain at fracture in the direction of compression
$\varepsilon_{\theta f}$	Strain at fracture in the azimuthal direction
η	Stress triaxiality
θ	Lode angle
$\bar{\theta}$	Normalized Lode angle
μ	Lode coefficient (or Lode's stress parameter)
ν	Poisson's ratio
ξ	Lode angle parameter (or normalized third deviatoric stress invariant)
σ	Normal stress
$\bar{\sigma}$	Effective stress
$\sigma_1, \sigma_2, \sigma_3$	Principal stress components
$\sigma_1, \sigma_2, \sigma_t$	Principal in-plane (on-surface) stresses and through-thickness stress
σ_m	Average or hydrostatic stress
σ_r	Radial stress component
σ_z	Longitudinal stress component
σ_θ	Azimuthal stress component

$\sigma_1',\ \sigma_2',\ \sigma_3'$	Principal deviatoric stress components
σ_{ij}'	Deviatoric stress tensor
τ	Shear stress
τ_{12}	In-plane shear stress
τ_f	Friction shear stress
τ_{max}	Maximum shear stress
τ_{ti}	Out-of-plane shear stress
ψ	Ductile damage variable according to Kachanov

Chapter 1

Introduction

In order to achieve a reduction in both resource consumption and manufacturing costs, there is a constant need to improve existing manufacturing processes. This improvement must be complemented with an enhancement in material characterization to completely understand their behavior when loaded. In the case of metal forming processes, the characterization of formability limits is extremely important for this to be achieved.

The concept of formability is usually defined as the maximum level of plastic deformation that a given material can withstand during a technological process of plastic deformation without the occurrence of defects such as plastic flaws, necking, or cracking (Rodrigues and Martins, 2010). Formability is hence characterized by the formability limits, which in bulk metal forming are typically defined to fracture. In most bulk forming processes, fracture is something to avoid at all costs, however it may not be an undesirable outcome for certain processes, such as blanking, piercing, or fine blanking – although the workpieces in these processes are typically sheets, they are treated as bulk, since plastic deformation occurs in a very localized way.

Fracture in bulk forming can occur internally (e.g., central bursts, or chevrons, in extrusion) or on the surface (e.g., edge cracking in forging) (Nielsen and Martins, 2021). This thesis focuses on tackling free surface cracks, therefore taking advantage of plane stress conditions.

Surface fracture initiation may occur according to one of three different ways, corresponding to the three crack opening modes of fracture mechanics: crack opening by tension (mode I), by in-plane shear (mode II), or by out-of-plane shear (mode III). The fracture forming limits consist of the combination of three lines that respectively correspond to these crack opening modes: the fracture forming limit line (FFL), the in-plane shear fracture forming limit line (SFFL), and the out-of-plane shear fracture forming limit line (OSFFL).

In bulk metal forming, fracture initiation can only occur by mode I or mode III (Martins et al., 2014), and the fracture forming limits are characterized exclusively for stress states ranging from uniaxial compression to through-thickness plane strain. However, some manufacturing processes may induce biaxial tensile stress states in certain regions of the workpiece, and this calls for a full characterization of the fracture forming limits in bulk metal forming for stress states compatible with plane stress conditions, i.e., from uniaxial compression to equibiaxial tension.

Experimental results in bulk formability show that the FFL may not always be present, meaning that the material may or may not fracture by tension, depending on the material itself or on its

temperature (Erman et al., 1983), conjecturing the existence of an 'uncertainty region' in which mode I and mode III compete between themselves.

If only the OSFFL is present, the values of effective strain at fracture may be replicated only by the normalized Cockcroft-Latham ductile damage criterion (associated with fracture by out-of-plane shear – mode III). If also the FFL is present, these values can only be replicated with a combination of the latter and the McClintock ductile damage criterion (associated with fracture by tension – mode I). The utilization of a single, rather than dual, criterion for the characterization of the fracture forming limits in bulk forming would be preferable for the metal forming industry, as only one expression would be necessary.

Therefore, the two main objectives of this thesis are: (1) the development of a bulk test specimen that allows for fracture initiation under biaxial tension states in plane stress conditions and on a non-covered surface, allowing for the utilization of a digital image correlation (DIC) system; and (2) the development of a single uncoupled ductile damage criterion for bulk metal forming built on the concept of fracture mode competition that dismisses the utilization of a second criterion for the characterization of the previously referred range of stress states. Additionally, an analytical expression for the shifting from the in-plane principal strain space to the space of effective strain vs. stress triaxiality in mode III is also for the first time derived.

This thesis is divided into 6 different chapters, being the present one the first.

Chapter 2 presents the state of the art in bulk formability. Starting with the concept of ductile fracture and the description of the three crack opening modes, the chapter is highly dedicated to the theory of ductile damage mechanics, focusing above all on uncoupled ductile damage criteria and the formulation of the theoretical fracture forming limits based on those. Notwithstanding, coupled damage criteria and the basic concepts of continuum damage mechanics are also introduced. The chapter includes the tests and methodologies to characterize the fracture forming limits in bulk metal forming and discusses the Lode parameters and their importance on uncoupled ductile damage criteria, since the utilization of these has been growing in the past decades. The chapter ends with a summary of the shortcomings in bulk formability, evidencing the importance of the aim of this thesis.

The theoretical development is detailed in Chapter 3. The shortcomings presented in the previous chapter are tackled: (1) a novel bulk test specimen for states of biaxial tension is developed; and (2), starting with the derivation of an analytical expression for the shifting from the in-plane principal strain space to the space of effective strain vs. stress triaxiality in mode III, a new uncoupled ductile damage criterion for the replication of values for effective strain at fracture through the whole range of stress triaxiality values compatible with plane stress is introduced. The chapter ends with the presentation of the calculations necessary for the calibration of different uncoupled ductile damage criteria, which are implemented into an Excel workbook.

Chapter 4 presents the experimental work performed, including a brief description of the utilized testing equipment and methodologies, the mechanical characterization of the material, and the experimental work plan of upset bulk formability test specimens utilized for the characterization of the formability limits.

Chapter 5 presents the experimental results and a discussion on those. First, with the FFL and the OSFFL adjusted to best fit the experimental values, the formability limits are shown in the in-plane principal strain space along with the strain loading paths up to fracture, and in the space of effective strain at fracture vs. stress triaxiality. Then, fractographies of the fracture surface morphology obtained with the new test specimen are presented along with a finite element method-predicted fracture initiation and propagation, and a discussion on the present crack opening mode is made.

Chapter 6 is the final chapter, presenting the main conclusions that can be withdrawn from the obtained results, along with possible future work that may follow the one already developed for this thesis.

Additionally, two appendices are also provided. Appendix A presents a detailed theoretical formulation of the FFL, the SFFL, and the OSFFL. Appendix B presents the detailed formulation of the various Lode parameters and their relation to stress triaxiality, the normalized maximum shear stress, and the normalized major principal stress component.

Chapter 2

State of the art in bulk formability

Nowadays, manufacturing technologies represent a highly important agent in the reduction of energy consumption and, consequently, in ecological preservation and protection, either through energy saving policies that can be adopted during the production phase, or through the manufacture of increasingly lighter components. When used in the transportation industry, these lighter components lead to a reduction in fossil fuel spending and a consequent reduction in carbon emissions from the vehicles themselves (Tekkaya, 2018). In fact, most of these emissions come from the material transformation phase. For example, life cycle analyzes of motor vehicles have determined that this phase represents about 78 to 86% of the whole carbon dioxide emissions (Zamel and Li, 2006).

These new and increasingly demanding needs employed in the manufacturing processes lead to a special need for a better characterization of the processes and materials' limits in order for one to be able to optimize the former.

2.1 Ductile fracture and the mechanics of void growth

As mentioned in the introduction, formability represents the maximum level of deformation that is achievable during a technological process of plastic deformation without the development of defects such as plastic flaws (regions of intense plastic shearing), necking, or cracking (Rodrigues and Martins, 2010). This way, the definition of formability limits is something of extreme importance for any plastic deformation process, allowing to understand if the desired deformation for the manufacture of a given part can be achieved without compromising the material's integrity, favoring a reduction in the number of defective parts and a consequent optimization of the technological processes.

The formability of a given material is characterized by its formability limits, which can be controlled by necking or by fracture. The formability limits by necking are only used in sheet forming, while the formability limits by fracture are used in both sheet and bulk metal forming.

Although fractures may be classified as brittle or ductile, the formability limits to fracture are essentially defined reckoning initiation and propagation of ductile cracks that develop inside or on the surface of parts due to an accumulation of damage in highly deformed regions, either by extensive overall material flow or localised material flow induced by the tools.

Plastic deformation at the grain boundaries or in the vicinity of inclusions or hard secondary-phase particles can lead to the nucleation of voids, and to a gradual growth of those and others that may have already existed prior to the deformation. These voids are regions in the material structure with high stress concentration, which leads to higher deformation rates (and consequent greater damage) than in the rest of the material (Nielsen and Martins, 2021). The continued growth of these voids to a dimension in the order of magnitude of the distance that separates them leads to an eventual coalescence between adjacent voids, creating microscopic cracks that, with continuing deformation, turn to macroscopic cracks (Figure 2.1). Figure 2.2 shows images obtained with a scanning electron microscope (SEM) of the deformation under tension and shear of 15–50 μm laser-drilled holes to emulate the growth and coalescence mechanism of voids under such stress states as it is schematically represented in Figure 2.1.
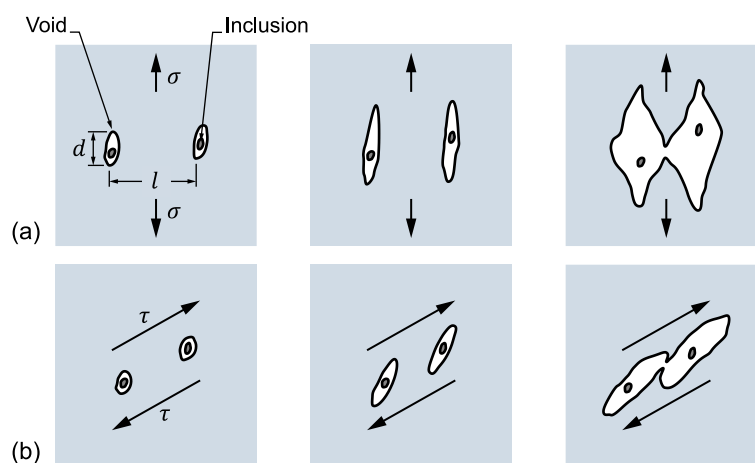
Figure 2.1 Schematic representation of the nucleation, growth, and coalescence mechanism of voids formed under (a) tensile and (b) shear stresses.
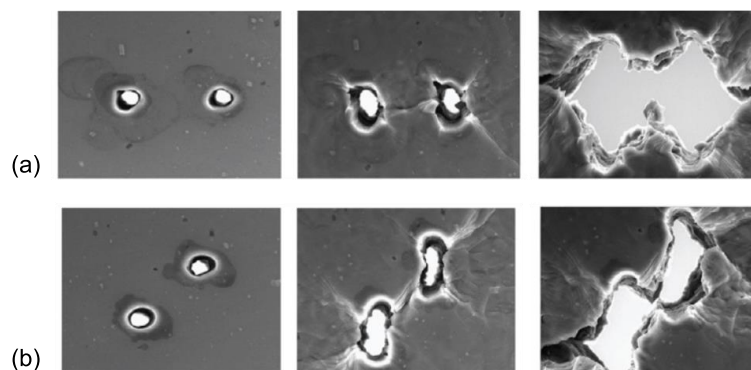
Figure 2.2 SEM images of the deformation sequence of laser drilled holes emulating the growth and coalescence mechanism of voids under (a) tensile and (b) shear stresses
(adapted from Weck and Wilkinson, 2008).

While proposing a fracture criterion based on the mechanics of void growth by tension (Figure 2.1a and Figure 2.2a), McClintock (1968) came to a conclusion that led Atkins and Mai (1985) to relate the ratio between the initial inter-hole spacing, l, and the initial average diameter of a void, d, with the stress triaxiality, $\eta = \sigma_m / \bar{\sigma}$, as follows:

$$\ln\left(\frac{l}{d}\right) \approx \int_0^{\bar{\varepsilon}} \frac{\sigma_m}{\bar{\sigma}} d\bar{\varepsilon} \tag{2.1}$$

Following a similar approach, and aiming to model growth and coalescence of voids under in-plane shear stresses, τ (Figure 2.1b and Figure 2.2b), Christiansen et al. (2016) proposed another relation that takes shear strain, γ, into account.

$$\ln\left(\frac{l}{d}\right) \approx \int_0^{\gamma} \frac{1}{3} d\gamma + \int_0^{\gamma} \frac{\sigma_m}{2\tau} d\gamma \tag{2.2}$$

In fact, the original work by McClintock (1968) showed a shear-related influence on void growth, but simplifications in his conclusions led to an expression that allowed Atkins and Mai (1985) to write the expression in equation (2.1). Nevertheless, equations (2.1) and (2.2) bring forth the realization that modelling void growth and coalescence subjected to tensile and shear stresses, requires for both dilatational effects related to stress triaxiality, and distortional effects related to shear stress to be considered. Moreover, these equations explain that as the l/d ratio increases (because of either smaller voids or greater separation between them), the degree of plastic deformation that the material can bear (the right-hand sides of the equations) also increases.

2.1.1 Ductile fracture and the three crack opening modes

In metal forming processes in which the intended purpose is not to cut material, arising fractures must be avoided, the conditions of which depend on the circumstances of crack development, on local stress and strain states, and on the ductile damage that develops in the material's micro-structure (Silva et al., 2015). In bulk forming, fracture can occur internally (e.g., extrusion central bursts, or chevrons) or on the surface (e.g., edge cracking in forging) (Nielsen and Martins, 2021).

On the surface, the type of fracture to appear is the product of a competition between the accumulation of the microstructural damage necessary for fracture to occur due to tensile stresses, in-plane shear stresses, or out-of-plane (or through-thickness) shear stresses, (Figure 2.3) each relating, respectively, to modes I, II, and III of fracture mechanics (Martins et al., 2014).
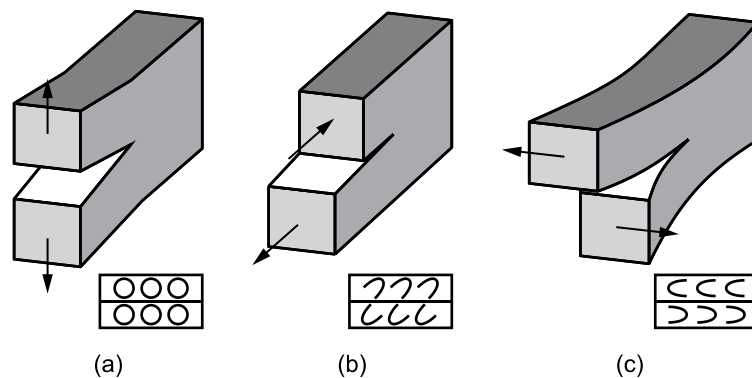
Figure 2.3 Crack opening modes and schematic representation of the respective surface morphology for (a) mode I – tensile stresses, (b) mode II – in-plane shear stresses, and (c) mode III – out-of-plane shear stresses (adapted from Nielsen and Martins, 2021).

The observation of the fracture surface morphology allows for a better understanding of the history of fracture initiation and propagation. The opening of cracks by tensile stresses (mode I of fracture mechanics) leads to the appearance of circular dimple structures, while by shear stresses it leads to the appearance of parabolic and elongated dimples that point in the same direction of crack propagation (mode II of fracture mechanics) or are rotated with respect to that same direction (mode III of fracture mechanics) (Figure 2.3).

A way to represent the formability limits by necking is to represent the forming limit curve (FLC) in the forming limit diagram (FLD) and by fracture the fracture forming limit line (FFL) in the fracture forming limit diagram (FFLD), where the locus of strain pairs at which necking or fracture initiation occurs are plotted in the in-plane principal strain space as $\varepsilon_1 = f(\varepsilon_2)$ (Figure 2.4). This diagram was initially proposed by Keeler (1968) for biaxial states of tension in sheet forming and extended to states of tension-compression by Goodwin (1968). Later, the FFLD was adapted to bulk forming processes by Kuhn et al. (1973), using in the axes the tensile and compressive strains on the outer surface of the test specimen, where plane stress states are present.

As necking is not experienced during manufacturing processes of bulk metal forming and, even in sheet forming, fracture and necking are likely to interact, henceforth this representation will only be referred to as the forming limit diagram, FLD.

Although approaches to treat sheet and bulk forming together have been made (Bao and Wierzbicki, 2004), it is wiser to treat them independently, as they present differences in plastic flow due to the conditions of plane stress found in sheet forming and three-dimensional stress found in bulk forming (Martins et al., 2014).
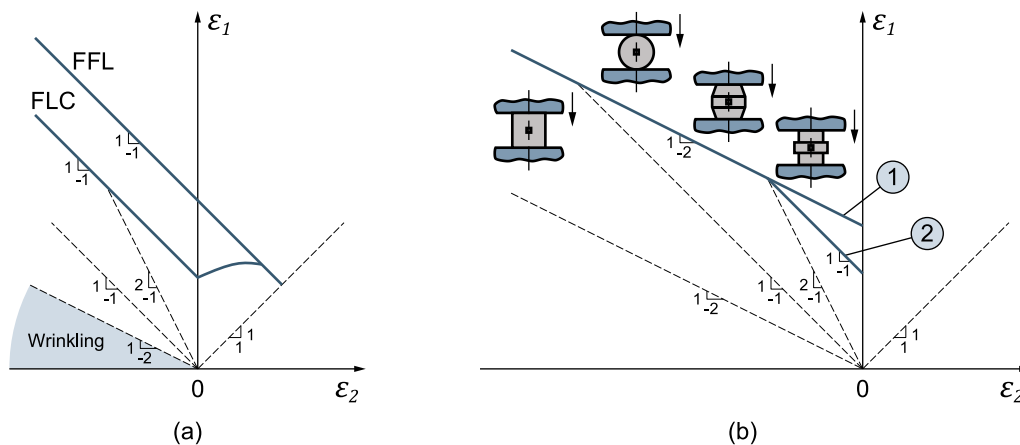
Figure 2.4 FLD for (a) sheet forming, showing the interaction between the forming limit curve (FLC) and the fracture forming limit line (FFL), and (b) bulk forming, showing the linear fracture locus (1) and the bilinear fracture locus (2) with two different slopes ('-1/2' and '-1') (adapted from Martins et al., 2014).

For the case of bulk forming, results obtained by Kuhn et al. (1973) have shown that the fracture locus in tensile, rolled, and cylindrical upset specimens fall on a straight line of slope '-1/2' (represented by (1) in Figure 2.4b and parallel to the loading path of uniaxial compression). Since both the vertical and the inclined cracks found on the outer surface do not run radially in the

specimen, one can easily perceive them as a result of shear, as it was stated by Kobayashi (1970). Later, results by Erman et al. (1983) showed a bilinear fracture locus in bulk forming resulting from the combination of the previously mentioned '-1/2' sloped line and another of slope '-1' (represented by (2) in Figure 2.4b and parallel to the pure shear loading path) to which vertical cracks are associated to. Above these lines, the material is expected to fail by fracture.

2.2 Ductile damage criteria and the development of the forming limit diagram

One of the first approaches to study the limits of formability consists of studying the deformation-zone, a result of process-dependent parameters that control the formability itself, and which wields a strong influence upon homogeneity of material flow, internal porosity, and tendency to open cracks during material processing (Nielsen and Martins, 2021). This approach derived from the slip line field theory with the work by Sachs et al. (1931) and was later thoroughly studied in the work by Caddell and Atkins (1968), in which the influence of the deformation-zone geometry was characterized by means of the deformation-zone geometry parameter, a ratio that relates the mean thickness of the workpiece with the contact length between the latter and the tool.

The assessment of damage accumulation considering, simultaneously, stresses and strains is achieved using damage criteria. In fact, the theory of ductile damage mechanics has been used for a long time to predict the onset of fracture in metal forming processes. This approach was first proposed by Freudenthal (1950) when creating a ductile damage criterion based on the total plastic work per unit volume, w^p.

A few years later, Kachanov (1958) proposed an alternative that eventually led to what is now known as continuum damage mechanics and, since then, several damage criteria have been proposed throughout the years, which can be essentially grouped into two main groups: coupled and uncoupled damage criteria.

2.2.1 Coupled damage criteria

Coupled damage criteria can be built upon a microstructure- or macroscopic perspective-based approach to continuum damage mechanics. In these approaches, the weighting functions used, and whose integrations lead to the damage value, are generally non-dimensional and dependent on the stress-state.

In coupled damage criteria, the accumulation of damage during plastic deformation leads to softening effects that influence the stress and strain values at the onset of fracture (Nielsen and

Martins, 2021). This damage dependence on the deformation itself makes the implementation of these models in existing finite element programs quite complicated.

Micromechanical-based approaches consider a uniform void distribution in a homogeneous material, so that porosity can be evaluated according to a void volumetric fraction, f_v. The first approaches in this field, and from which many other damage criteria are derived, were the yield criterion for porous materials by Shima and Oyane (1976) and the damage criterion proposed by Gurson (1977) (later modified by Tvergaard, 1981, and then by Tvergaard and Needleman, 1984, originating in the Gurson-Tvergaard-Needleman, or GTN, criterion), which use the volumetric void fraction, or parameters derived from it, to assess the stress state at the onset of fracture and to build the constitutive equations according to the criteria. In fact, this series of modifications to the original Gurson criterion led to a differentiation in the group of micromechanics-based damage criteria between the ones that derive from yield criteria for porous materials and the others that are built upon the GTN criterion, almost creating two distinct groups inside the micromechanics one.

Macromechanics-based criteria utilize a damage variable, ψ, that varies between 0 and 1 to assess the damage in a given material under plastic deformation. According to Kachanov's (1958) creep rupture-based damage criterion, this variable's value is equal to 1 for a material in the undamaged state, decreasing until the moment of fracture, when it becomes 0 – if we take into account the definition proposed by Lemaitre (1985) in his damage criterion based on microcracks' initiation and evolution and voids' growth and coalescence, the value of the damage variable, represented by D_n, is 0 for the undamaged state and 1 at fracture. Therefore, according to the theory of continuum damage mechanics that is born out of these two criteria, we have that the elastic modulus of the damaged material, $\tilde{E}$, can be written as:

$$\tilde{E} = E\psi = E(1 - D_n)$$

$$\psi = 1 - D_n = \frac{\tilde{E}}{E}$$

(2.3)

where E is the elastic modulus of the undamaged material. This way, it is then possible to determine the damage evolution through the characterization of the elastic modulus during plastic deformation (Figure 2.5).
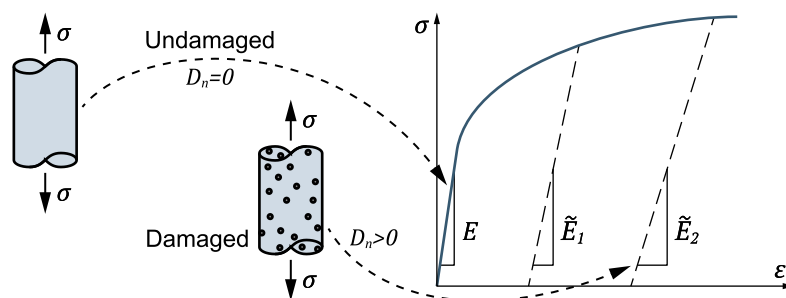
Figure 2.5 *Schematic representation of the variation of the elastic modulus, E, with the accumulation of damage according to continuum damage mechanics (adapted from Lemaitre and Chaboche, 1985).*

It is worth noting that Lemaitre's (1985) model also considers an elastic damage strain energy release rate, w^e, (2.4) to characterize fracture initiation that contemplates both distortional, w_d^e, and dilatational effects, w_H^e, the latter accounting for stress triaxiality, η. Yet, this criterion is mostly suitable for stress states with little effect of shear.

$$
\begin{aligned}
w^e = w_d^e + w_H^e &= \frac{1+\nu}{E} \frac{\sigma'}{1-D_n} + \frac{1-2\nu}{E} \frac{\sigma_m}{1-D_n} \\
&= \frac{\bar{\sigma}}{2E(1-D_n)} \left[\frac{2}{3}(1+\nu) + 3(1-2\nu)\eta^2 \right]
\end{aligned}
\tag{2.4}
$$

where ν is the Poisson's ratio and σ', $\bar{\sigma}$, and σ_m are the deviatoric, effective, and average stresses.

Nevertheless, since the analysis of coupled damage criteria is out of the scope of this work, this topic will not be detailed further.

2.2.2 Uncoupled damage criteria

Uncoupled damage criteria are simpler, when compared to coupled ones, for they are just weighted integrations of the effective plastic strain (Atkins, 1996), being possible to write a generalized formula for this type of criteria as:

$$
D_{crit} = \int_0^{\bar{\varepsilon}_f} g \, d\bar{\varepsilon}
\tag{2.5}
$$

where g is a nondimensional weighting function that corrects the accumulated value of effective strain at fracture, $\bar{\varepsilon}_f$, as a function of the strain loading path. Because of the phenomenological link of ductile damage to the critical size of voids at the time of coalescence introduced by McClintock (1968) and described in Section 2.1, uncoupled ductile damage criteria rely on this correction of the effective strain at fracture. Additionally, if there is a threshold strain, $\bar{\varepsilon}_0$, below which damage is not accumulated, called the damage initiation strain, the lower limit of the integral in equation (2.5) becomes $\bar{\varepsilon}_0$ rather than zero.

One of the first attempts to predict the onset of cracking was made by Freudenthal (1950), who suggested a damage criterion in which the critical value of ductile damage equals the total plastic work per unit volume, w^p, at fracture:

$$
D_{crit}^{Fr} = \int_0^{\bar{\varepsilon}_f} \bar{\sigma} \, d\bar{\varepsilon} = (w^p)_f
\tag{2.6}
$$

The main critique to Freudenthal's (1950) criterion is that it makes no distinction between tensile or compressive stresses. As a matter of fact, it was shown by Vujovic and Shabaik (1986) that the effective strain at fracture, $\bar{\varepsilon}_f$, reduces as stress triaxiality, η, goes from negative to positive values, and thus with the increase of hydrostatic tension.

More commonly, uncoupled damage criteria are used to predict the onset of cracking by exploiting the theory of void growth mechanics under tension (2.1) and shear (2.2). Cockcroft and Latham (1968) proposed a purely empirical ductile damage criterion by making the nondimensional weighting function equal to the major principal stress, $g = \sigma_1$, evidencing the tensile stress's importance in void growth:

$$D_{crit}^{CL} = \int_0^{\bar{\varepsilon}_f} \sigma_1 \, d\bar{\varepsilon} \tag{2.7}$$

Nevertheless, from the void growth point of view and because of the left-hand sides of equations (2.1) and (2.2), it is more reasonable to include dimensionless stresses, so that one can consider stress triaxiality, typical of the void growth theory introduced by McClintock (1968). Because of this, Oh et al. (1979) proposed a normalized version of the Cockcroft and Latham (1968) criterion:

$$D_{crit}^{NCL} = \int_0^{\bar{\varepsilon}_f} \frac{\sigma_1}{\bar{\sigma}} \, d\bar{\varepsilon} \tag{2.8}$$

Experimental data shows that materials with limited formability can be successfully deformed under high hydrostatic pressures. So, for a given material, temperature, and strain rate of deformation, formability is highly dependent of the hydrostatic stress, σ_m (Gouveia et al., 1996). Notwithstanding, the normalized version of the Cockcroft and Latham damage criterion has a good applicability for predicting the onset of surface cracks in bulk metal forming because it is essentially built on a 'hidden' out-of-plane shear-based condition, as it was concluded by Martins et al. (2014) and as it will be explained in Section 2.2.3.

By making the weighting function equal to the stress triaxiality, $g = \eta = \sigma_m/\bar{\sigma}$, one obtains the damage criterion proposed by Ayada et al. (1987), usually known as the McClintock (1968) damage criterion, for being a simplified version of the latter's work:

$$D_{crit}^{Mc} = \int_0^{\bar{\varepsilon}_f} \frac{\sigma_m}{\bar{\sigma}} \, d\bar{\varepsilon} \tag{2.9}$$

Many other criteria were developed following the uncoupled approach of Cockcroft and Latham (1968) and McClintock (1968). For example, Brozzo et al. (1972) empirically altered the Cockcroft and Latham (1968) criterion to account for an explicit dependance on the hydrostatic stress, σ_m, Rice and Tracey (1969) created an equation for the calculation of the critical ductile damage value considering a single spherical void, and Oyane (1972) formulated a damage criterion from the plasticity theory for porous materials and from microscopic observations of microcracks initiation and growth, considering that density decreases with void growth by tension.

Another approach is the one used by Tai and Yang (1987), where the weighting function is based on the elastic damage strain energy release rate proposed by Lemaitre (1985) to control crack initiation (2.10). A major problem in this criterion is that it was only tested for pre-notched tensile test specimens, thus shear conditions were not assessed.

$$D_{crit}^{TY} = \int_0^{\bar{\varepsilon}_f} \left[\frac{2}{3}(1+v) + 3(1-2v)\left(\frac{\sigma_m}{\bar{\sigma}}\right)^2 \right] d\bar{\varepsilon} \tag{2.10}$$

These uncoupled ductile damage criteria account for the major principal stress and/or the hydrostatic stress on crack opening, making them suitable for failure under tension (high triaxiality), but not so much for low stress triaxiality states, where shear effects are relevant (apart from the normalized Cockcroft-Latham criterion, for being based on a 'hidden' out-of-plane shear-based condition). Yet, more recently, Christiansen et al. (2016) proposed a criterion to overcome this, making use of equation (2.2). By multiplying the right-hand side of the equation by the normalized shear stress, $\tau/\bar{\sigma}$, one obtains the following:

$$D_{crit}^{Ch} = \int_0^{\gamma_f} \frac{\tau}{\bar{\sigma}} d\gamma + \int_0^{\gamma_f} \frac{3}{2} \frac{\sigma_m}{\bar{\sigma}} d\gamma \tag{2.11}$$

The first term in the right-hand side of equation (2.11) is related to the accumulation of damage caused by distortion due to shear, whereas the second one to the accumulation of damage caused by dilatation due to stress triaxiality, η.

Lou et al. (2012) chose to multiply the stress ratios related to distortional and dilatational void effects, resulting in the following criterion:

$$D_{crit}^{Lo} = \int_0^{\bar{\varepsilon}_f} \left(\frac{\tau}{\bar{\sigma}}\right)^A \left(\frac{\langle 1 + 3\,\sigma_m/\bar{\sigma}\rangle}{2}\right)^B d\bar{\varepsilon} \tag{2.12}$$

The Macaulay brackets used in equation (2.12) prevent the accumulation of damage when stress triaxiality, η, is below -1/3 (uniaxial compression), a stress state at which the criterion considers not to induce fracture while also avoiding void healing, where very low values of stress triaxiality would induce the accumulation of negative damage and, thus, material regeneration, which is mostly not realistic. A and B are material parameters to be identified.

Equation (2.13) presents another uncoupled approach, proposed by Işık (2018), that accounts for both dilatational and distortional effects on void growth. This criterion is further explored in Section 2.2.7. Again, A and B are material parameters to be identified.

$$D_{crit}^{I\c{s}} = \int_0^{\bar{\varepsilon}_f} \left[A\langle 1 + 3\eta\rangle + B\left(\frac{2\tau_{max}}{\bar{\sigma}} - 1\right) \right] d\bar{\varepsilon} \tag{2.13}$$

Table 2.1 provides an overview of the previously presented uncoupled damage criteria. For all the ones listed there, the procedure for determining the critical values, D_{crit}^i, compels experimental testing to obtain the strain values at fracture. Because assuming material regeneration would be mostly unrealistic for cold forming processes, none of these criteria should account for negative damage accumulation due to dilatational effects on void growth when $\sigma_m < 0$ ($\eta < -1/3$), thus the Macaulay brackets are implicitly considered for all of them (Nielsen and Martins, 2021).

As uncoupled ductile damage criteria are a function of the strain loading path, but do not alter or influence it in any way nor account for the progressive deterioration of the material due to the accumulation of damage, unlike coupled ones, they are of much easier implementation in existing finite element programs than the latter. Moreover, the definition and obtainment of material parameters from experimental data is also easier for the former.

Table 2.1 *Uncoupled ductile damage criteria used in metal forming processes.*

Freudenthal (1950)	$D_{crit}^{Fr} = \int_0^{\bar{\varepsilon}_f} \bar{\sigma} \, d\bar{\varepsilon}$
Cockcroft and Latham (1968)	$D_{crit}^{CL} = \int_0^{\bar{\varepsilon}_f} \sigma_1 \, d\bar{\varepsilon}$
Normalized Cockcroft and Latham (due to Oh et al., 1979)	$D_{crit}^{NCL} = \int_0^{\bar{\varepsilon}_f} \frac{\sigma_1}{\bar{\sigma}} \, d\bar{\varepsilon}$
Ayada et al. (1987) (after McClintock, 1968)	$D_{crit}^{Mc} = \int_0^{\bar{\varepsilon}_f} \frac{\sigma_m}{\bar{\sigma}} \, d\bar{\varepsilon}$
Rice and Tracey (1969)	$D_{crit}^{RT} = \int_0^{\bar{\varepsilon}_f} A \exp\left(\frac{3}{2}\frac{\sigma_m}{\bar{\sigma}}\right) d\bar{\varepsilon}$
Brozzo et al. (1972)	$D_{crit}^{Br} = \int_0^{\bar{\varepsilon}_f} \frac{2\sigma_1}{3(\sigma_1 - \sigma_m)} \, d\bar{\varepsilon}$
Oyane (1972)	$D_{crit}^{Oy} = \int_0^{\bar{\varepsilon}_f} \left(1 + A\frac{\sigma_m}{\bar{\sigma}}\right) d\bar{\varepsilon}$
Tai and Yang (1987)	$D_{crit}^{TY} = \int_0^{\bar{\varepsilon}_f} \left[\frac{2}{3}(1+\nu) + 3(1-2\nu)\eta^2\right] d\bar{\varepsilon}$
Lou et al. (2012)	$D_{crit}^{Lo} = \int_0^{\bar{\varepsilon}_f} \left(\frac{\tau}{\bar{\sigma}}\right)^A \left(\frac{\langle 1 + 3\,\sigma_m/\bar{\sigma}\rangle}{2}\right)^B d\bar{\varepsilon}$
Christiansen et al. (2016)	$D_{crit}^{Ch} = \int_0^{\gamma_f} \frac{\tau}{\bar{\sigma}} \, d\gamma + \int_0^{\gamma_f} \frac{3}{2}\frac{\sigma_m}{\bar{\sigma}} \, d\gamma$
Işık (2018)	$D_{crit}^{I\text{ş}} = \int_0^{\bar{\varepsilon}_f} \left[A\langle 1 + 3\eta\rangle + B\left(\frac{2\tau_{max}}{\bar{\sigma}} - 1\right)\right] d\bar{\varepsilon}$

2.2.3 Analytical formulation of the FLD based on fracture mechanics

In this section, the principal stress directions will be considered. However, to facilitate in terms of nomenclature, the in-plane principal stresses (acting tangent to the specimen's surface) will be called σ_1 and σ_2, but since the stress normal to the surface is always 0 on a free surface, it cannot be called σ_3, so it will rather be called $\sigma_t = 0$, even though it acts in a principal direction. This way, σ_1 and σ_2 are properly defined considering the solid mechanics definition ($\sigma_1 > \sigma_2$), but, although σ_t is a principal stress, it is not necessarily smaller or larger than the others (see Figure 2.6).
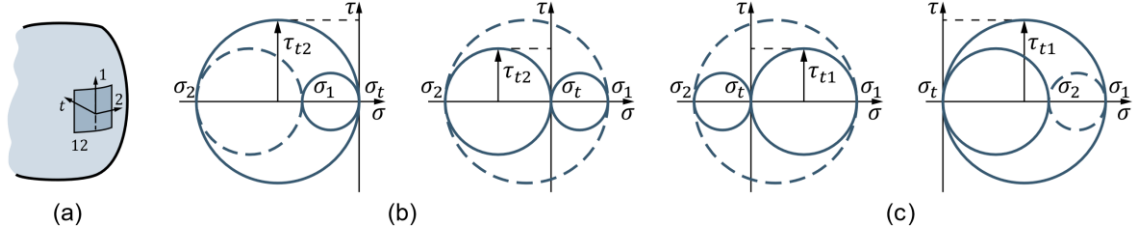
Figure 2.6 *Schematic representation of (a) the in-plane, or surface, plane (12) and the through-thickness direction, t, and of the Mohr circles for (b) compression dominated stress states, and (c) tension dominated stress states, evidencing the largest through-thickness shear stress, τ_{ti}. The dashed circles represent the in-plane stress state (on the specimen's surface).*

Following the analysis done by Martins et al. (2014), the mathematical formulation of the FLD is performed using the so-called McClintock damage criterion in equation (2.9). Expressing the integrand, $\sigma_m/\bar{\sigma}$, and the variable of integration, $d\bar{\varepsilon}$, in that same equation as the product of three partial ratios involving the strain increment $d\varepsilon_1$ and the stress σ_1 (to characterize the mode I of fracture mechanics), we get the following:

$$D_{crit} = \int_0^{\varepsilon_{1f}} \frac{\sigma_m}{\sigma_1} \frac{\sigma_1}{\bar{\sigma}} \frac{d\bar{\varepsilon}}{d\varepsilon_1} d\varepsilon_1 \qquad (2.14)$$

Using Hill's (1948) anisotropic yield criterion, assuming plane stress, $\sigma_t = 0$, and rotational symmetry anisotropy, $r_\alpha = r = \bar{r}$, equation (2.14) can be rewritten as follows:

$$D_{crit} = \int_0^{\varepsilon_{1f}} \frac{1+r}{3} (1+\beta) \, d\varepsilon_1 \qquad (2.15)$$

where $\beta = d\varepsilon_2/d\varepsilon_1$ is defined as the slope of a general proportional strain loading path.

Performing the integration in equation (2.15) and considering $\beta = cte.$, the critical value of damage can be rewritten as follows:

$$D_{crit} = \frac{1+r}{3} \left(\varepsilon_{1f} + \varepsilon_{2f} \right) \qquad (2.16)$$

If the lower limit in the integral in equation (2.15) was to be, rather than zero, the damage initiation strain, $\bar{\varepsilon}_0$, a threshold value of strain that represents a strain value below which no damage is accumulated, the critical value of damage for the mode I of fracture mechanics results in:

$$D_{crit} = \frac{1+r}{3} \left[\varepsilon_{1f} + \varepsilon_{2f} - (1+\beta)\varepsilon_0 \right] \qquad (2.17)$$

Equations (2.16) and (2.17) can be plotted in the in-plane principal strain space, $\varepsilon_1 = f(\varepsilon_2)$, as it is schematically presented in Figure 2.7a. From this representation, we can see that the critical value of the McClintock damage criterion is a straight line with slope '-1', agreeing with the experimental FFL depicted in Section 2.1.1. Moreover, it is interesting to note that the accounting for the damage initiation strain in equation (2.17) leads to an 'upward curvature' tail in the lower part of the FFL.

Focusing now on in-plane shear, and thus on mode II of fracture mechanics, the integrand, $\sigma_m/\bar{\sigma}$, in the McClintock damage criterion in equation (2.9) may be expressed as the ratio between the in-plane shear stress, τ_{12}, and the effective stress, $\bar{\sigma}$:

$$D_{crit}^s = \int_0^{\bar{\varepsilon}_f} \frac{\tau_{12}}{\bar{\sigma}} d\bar{\varepsilon} = \int_0^{\varepsilon_{1f}} \frac{\tau_{12}}{\bar{\sigma}} \frac{d\bar{\varepsilon}}{d\varepsilon_1} d\varepsilon_1 \qquad (2.18)$$

Considering that $\tau_{12} = (\sigma_1 - \sigma_2)/2$ and, once again, Hill's 48 anisotropic yield criterion assuming plane stress and rotational symmetry anisotropy, equation (2.18) can be rewritten as equation (2.19).

$$D_{crit}^s = \int_0^{\varepsilon_{1f}} \frac{1}{2} \frac{1+r}{1+2r} (1 - \beta) \, d\varepsilon_1 \qquad (2.19)$$

Performing the integration in equation (2.19) and assuming $\beta = cte.$, the result is equation (2.20) and, again, if a damage initiation strain, $\bar{\varepsilon}_0$, is considered, the result is equation (2.21).

$$D_{crit}^s = \frac{1}{2} \frac{1+r}{1+2r} (\varepsilon_{1f} - \varepsilon_{2f}) \qquad (2.20)$$

$$D_{crit}^s = \frac{1}{2} \frac{1+r}{1+2r} [\varepsilon_{1f} - \varepsilon_{2f} - (1 - \beta)\varepsilon_0] \qquad (2.21)$$

Figure 2.7b shows the schematical representation of the plot of equations (2.20) and (2.21). The representation shows that the critical value of the McClintock damage criterion considering in-plane shear is a straight line with slope '+1', called the in-plane shear fracture forming limit line (SFFL). For mode II of fracture mechanics as well, the accounting for the damage initiation strain in equation (2.21) leads to an 'upward curvature' tail in the lower part of the SFFL, as it was observed in the FFL.

Similarly to in-plane shear, for the case of out-of-plane shear (mode III of fracture mechanics), the integrand, $\sigma_m/\bar{\sigma}$, in equation (2.9) may be expressed as the ratio between the out-of-plane shear stress, τ_{ti}, and the effective stress, $\bar{\sigma}$. This way, the rewriting of the normalized maximum shear damage criterion considering out-of-plane shear (or through-thickness shear) results in:

$$D_{crit}^{ts} = \int_0^{\bar{\varepsilon}_f} \frac{\tau_{ti}}{\bar{\sigma}} d\bar{\varepsilon} = \int_0^{\varepsilon_{1f}} \frac{\tau_{t1}}{\bar{\sigma}} \frac{d\bar{\varepsilon}}{d\varepsilon_1} d\varepsilon_1 \qquad (2.22)$$

Since plane stress, $\sigma_t = 0$, was assumed, the out-of-plane (or through-thickness) shear stress can be written as $\tau_{ti} = |\sigma_i - \sigma_t|/2 = |\sigma_i|/2$ (where $i = 1,2$). From Figure 2.6, it is clear that from a state of pure shear to equibiaxial tension (tension dominated stress states), τ_{t1} dominates the out-of-plane shear and from equibiaxial compression to pure shear (compression dominated stress states), τ_{t2} does it. Hence, one can write $(\tau_{t2})_{comp} \, d\varepsilon_2 = (|\sigma_2|/2) d\varepsilon_2 \equiv (\tau_{t1})_{tens} \, d\varepsilon_1 = (|\sigma_1|/2) d\varepsilon_1$. With this and all the considerations taken above for tension and in-plane shear, an expression for an adaptation of the McClintock ductile damage criterion to out-of-plane shear can be obtained:

$$D_{crit}^{ts} = \int_0^{\varepsilon_{1f}} \frac{1}{2} \frac{1+r}{1+2r} [(1+r) + r\beta] \, d\varepsilon_1 \qquad (2.23)$$

Performing the integration in equation (2.23) and assuming $\beta = cte.$, the result is equation (2.24). Yet again, a damage initiation strain, $\bar{\varepsilon}_0$, can be considered, making the integration result in equation (2.25).

$$D_{crit}^{ts} = \frac{1}{2} \frac{(1+r)^2}{1+2r} \left(\varepsilon_{1f} + \frac{r}{1+r} \varepsilon_{2f} \right) \qquad (2.24)$$

$$D_{crit}^{ts} = \frac{1}{2} \frac{(1+r)^2}{1+2r} \left[\varepsilon_{1f} + \frac{r}{1+r} \varepsilon_{2f} - \left(1 + \frac{r}{1+r} \beta \right) \varepsilon_0 \right] \qquad (2.25)$$

Figure 2.7c schematically represents the plot of equations (2.24) and (2.25). The critical value of the McClintock damage criterion considering out-of-plane shear is observed to be a straight line with slope '-1/2', called the out-of-plane shear fracture limit line (OSFFL), coinciding with the results of Kuhn et al. (1973) and confirming the speculations of fracture by shear presented by Kobayashi (1970). Considering the damage initiation strain in mode III of fracture mechanics, equation (2.25) leads to an 'upward curvature' tail in the lower part of the OSFFL, as it was observed in the FFL and in the SFFL.

For all the three modes, the effect of the damage initiation strain can be easily comprehended when considering ellipses of constant effective strain that gradually 'push' the fracture locus upward as one gets closer to biaxial expansion states, as portrayed in Figure 2.7.
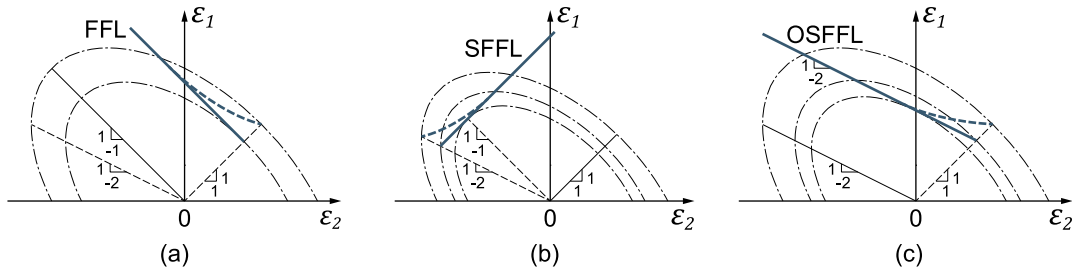
Figure 2.7 *Schematic representations of (a) the fracture forming limit line (FFL), (b) the in-plane shear fracture forming limit line (SFFL), and (c) the out-of-plane shear fracture forming limit line (OSFFL), all showing the effect of the damage initiation strain as a dashed line (adapted from Martins et al., 2014).*

When dealing with bulk forming, it is reasonable to assume isotropy. Hence, the equations for the critical value of damage in all the three modes of fracture mechanics can be rewritten with $r = 1$:

$$D_{crit} = \frac{2}{3} \left[\varepsilon_{1f} + \varepsilon_{2f} - (1+\beta)\varepsilon_0 \right] \qquad (2.26)$$

$$D_{crit}^s = \frac{1}{3} \left[\varepsilon_{1f} - \varepsilon_{2f} - (1-\beta)\varepsilon_0 \right] \qquad (2.27)$$

$$D_{crit}^{ts} = \frac{1}{3} \left[\varepsilon_{1f} + \frac{1}{2}\varepsilon_{2f} - \left(1 + \frac{\beta}{2} \right) \varepsilon_0 \right] \qquad (2.28)$$

Comparing the results above with the experimental ones obtained by Kuhn et al. (1973) and Erman et al. (1983) (schematically represented in Figure 2.4), one can readily understand that only mode I ('-1' slope) and mode III ('-1/2' slope) of fracture mechanics are present in bulk forming processes.

As perceived by Martins et al. (2014), mode I and mode II of fracture mechanics are present in sheet forming processes and, according to Leonardo et al. (2020), the only forming processes that present all three modes of fracture are the ones categorized under sheet-bulk forming.

An additional interesting result arises when comparing the fracture locus by out-of-plane shear, D_{crit}^{ts}, in equation (2.23) with the normalized version of the Cockcroft and Latham (1968) ductile damage criterion proposed by Oh et al. (1979) in equation (2.8). The weighting function in this criterion is the normalized major principal stress component, $g = \sigma_1/\bar{\sigma}$. Therefore, with a similar procedure to the one used for the McClintock ductile damage criterion, the normalized Cockcroft-Latham criterion may be rewritten as:

$$D_{crit}^{NCL} = \int_0^{\bar{\varepsilon}_f} \frac{\sigma_1}{\bar{\sigma}} d\bar{\varepsilon} = \int_0^{\varepsilon_{1f}} \frac{\sigma_1}{\bar{\sigma}} \frac{d\bar{\varepsilon}}{d\varepsilon_1} d\varepsilon_1 \qquad (2.29)$$

Using Hill's 48 anisotropic yield criterion and, again, considering rotational symmetry anisotropy and plane stress, the normalized Cockcroft-Latham ductile damage criterion results in the following expression:

$$D_{crit}^{NCL} = \frac{1+r}{1+2r}\left(\varepsilon_{1f} + \frac{r}{1+r}\varepsilon_{2f}\right) \qquad (2.30)$$

Again, a damage initiation strain, $\bar{\varepsilon}_0$, can be considered when integrating the righthand term of equation (2.29), and the result is equation (2.31). Moreover, since the focus of this work is bulk forming, assuming isotropy, $r = 1$, is reasonable, thus equation (2.31) results in equation (2.32).

$$D_{crit}^{NCL} = \frac{(1+r)^2}{1+2r}\left[\varepsilon_{1f} + \frac{r}{1+r}\varepsilon_{2f} - \left(1 + \frac{r}{1+r}\beta\right)\varepsilon_0\right] \qquad (2.31)$$

$$D_{crit}^{NCL} = \frac{2}{3}\left[\varepsilon_{1f} + \frac{1}{2}\varepsilon_{2f} - \left(1 + \frac{\beta}{2}\right)\varepsilon_0\right] \qquad (2.32)$$

Comparing equation (2.32) with equation (2.27), allows one to realize that $D_{crit}^{ts} = D_{crit}^{NCL}/2$, suggesting that the normalized Cockcroft-Latham ductile damage criterion (due to Oh et al., 1979) is not in fact a principal stress damage-based model, but rather a damage criterion based on a 'hidden' out-of-plane shear-based condition (Martins et al., 2014).

This explains why the normalized Cockcroft-Latham damage criterion presents successful results in bulk forming, particularly for test specimens that present vertical or inclined cracks, once again confirming Kobayashi's (1970) speculations that these cracks would have been caused by shear, as it was described in Section 2.1.1.

For a more detailed algebraic procedure of the equations in this section, see Appendix A.

2.2.4 The space of effective strain vs. stress triaxiality

A different representation of the fracture locus is the plot of the effective strain vs. stress triaxiality, $\bar{\varepsilon} = f(\eta)$, as it was originally proposed by Hancock and Mackenzie (1976), where the effective strain is defined considering the von Mises' yield criterion as in equation (2.33) and the stress triaxiality is defined as in equation (2.34), whose formulation is also detailed in Appendix A (A.30).

$$d\bar{\varepsilon} = \frac{\sqrt{2}}{3}[(\varepsilon_1 - \varepsilon_2)^2 + (\varepsilon_2 - \varepsilon_3)^2 + (\varepsilon_3 - \varepsilon_1)^2]^{1/2} \tag{2.33}$$

$$\eta = \frac{\sigma_m}{\bar{\sigma}} = \eta = \frac{\sqrt{1 + 2r}(1 + \beta)}{3\sqrt{1 + \frac{2r}{1+r}\beta + \beta^2}} \tag{2.34}$$

Again, since the assumption of isotropy is reasonable, equation (2.34) can be rewritten as equation (2.35).

$$\eta = \frac{\sigma_m}{\bar{\sigma}} = \frac{(1 + \beta)}{\sqrt{3}\sqrt{1 + \beta + \beta^2}} \tag{2.35}$$
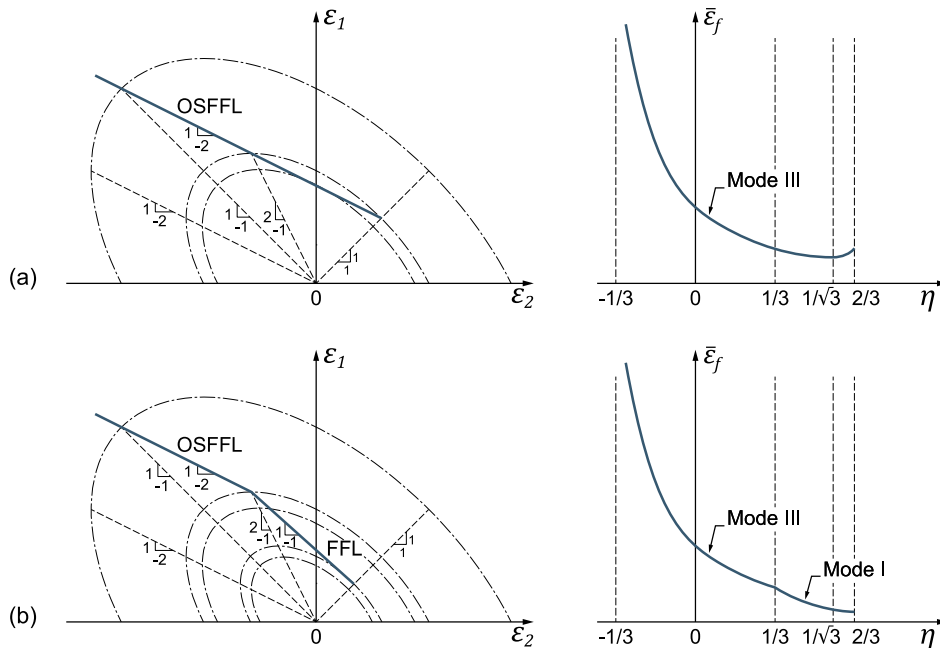
Figure 2.8 *Schematic representation of the fracture locus in the in-plane principal strain space (left) and the effective strain vs. stress triaxiality space (right) for bulk forming test specimens considering (a) a linear locus based on an OSFFL and (b) a bilinear locus resulting from the combination of an OSFFL and a FFL.*

Figure 2.8 presents an example for the schematic representation of the effective strain vs. stress triaxiality space in bulk forming test specimens, emphasizing a distinction between the curves for modes I and III of fracture mechanics. For an easier understanding of the effective strain vs. stress triaxiality plane and its linkage to the in-plane principal strain space, Table 2.2 presents the slopes of strain loading path, β, and stress triaxiality values, η, for characteristic proposloading paths considering plane stress states (reasonable for free surfaces in bulk forming).

Table 2.2 *Characteristic loading paths with respective slope of strain loading path and stress triaxiality.*

Loading path	Slope of strain loading path, $\beta = d\varepsilon_2/d\varepsilon_1$	Stress triaxiality, η
Uniaxial compression	$\beta = {}^{-2}/_1 = -2$	$\eta = -\dfrac{1}{3}$
Pure shear (torsion)	$\beta = {}^{-1}/_1 = -1$	$\eta = 0$
Uniaxial tension	$\beta = {}^{-1}/_2 = -0.5$	$\eta = \dfrac{1}{3}$
Through-thickness plane strain	$\beta = {}^{0}/_1 = 0$	$\eta = \dfrac{1}{\sqrt{3}}$
Equibiaxial tension	$\beta = {}^{1}/_1 = 1$	$\eta = \dfrac{2}{3}$

2.2.5 Tests and methodologies to obtain the FLD in bulk forming
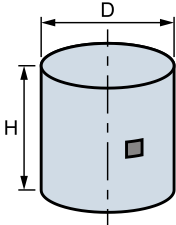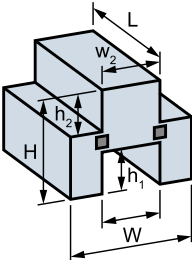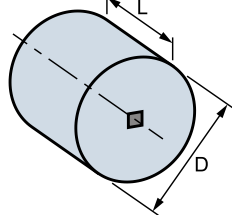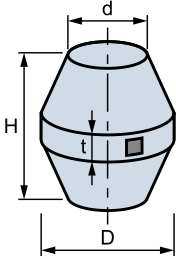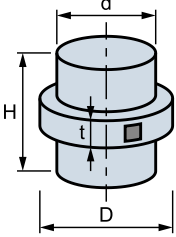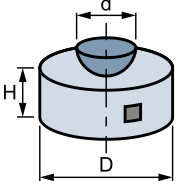
As concluded in Section 2.2.3, the fracture loci in bulk forming are related with crack opening by tension (mode I of fracture mechanics – FFL) and by out-of-plane shear (mode III of fracture mechanics – OSFFL). To assess the various loading paths that allow the fracture characterization of a given material, several bulk formability specimens must be utilized. Table 2.3 presents them with their respective initial stress and strain states for isotropic materials at critical surface locations marked with dark squares where fracture occurs.

After the circular grid system was proposed to sheet formability tests by Keeler (1968), Kuhn and Lee (1970) proposed a similar approach to bulk forming processes, printing square grid lines ($l_0 = w_0$) at the equator of cylindrical test specimens (Figure 2.9a). The major, l, and minor, w, side lengths of the rectangle resulting from the square after deformation and fracture are measured, and the strains are calculated as $\varepsilon_{\theta f} = \ln(w/w_0)$ and $\varepsilon_{zf} = \ln(l/l_0)$. This method, however, may cause inaccuracies in fracture locus identification, due to errors in measurement of the grid.

(a)   (b)
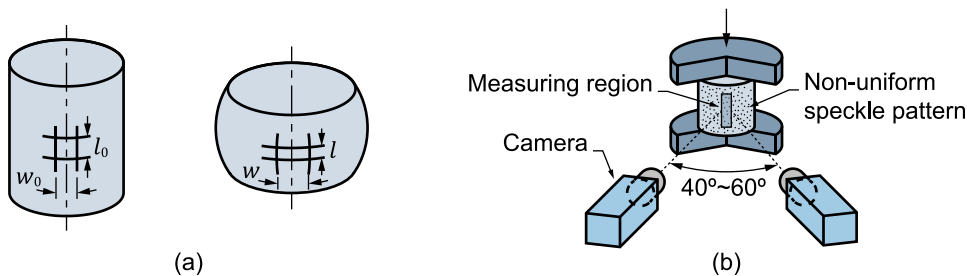
Figure 2.9 *Schematic representation of the two techniques to determine the strains at fracture in bulk formability test specimens: (a) square grid analysis (adapted from Kuhn and Lee, 1970), and (b) digital image correlation (DIC) system (adapted from Magrinho et al., 2018).*

Table 2.3 *Schematic representation of bulk formability tests (adapted from Nielsen and Martins, 2021, and Silva et al., 2015).*

Experimental test	Geometry	Initial stress state	Initial strain state
Cylindrical		$\sigma_1 = \sigma_2 = 0$ $\sigma_3 < 0$	$\varepsilon_1 = \varepsilon_2 = -\varepsilon_3/2 > 0$
Shear		$\sigma_1 = -\sigma_3 > 0$ $\sigma_2 = 0$	$\varepsilon_1 = -\varepsilon_3 > 0$ $\varepsilon_2 = 0$
Rotated cylindrical, or 'Brazilian'		$\sigma_1 = -\sigma_3 > 0$ $\sigma_2 = 0$	$\varepsilon_1 = -\varepsilon_3 > 0$ $\varepsilon_2 = 0$
Tapered		$\sigma_1 \geq 0 \geq \sigma_3$ $\sigma_2 = 0$	$\varepsilon_1 > 0$ $\varepsilon_1 \geq \varepsilon_2 \geq \varepsilon_3$ $\varepsilon_3 < 0$
Flanged		$\sigma_1 > 0$ $\sigma_2 = \sigma_3 = 0$	$\varepsilon_2 = \varepsilon_3 = -\varepsilon_1/2 < 0$
Hemispherical		$\sigma_1 > 0$ $\sigma_2 = \sigma_3 = 0$	$\varepsilon_2 = \varepsilon_3 = -\varepsilon_1/2 < 0$

As an alternative to the square grid analysis, the strains at fracture may be obtained through digital image correlation (DIC), allowing the measurement of the surface strains evolution with time (Figure 2.9b, Magrinho et al., 2018). Using the DIC system requires that the surface of the test specimens are painted with a non-uniform speckle pattern and the strains evolutions with time it provides, when combined with the load evolution with the displacement, allows for the identification of the crack-triggering time instant and for the calculation of the strain loading paths (this methodology will be further detailed in Section 4.1).

The strain loading paths that are obtained with these test specimens are depicted in Figure 2.10. An interesting observation from analyzing the work done by Silva et al. (2015) and Magrinho et al. (2018), is that the specimen geometry that defines the transition from mode III to mode I of fracture mechanics (or mixed mode) is usually the tapered one.
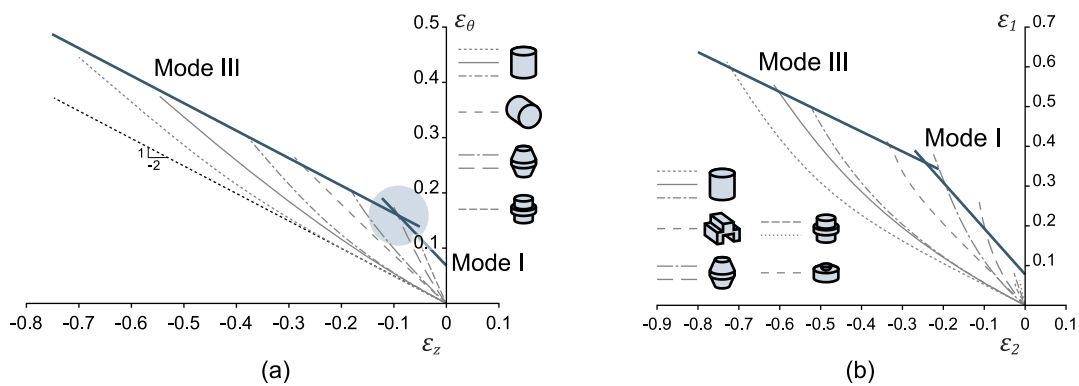
Figure 2.10 Fracture loci and strain loading paths for the different bulk formability test specimens in (a) aluminum AA 2030-T4 (adapted from Silva et al., 2015) (b) AISI 1045 steel (adapted from Magrinho et al., 2018).

2.2.6 The Lode parameters and their relation to damage

With the analysis of ductile damage in metal forming as proposed by Martins et al. (2014), and presented in Section 2.2.3, it results that the only factor that distinguishes between the different stress states is the stress triaxiality, η, that is directly related to the slope of a strain loading path, β, when considering plane stress states (see Figure 2.8 and Table 2.2).
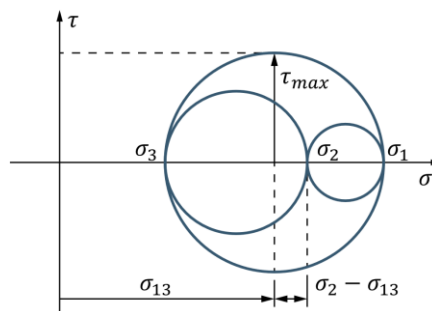
Figure 2.11 Mohr's stress circle illustrating the notation used in the definition of the Lode coefficient (adapted from Nielsen and Martins, 2021).

A need for distinction between different stress states with yet similar loading paths, led researchers to develop an additional stress ratio, known as the Lode coefficient or Lode's stress parameter, μ, (due to Lode, 1926). This parameter is a measure of the intermediate principal stress component, σ_2, that allows to analyze its influence on yielding, according to Tresca's and von Mises' yield criteria (Figure 2.11):

$$\sigma_2 = \frac{\sigma_1 + \sigma_3}{2} + \mu \frac{\sigma_1 - \sigma_3}{2} \tag{2.36}$$

$$\mu = \frac{2\sigma_2 - \sigma_1 - \sigma_3}{\sigma_1 - \sigma_3} = \frac{\sigma_2 - \frac{1}{2}(\sigma_1 + \sigma_3)}{\frac{1}{2}(\sigma_1 - \sigma_3)} = \frac{\sigma_2 - \sigma_{13}}{\tau_{max}} \tag{2.37}$$

where $-1 \leq \mu \leq 1$, since for $\sigma_2 = \sigma_3$ the result is $\mu = -1$ and for $\sigma_1 = \sigma_2$ the result is $\mu = 1$.

For the case of the von Mises' yield criterion, by combining the definitions of stress triaxiality, η, and the Lode coefficient, μ, one can express the principal stresses as follows:

$$\begin{aligned}
\sigma_1 &= \sigma_m + \frac{(3-\mu)\bar{\sigma}}{3\sqrt{3+\mu^2}} = \left(\eta + \frac{3-\mu}{3\sqrt{3+\mu^2}}\right)\bar{\sigma} \\
\sigma_2 &= \sigma_m + \frac{2\mu\bar{\sigma}}{3\sqrt{3+\mu^2}} = \left(\eta + \frac{2\mu}{3\sqrt{3+\mu^2}}\right)\bar{\sigma} \\
\sigma_3 &= \sigma_m - \frac{(3+\mu)\bar{\sigma}}{3\sqrt{3+\mu^2}} = \left(\eta - \frac{3+\mu}{3\sqrt{3+\mu^2}}\right)\bar{\sigma}
\end{aligned} \tag{2.38}$$

Another way of expressing the Lode coefficient is by means of the Lode angle, θ, and the Lode angle parameter, ξ. Equation (2.38) makes clear the connection between the Lode coefficient, μ, and the deviatoric part of the stress tensor, which controls the distortional effects in material deformation, and allows for the use of the π-plane (Figure 2.12b), or octahedral plane, in order to disregard the hydrostatic stress, σ_m, and provide an easier look on the Lode angle than in the Haigh-Westergaard stress space (after Westergaard, 1920 – Figure 2.12a).
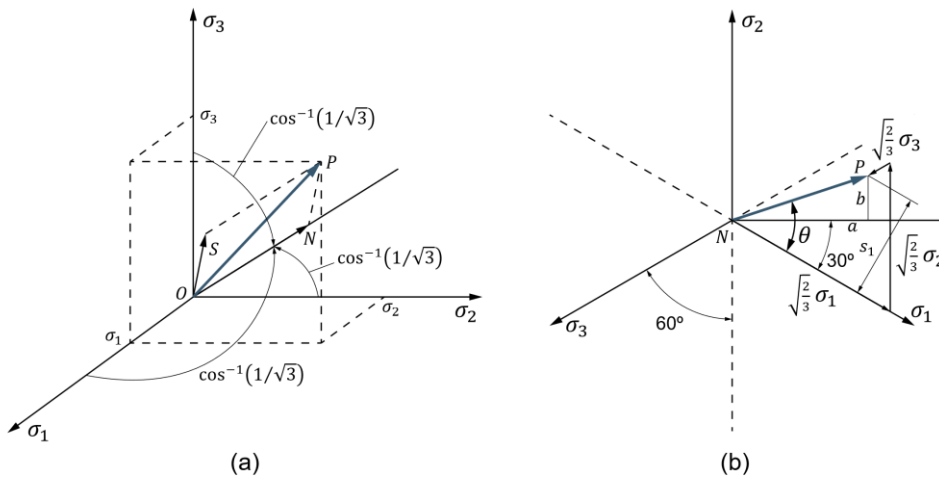
Figure 2.12 *Representation of a stress state characterized by point P (a) in the Haigh-Westergaard stress space (adapted from Nielsen and Martins, 2021), and (b) its projection on the π-plane (adapted from Mendelson, 1986).*

22

An analysis of Figure 2.12b allows for the obtainment of the following expression, that relates the Lode angle, θ, and the Lode coefficient, μ:

$$\tan\theta = \frac{\sqrt{3}(\mu + 1)}{3 - \mu} \tag{2.39}$$

In turn, the Lode angle parameter, or normalized third deviatoric stress invariant (Bai and Wierzbicki, 2008), ξ, is defined as presented by Chen (1982):

$$\xi = \cos 3\theta = \frac{3\sqrt{3}}{2}\frac{J_3}{J_2^{3/2}} = \frac{27}{2}\frac{J_3}{\bar{\sigma}} \tag{2.40}$$

where J_2 and J_3 are, respectively, the second and third deviatoric stress tensor invariants.

For the case of plane stress, $\sigma_3 = 0$, and considering the von Mises' yield criterion, the Lode angle parameter, ξ, in equation (2.40) may be expressed in terms of stress triaxiality, η, as follows:

$$\xi = \cos 3\theta = -\frac{27}{2}\eta\left(\eta^2 - \frac{1}{3}\right) \tag{2.41}$$

Furthermore, the Lode angle can be normalized (Bai and Wierzbicki, 2008) for representation purposes and to fall in the same limits of ξ, being defined as:

$$\bar{\theta} = 1 - \frac{6\theta}{\pi} = 1 - \frac{2}{\pi}\cos^{-1}\xi = 1 - \frac{2}{\pi}\cos^{-1}\left[-\frac{27}{2}\eta\left(\eta^2 - \frac{1}{3}\right)\right] \tag{2.42}$$

The graphical representation of the evolution of stress triaxiality, η, with the normalized Lode angle, $\bar{\theta}$, and with the Lode angle parameter, ξ, (i.e., the plot of equations (2.42) and (2.41)) is presented, respectively, by the curves in blue and orange in Figure 2.13.
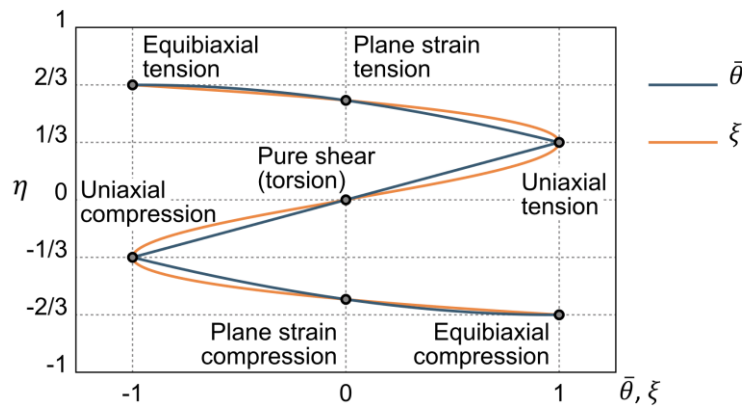
Figure 2.13 *Variation of stress triaxiality, η, with the normalized Lode angle, $\bar{\theta}$, (blue curve) and the Lode angle parameter, ξ, (orange curve) (adapted from Bai and Wierzbicki, 2008).*

Bai and Wierzbicki (2010) expressed the three principal stress components in terms of the Lode angle, θ, and the stress triaxiality, η:

$$\sigma_1 = \bar{\sigma}\left(\eta + \frac{2}{3}\cos\theta\right) \tag{2.43}$$

$$\sigma_2 = \bar{\sigma}\left[\eta + \frac{2}{3}\cos\left(\frac{2}{3}\pi - \theta\right)\right] \tag{2.44}$$

$$\sigma_3 = \bar{\sigma}\left[\eta + \frac{2}{3}\cos\left(\frac{2}{3}\pi + \theta\right)\right] \tag{2.45}$$

With these expressions, and using Tresca's yield criterion, $\tau_{max} = (\sigma_1 - \sigma_3)/2$, Lou et al. (2012) wrote the normalized maximum shear stress, $2\tau_{max}/\bar{\sigma}$, only in terms of the Lode angle, θ:

$$\frac{2\tau_{max}}{\bar{\sigma}} = \frac{\sigma_1 - \sigma_3}{\bar{\sigma}} = \frac{2}{3}\left[\cos\theta - \cos\left(\frac{2}{3}\pi + \theta\right)\right] \tag{2.46}$$

By now combining equations (2.41) and (2.46), the normalized maximum shear stress, $2\tau_{max}/\bar{\sigma}$, can be rewritten in terms of the stress triaxiality, η, as follows:

$$\frac{2\tau_{max}}{\bar{\sigma}} = \frac{2}{3}\left\{\cos\left[\frac{1}{3}\cos^{-1}\left(-\frac{27}{2}\eta\left(\eta^2 - \frac{1}{3}\right)\right)\right] \\ - \cos\left[\frac{2}{3}\pi + \frac{1}{3}\cos^{-1}\left(-\frac{27}{2}\eta\left(\eta^2 - \frac{1}{3}\right)\right)\right]\right\} \tag{2.47}$$

The graphical representation of the variation of the normalized maximum shear stress, $2\tau_{max}/\bar{\sigma}$, with stress triaxiality, η, (i.e., the plot of equation (2.47)) is presented in Figure 2.14.
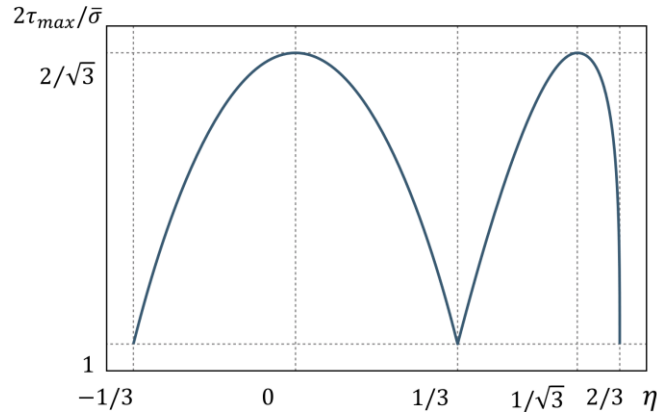
Figure 2.14 *Graphical representation of the variation of the normalized maximum shear stress, $2\tau_{max}/\bar{\sigma}$, with stress triaxiality, η.*

Validating the motto for the establishing of the Lode parameter, μ, Bai and Wierzbicki (2008) presented an illustrative three-dimensional graphical representation of the relation between stress triaxiality, η, the effective strain at fracture, $\bar{\varepsilon}_f$, and the normalized Lode angle, $\bar{\theta}$, (Figure 2.15) that is directly related to the Lode parameter, as shown in this section. Figure 2.15a presents this representation for the fracture criterion proposed by Johnson and Cook (1985) that does not account for the Lode parameters, while Figure 2.15b presents the representation for the uncoupled ductile damage criterion proposed by Bai and Wierzbicki (2008) that does account for them.

In these representations, the damage criteria are represented by the red curves on the surfaces rather than the surfaces themselves, being the latter used just for providing an easier special

perception. The projection of either curve on a single $\bar{\varepsilon}_f = f(\eta)$ plane allows for the representation of bidimensional fracture loci on the space of effective strain at fracture vs. stress triaxiality.
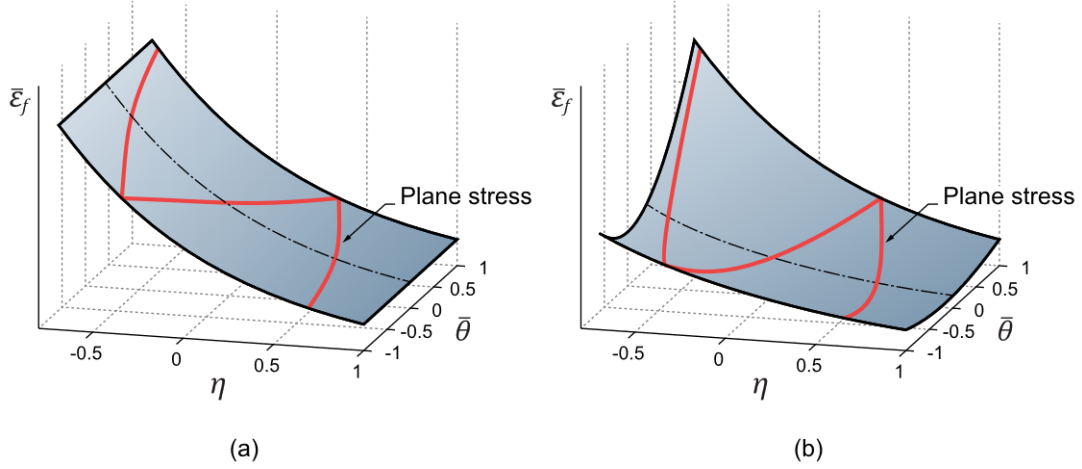
Figure 2.15 *Schematic representation of the fracture loci (a) not accounting for the Lode parameters (fracture criterion proposed by Johnson and Cook, 1985), and (b) accounting for the Lode parameters (uncoupled ductile damage criterion proposed by Bai and Wierzbicki, 2008) in a three-dimensional version of the space of effective strain at fracture vs. stress triaxiality, that includes the normalized Lode angle (adapted from Bai and Wierzbicki, 2008).*

It is interesting to note from Figure 2.14 that the normalized maximum shear stress, $2\tau_{max}/\bar{\sigma}$, has its maxima for pure shear ($\eta = 0$) and for through-thickness plane strain ($\eta = 1/\sqrt{3}$), as one would expect, and minima for situations of uniaxial compression ($\eta = -1/3$), uniaxial tension ($\eta = 1/3$), and equibiaxial tension ($\eta = 2/3$), where shear has a smaller effect. Furthermore, the maximum value of $2\tau_{max}/\bar{\sigma}$ is $2/\sqrt{3} \approx 1.155$, i.e., the ratio between the values of effective stress for the von Mises' and the Tresca's yield criteria, which makes sense, since Figure 2.14 corresponds to the plot of equation (2.47), which is a combination of equation (2.41), that was built on the former criterion, and equation (2.46), that was built on the latter.

Yet, it is worth noting that while Figure 2.13 and Figure 2.15 present values for stress triaxiality, η, between $-2/3$ and $2/3$, current bulk formability tests only allow for states of $-1/3 \le \eta \le 1/\sqrt{3}$ (from uniaxial compression to through-thickness plane strain) and, in theory, uniaxial compression stress states (with $\eta = -1/3$) lead to infinitely large damage values with no fracture in bulk forming and when considering plane stress conditions (due to the $-1/2$ slope of the OSFFL in the in-plane principal strain space, or the $\eta = -1/3$ asymptote in the space of effective strain vs. stress triaxiality – see Figure 2.8). Nevertheless, this representation is acceptable in theoretical terms as it complies with the solid mechanics' definition of principal strains ($\varepsilon_1 \ge \varepsilon_2$).

For more details on the algebraic procedure for the obtainment of equations (2.37) to (2.47), refer to Appendix B.

2.2.7 Işık's (2018) uncoupled fracture risk criterion

Some important conclusions can be withdrawn from the previous sections of this work, namely:

a. The hydrostatic component of the stress tensor controls dilatational effects on void growth by means of stress triaxiality (Section 2.1 – equation (2.1)).

b. The deviatoric component of the stress tensor controls changes in void shape by distortion through the Lode parameters (Section 2.1 – equation (2.2)).

c. The fracture locus has a trend shift near the state of uniaxial tension, $\eta = 1/3$ (Figure 2.8b).

d. There is no possibility of having void growth in materials subjected to compressive states of stress under $\eta < -1/3$ (as explained in the previous section).

These conclusions, led Işık (2018) to propose an uncoupled ductile damage criterion, or fracture risk criterion, with a nondimensional weighting function, g, that combines the effect of stress triaxiality, η, in void growth with the effect of shear in void shape changing, that is implicitly related to the Lode parameters (μ, θ, or ξ), as shown in Section 2.2.6 in equation (2.46):

$$D_{crit}^{I\varsigma} = \int_0^{\bar{\varepsilon}_f} \left[A\langle 1 + 3\eta \rangle + B \left(\frac{2\tau_{max}}{\bar{\sigma}} - 1 \right) \right] d\bar{\varepsilon} \equiv D(\eta) + D(\mu) \tag{2.48}$$

where A and B are material parameters to be identified. Respectively, they account for the impact of dilatational and distortional effects in void growth and coalescence.

Considering the criteria proposed by Christiansen et al. (2016) and Lou et al. (2012) in equations (2.10) and (2.11), one can see that they also account for the Lode parameters:

$$D_{crit}^{Ch} = \int_0^{\gamma_f} \frac{\tau}{\bar{\sigma}} d\gamma + \int_0^{\gamma_f} \frac{3}{2} \frac{\sigma_m}{\bar{\sigma}} d\gamma \equiv D(\mu) + D(\eta) \tag{2.49}$$

$$D_{crit}^{Lo} = \int_0^{\bar{\varepsilon}_f} \left(\frac{\tau}{\bar{\sigma}} \right)^A \left(\frac{\langle 1 + 3\sigma_m/\bar{\sigma} \rangle}{2} \right)^B d\bar{\varepsilon} \equiv D(\mu) \times D(\eta) \tag{2.50}$$

However, these last two models result in a narrow range of applicability. For instance, the criterion due to Christiansen et al. (2016) is limited to pure shear or combined shear and tension situations, struggling with states where voids grow solely by tension. The criterion due to Lou et al. (2012) is based on an approach similar to that of Bao and Wierzbicki (2004), where results from bulk and sheet formability tests are treated together, arising all the problems due to differences between plastic flow, already mentioned in Section 2.1.1.

From Figure 2.14, it is clear that the weighting function in equation (2.48) does not allow for an accumulation of damage due to the Lode parameters in situations of uniaxial compression ($\eta = -1/3$), nor uniaxial tension ($\eta = 1/3$), nor equibiaxial tension ($\eta = 2/3$), since in these cases $2\tau_{max}/\bar{\sigma} = 1$ and, therefore, the second term of the weighting function in equation (2.48) equals zero, meaning that no shear is reckoned.

By assuming proportional strain loading paths and normalizing the material parameters, A and B, with the critical damage, $D_{crit}^{I\c{s}}$, equation (2.48) can be rewritten as follows, in order to plot the fracture locus in the space of effective strain vs. stress triaxiality (Figure 2.16):

$$\bar{\varepsilon}_f = \frac{1}{A\langle 1 + 3\eta \rangle + B\left(\frac{2\tau_{max}}{\bar{\sigma}} - 1\right)} \tag{2.51}$$
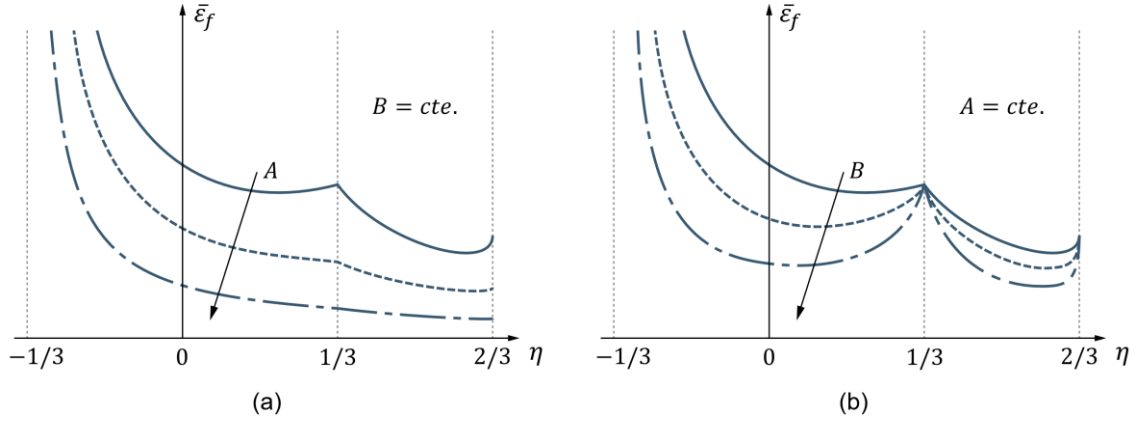
Figure 2.16 *Schematic representation of the fracture loci obtained with the fracture risk criterion due to Işık (2018) in the space of effective strain vs. stress triaxiality evidencing the influence of the material parameters (a) A and (b) B (adapted from Işık, 2018).*

Having been developed for the characterization of damage in sheet-bulk forming, this criterion does not make any distinction between sheet and bulk metal forming, being this diferentiation controlled by the ratio between the material parameters A and B (Figure 2.16). Nevertheless, like the analytical framework provided by Martins et al. (2014) and the analysis conducted in Section 2.2.3 and Appendix A, this criterion leads to an assymptote for the case of uniaxial compression ($\eta = -1/3$), being in agreement with the statement of infinetily large damage values for $\eta = -1/3$ in plane stress conditions presented in the end of Section 2.2.6.

Furthermore, as it is observable in Figure 2.16, as the B/A ratio increases, the shape of the fracture locus tends to evolve from a monotonic curve to a 'double valley', with a local maximum at $\eta = 1/3$ (uniaxial tension) and two local minima for $\eta = 0$ (pure shear) and for $\eta = 1/\sqrt{3}$ (through-thickness plane strain).

2.3 Shortcomings in bulk formability

An interesting point that arises from all the previous sections is that when it comes to bulk forming no specimen is able to reach the first quadrant of the in-plane principal strain space, i.e., a state of biaxial tension, opposing to what happens in sheet formability tests (see Figure 2.4a). In an attempt to change this, Silva et al. (2015) developed a ring expansion test specimen with a stepped conical punch that was able to create these strain states (Figure 2.17). Yet, this was only achievable at the inner surface of the specimen, thus it could not be analyzed with DIC. Moreover,

it was on a surface in contact with the die, creating difficulties in reading square grid lines after deformation, due to friction. Also, the contact with the die does not create plane stress conditions at the outer surface, hence the values of stress triaxiality are not characteristic of a truly expansion state (Figure 2.17b), although it is what appears to be shown in the in-plane principal strain space (Figure 2.17a), arising the conclusion that the latter is inadequate to characterize three-dimensional stress loading states, i.e., not in plane stress conditions.

Nevertheless, 'true' biaxial tension states at fracture were found on partial extrusion experiments (Figure 2.17c) of AISI 4640 sintered steel powder by Erman et al. (1983), that also recognized the need for a full characterization of the fracture limits in bulk forming. However, extremely small values of strain were achieved, and this test cannot be analyzed by DIC since fracture initiates on a die-covered surface. Additionally, the elastic rebound of the material makes the repeated evaluation of strain evolution through grid marks very difficult.
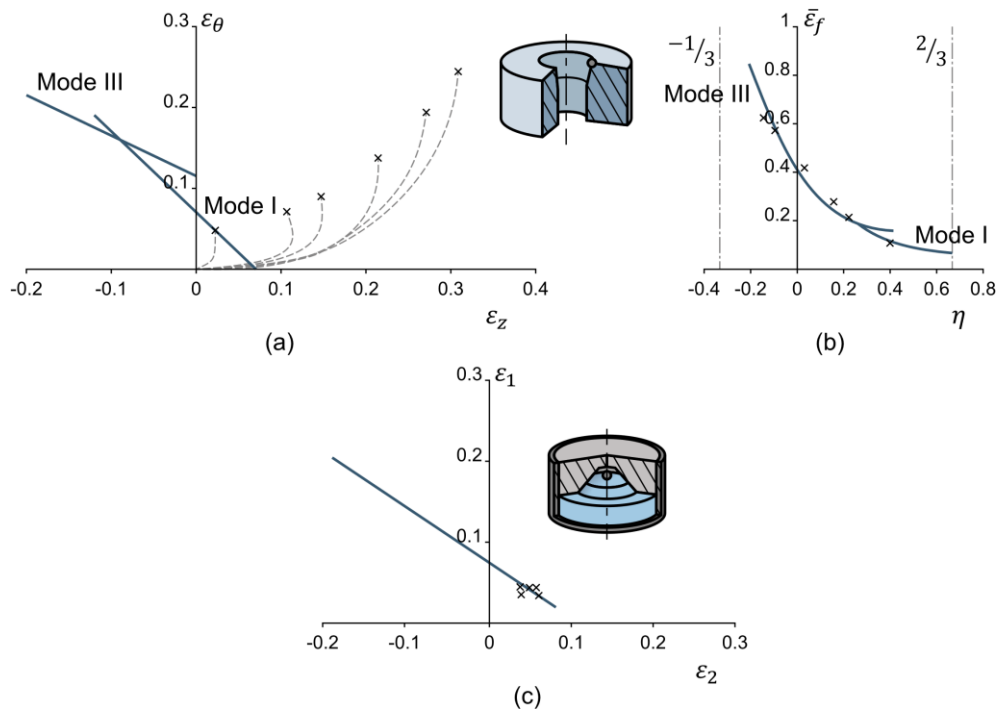
Figure 2.17 (a) Loading paths and fracture loci for the ring expansion test specimens represented in the in-plane principal strain space, (b) fracture loci for the same specimen in the effective strain at fracture vs. stress triaxiality space (adapted from Silva et al., 2015), and (c) fracture loci for partial extrusion operations in the in-plane strain space (adapted from Erman et al., 1983).

Besides, even though recent studies point mostly to the existence of bilinear fracture loci in bulk forming with mode I between the states of uniaxial tension ($\eta = 1/3$) and through-thickness plane strain ($\eta = 1/\sqrt{3}$) (e.g., Silva et al., 2015, or Magrinho et al., 2018 – see Figure 2.10), the fact that older studies (e.g., Kuhn et al., 1973, or Gouveia et al., 1996) present bulk formability limits fully defined by a single '-1/2' sloped line corresponding to the crack opening mode III suggests that there may be an 'uncertainty region' (Figure 2.18) in which either mode I or III may be responsible for the crack opening mechanism that may depend on the material being tested or on temperature, as perceived by Erman et al. (1983), revealing a competition between modes of fracture.
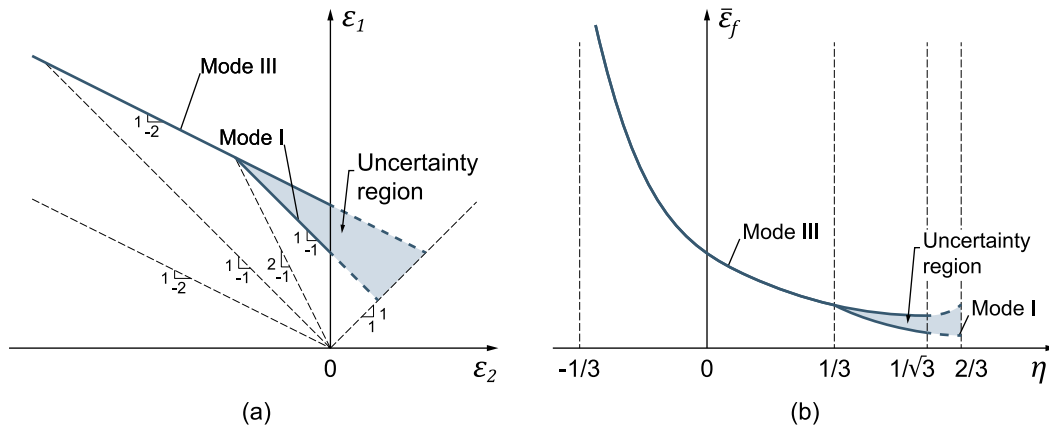
Figure 2.18 *Schematic representation of the formability limits in (a) the in-plane principal strain space and (b) the space of effective strain at fracture vs. stress triaxiality, evidencing the uncertainty region shaded in light blue.*

Erman et al. (1983) tackled this competition, stating that the 'deviations in the small strain region' could be justified with the Marciniak and Kuczyński (1967) model for localized thinning when small inhomogeneities were considered in the axial and radial directions. Claiming that the application of this model with inhomogeneities in the radial direction could reproduce the fracture forming line with a slope of '-1/2', they suggested that the inhomogeneities in the axial direction could justify the already mentioned deviations. However, as explained when addressing the combined treatment of sheet and bulk forming in Section 2.1.1, differences in plastic flow and the lack of a necking-preceded fracture in bulk forming makes unsuitable the application of a localized instability model based on the plane stress conditions of sheet metal forming to the three-dimensional stress state conditions of bulk metal forming.

Therefore, the two main objectives of this thesis are the development of a test specimen geometry that allows for the characterization of bulk formability limits in states of biaxial tension on a free outer surface in upsetting conditions and the development of a single ductile damage criterion that is able to fairly modulate the material preference for either of the fracture modes.

Chapter 3

Theoretical development

This chapter focuses mainly on tackling the problems and shortcomings in bulk metal forming enunciated in Section 2.3. To overcome these: 1) a novel geometry for a bulk test specimen to characterize states of biaxial tension in bulk forming is developed (Section 3.1); 2) starting with the development of an analytical expression for the shift from the in-plane principal strain space to the space of effective strain vs. stress triaxiality in mode III (Section 3.2), 3) a new single uncoupled ductile damage criterion to model fracture in bulk forming is proposed (Section 3.3); and 4) an Excel workbook to study the suitability of four different criteria is presented and explained in detail (Section 3.4): the McClintock criterion (due to Ayada et al., 1987), the normalized Cockcroft-Latham criterion (due to Oh et al., 1979), Işık's (2018) criterion, and the newly proposed one.

3.1 Development of a novel bulk test specimen for biaxial tensile stress states

It was introduced in Section 2.3 the need to characterize biaxial tension states not only in the in-plane principal strain space (as did Silva et al., 2015), but also in the space of effective strain vs. stress triaxiality, i.e., in plane stress conditions, which in bulk forming is only possible in free surfaces. When considering upsetting conditions, this leads to a specimen that presents positive values for strain at fracture in both the azimuthal, $(\varepsilon_\theta)_f > 0$, and the longitudinal, $(\varepsilon_z)_f > 0$, directions while still creating the radial stress, σ_r, variations characteristic of bulk forming processes.

To better evaluate strain evolutions at the fracture site, the latter needs to be on the specimen's outer surface and, preferably, in the longitudinal mid-plane (or the specimen's equator). Hence, these needed conditions premise the creation of a 'barreled ring' specimen (Figure 3.1a) that expands in the azimuthal direction, θ, due to upsetting and, although most of the material is in a compressive state, the momentum created in the longitudinal mid-plane due to the compressive forces acting on the upper and bottom surfaces (refer to the black arrows in Figure 3.1b) allows for tensile stress states in the longitudinal direction, z, on the outer surface.
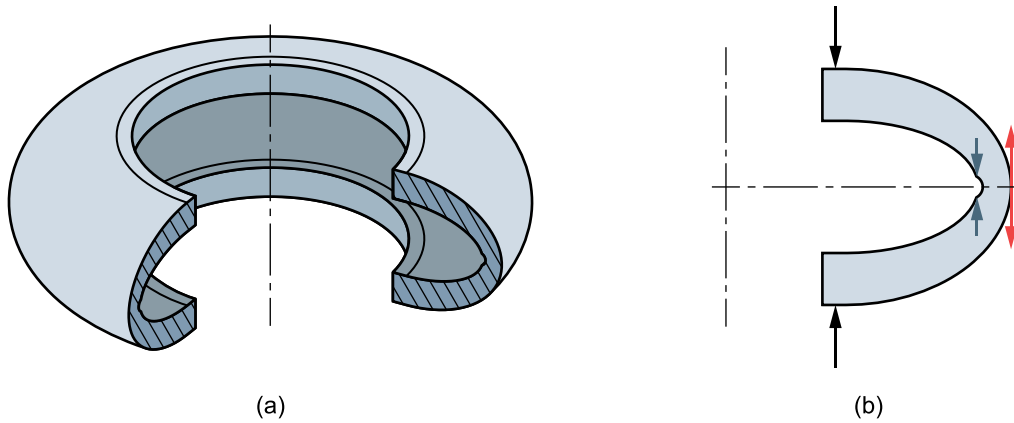
Figure 3.1 *(a) 3D model of the barreled ring test specimen with a section cut for easier geometry understanding and (b) schematic representation of the deformation mechanism to create biaxial tensile stress states in the barreled ring test specimen.*

As the conditions above were never achieved before, numerical simulations were fulfilled to guarantee that the new test specimen would attain them. These simulations were performed with the finite element computer program *i-form*, an in-house software created and developed by the Manufacturing and Industrial Management Unit of *Instituto Superior Técnico* and the Technical University of Denmark. Considering both the finite element method and plasticity theory, it is built upon the irreducible finite element flow formulation and accounts for the practical non-linearities in geometry, material properties, and contact changes, which are typical of the interaction between workpieces and tools, being able to produce accurate predictions of, among others, strains, stresses, and damage (Nielsen et al., 2013). This way, a geometry analysis that meets the desired results is done in a less expensive and time-consuming way than it would with a fully experimental analysis.

The numerical simulations were conducted with two-dimensional finite element models with linear quadrilateral elements, taking advantage of the axisymmetric properties of the specimen. The most refined models contained around 5600 elements and 5800 nodal points, with the simulations taking approximately 1 hour to run on a standard laptop equipped with an Intel i5-7200U CPU (2.5 GHz) processor. The mesh was slightly refined by means of a quadtree subdivision strategy at the central zone of the specimen and an additional refinement was applied at the surrounding area of the outer surface at the equator of the specimen (Figure 3.2), where fracture is expected to develop and where damage is expected to be maximum. The specimen was assumed deformable and isotropic objects.

The compression platens were modelled as rigid objects and discretized with linear contact-friction elements. Friction was modelled through the law of constant friction $\tau_f = mk$, where k is the shear flow stress and m is the friction factor, that was set equal to 0.1 after verifying the finite element predicted forces that best matched the experimental measurements.
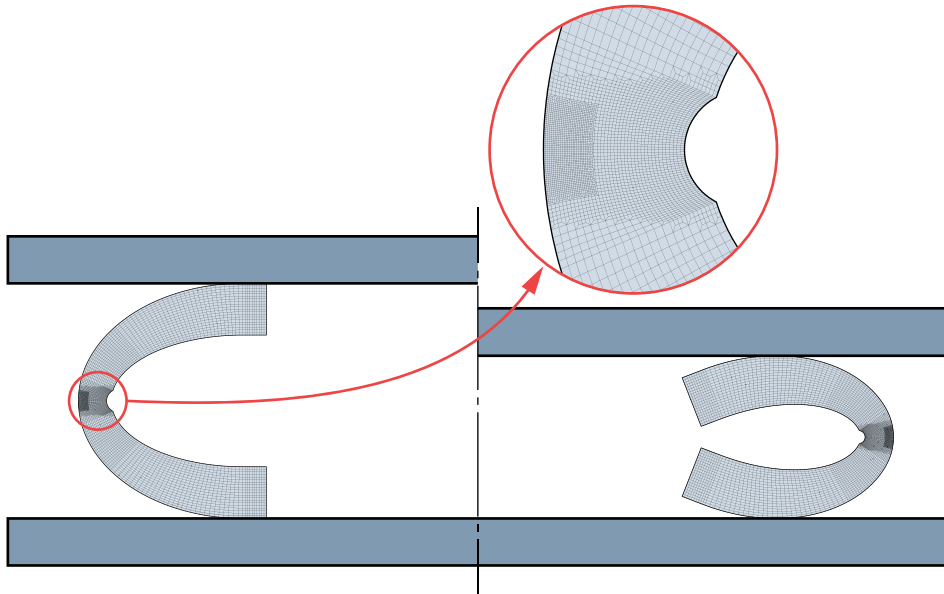
Figure 3.2 *Representation of the most refined used mesh in the (left) undeformed/initial stage and (right) deformed stage.*

Depicted in Figure 3.3a and Figure 3.3b are the finite element predicted distributions for the longitudinal, σ_z, and radial, σ_r, stresses, respectively, with details of the expected fracture initiation site.

As can be perceived, the predicted σ_z distribution in Figure 3.3a allows to conclude that the barreled ring specimen meets the desired conditions that were enunciated in the beginning of this section to create states of longitudinal tension, $\sigma_z > 0$, on the equatorial free surface. Combined with the circumferential tensile stresses, $\sigma_\theta > 0$, that arise due to ring expansion during the upsetting. This result proves that the barreled ring specimen is subjected to biaxial tension on the outer equatorial free surface where the cracks are expected to trigger.

Additionally, the predicted σ_r distribution in Figure 3.3b verifies the unavoidable existence of plane stress conditions, $\sigma_r = 0$, on the outer and inner equatorial free surfaces, and the presence of radial stress variations, $\sigma_r \neq 0$, throughout the specimen's thickness. These variations indicate that the barreled ring test specimen can replicate the three-dimensional stress states typical of bulk metal forming, as it was intended.

Since, according with the definition of uncertainty region proposed in Section 2.3, fracture in this region may be triggered by either tension (mode I) or through-thickness shear (mode III), Figure 3.3c and Figure 3.3d show the finite element predicted distribution of damage according to the McClintock (mode I) and normalized Cockcroft-Latham (mode III) criteria, respectively. As seen, high values of damage are concentrated on the equatorial free surface when considering either of the criteria. Since the McClintock and normalized Cockcroft-Latham criteria represent modes I and III of fracture mechanics (as seen in Section 2.2.3), respectively, these results indicate that, when upsetting the barreled ring specimen, cracks are in fact triggered on the equatorial free surface, whatever crack opening mode manifests.
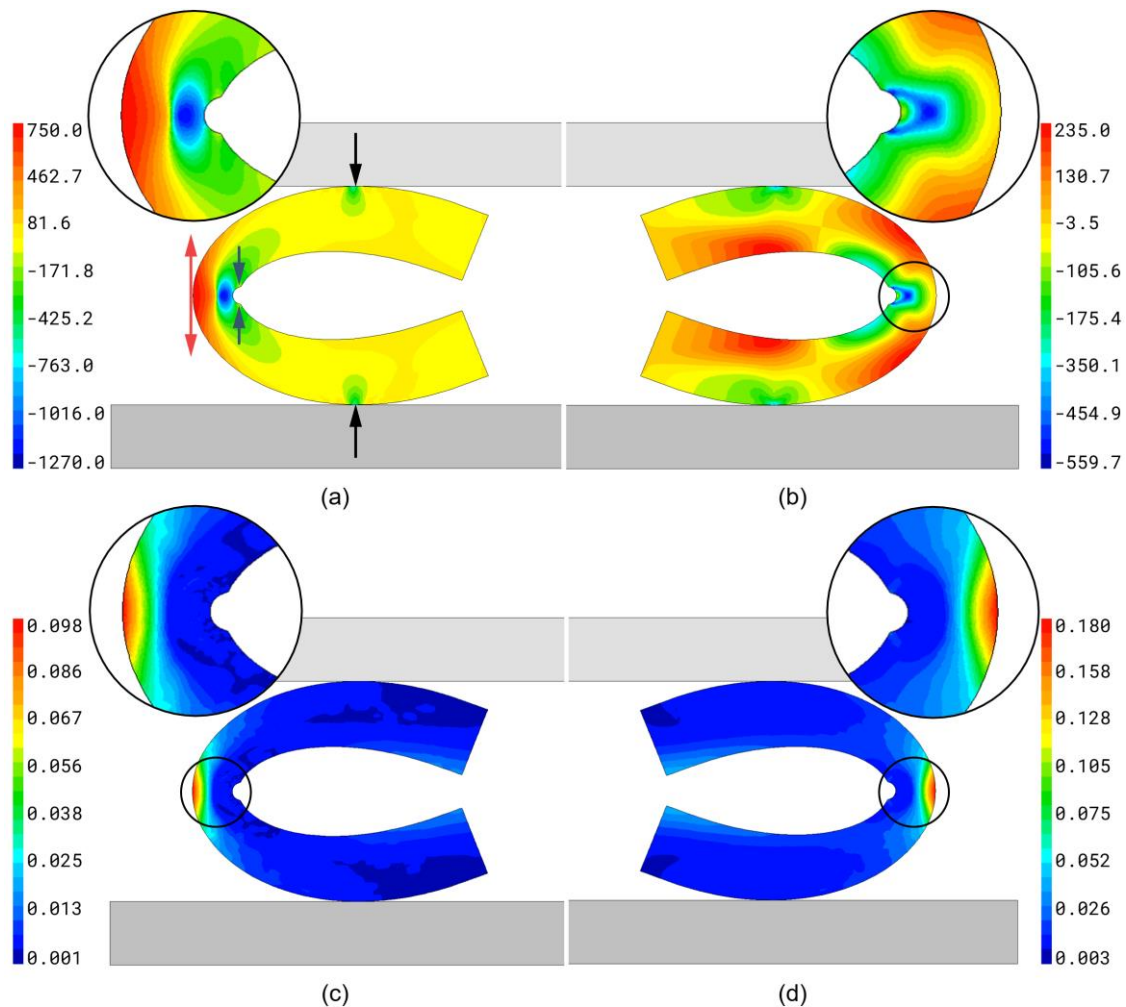
Figure 3.3 *Finite element predicted distributions of (a) longitudinal stress, σ_z, (b) radial stress, σ_r, (c) ductile damage according to the McClintock criterion and (d) ductile damage according to the normalized Cockcroft-Latham criterion.*
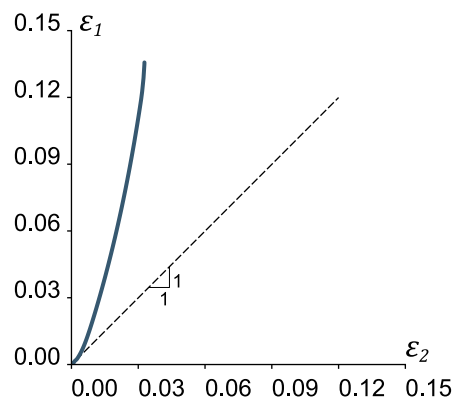
Figure 3.4 *Finite element method-predicted strain loading path for a point on the outer equatorial free surface of the barreled ring specimen in the in-plane principal strain space.*

Additionally, Figure 3.4 presents the graphical representation of the FEM prediction for the strain loading path for a point on the outer equatorial free surface of the barreled ring specimen in the in-plane principal strain space, that, once again, confirms biaxial tension states. For the case of this specimen, $\varepsilon_1 = \varepsilon_z$ and $\varepsilon_2 = \varepsilon_\theta$, opposing to what happens for the conventional bulk

33

specimens, where compression in the longitudinal direction coexists with longitudinal tension at the fracture initiation site, hence resulting in $\varepsilon_1 = \varepsilon_\theta$ and $\varepsilon_2 = \varepsilon_z$.

3.2 The normalized Cockcroft-Latham damage criterion as a function of stress triaxiality

From the previous section, fracture in the barreled ring may initiate by out-of-plane shear (mode III) or tension (mode I), thus both the normalized Cockcroft-Latham and McClintock criteria must be studied. Conducting a similar analysis to that on the end of Section 2.2.7, but for the referred ductile damage criteria (equations (2.8) and (2.9), respectively), and by assuming proportional strain loading paths, the following expressions for the effective strains at fracture for these criteria result:

$$\bar{\varepsilon}_f = \frac{D_{crit}^{NCL}}{\sigma_1/\bar{\sigma}} \tag{3.1}$$

$$\bar{\varepsilon}_f = \frac{D_{crit}^{Mc}}{\eta} \tag{3.2}$$

The effective strain at fracture for the McClintock criterion (3.2) is inevitably written in terms of stress triaxiality, η, since the latter is the integrand for the criterion – a similar expression (3.3) was also derived by Silva et al. (2015), in which $Y = (3 \times D_{crit}^{Mc})/2$. However, this is not the case for the normalized Cockcroft-Latham one (3.1) and, to change this, the normalized major principal stress component, $\sigma_1/\bar{\sigma}$, must be written in terms of η.

$$\bar{\varepsilon}_f = \frac{2}{3}\frac{Y}{\eta} \equiv \frac{D_{crit}^{Mc}}{\eta} \tag{3.3}$$

Using the ratios already calculated for the analysis in Section 2.2.3 (and obtained in Appendix A), one can write the $\sigma_1/\bar{\sigma}$ ratio as follows:

$$\frac{\sigma_1}{\bar{\sigma}} = \frac{\eta}{\sigma_m/\sigma_1} = \frac{3[(1+r)+r\beta]}{(1+2r)(1+\beta)}\eta \tag{3.4}$$

To fully rewrite equation (3.4) only in terms of stress triaxialy, η, there is a need to find the inverse of the expression in equation (2.35), that related η with the slope of a proportional strain loading path, β, eventually resulting in equation (3.5):

$$\beta = \frac{-2\left(\frac{9\eta^2 r}{(1+r)} - (1+2r)\right) - 6\eta\sqrt{-\left(\frac{9\eta^2}{(1+r)^2} - \frac{2}{(1+r)}\right)(1+2r)}}{2(9\eta^2 - (1+2r))} \tag{3.5}$$

This last expresssion may now be inserted into equation (3.4):

$$\frac{\sigma_1}{\bar\sigma} = \left(\frac{3}{1+2r}\right)\frac{(1+r)+r\dfrac{-2\left(\dfrac{9\eta^2 r}{(1+r)}-(1+2r)\right)-6\eta\sqrt{-\left(\dfrac{9\eta^2}{(1+r)^2}-\dfrac{2}{(1+r)}\right)(1+2r)}}{2\left(9\eta^2-(1+2r)\right)}}{1+\dfrac{-2\left(\dfrac{9\eta^2 r}{(1+r)}-(1+2r)\right)-6\eta\sqrt{-\left(\dfrac{9\eta^2}{(1+r)^2}-\dfrac{2}{(1+r)}\right)(1+2r)}}{2\left(9\eta^2-(1+2r)\right)}}\,\eta \qquad (3.6)$$

Finally, the $\sigma_1/\bar\sigma$ ratio in equation (3.1) may be replaced by the expression in equation (3.6), allowing for the plot of the normalized version of the Cockcroft-Latham damage criterion:

$$\bar\varepsilon_f = \frac{(1+2r)\left(1+\dfrac{-2\left(\dfrac{9\eta^2 r}{(1+r)}-(1+2r)\right)-6\eta\sqrt{-\left(\dfrac{9\eta^2}{(1+r)^2}-\dfrac{2}{(1+r)}\right)(1+2r)}}{2\left(9\eta^2-(1+2r)\right)}\right)}{3\left((1+r)+r\dfrac{-2\left(\dfrac{9\eta^2 r}{(1+r)}-(1+2r)\right)-6\eta\sqrt{-\left(\dfrac{9\eta^2}{(1+r)^2}-\dfrac{2}{(1+r)}\right)(1+2r)}}{2\left(9\eta^2-(1+2r)\right)}\right)}\cdot\frac{D_{crit}^{NCL}}{\eta} \qquad (3.7)$$

Once again, since this work is focused on bulk formability, the assumption of isotropy is acceptable, thus, by making $r=1$, equation (3.7) eventually results in equation (3.9).

$$\bar\varepsilon_f = \left(\frac{1+\dfrac{-(9\eta^2-6)-6\eta\sqrt{-3\left(\dfrac{9\eta^2}{4}-1\right)}}{2(9\eta^2-3)}}{2+\dfrac{-(9\eta^2-6)-6\eta\sqrt{-3\left(\dfrac{9\eta^2}{4}-1\right)}}{2(9\eta^2-3)}}\right)\frac{D_{crit}^{NCL}}{\eta} \qquad (3.8)$$

$$\bar\varepsilon_f = \left(\frac{9\eta^2-3\eta\sqrt{-3(9\eta^2-4)}}{(27\eta^2-6)-3\eta\sqrt{-3(9\eta^2-4)}}\right)\frac{D_{crit}^{NCL}}{\eta} \qquad (3.9)$$

Finally, equations (3.2) and (3.9) can be plotted in the space of effective strain vs. stress triaxiality, allowing for the representation of the McClintock (Figure 3.5a) and normalized Cockcroft-Latham (Figure 3.5b) criteria in this space.
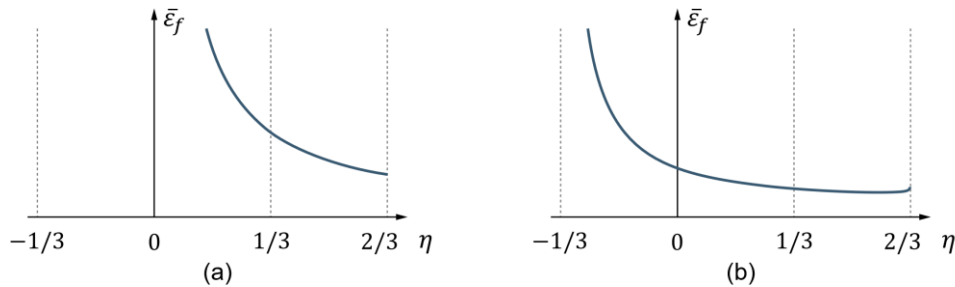
Figure 3.5 *Schematical representation of the (a) McClintock and the (b) normalized Cockcroft-Latham ductile damage criteria in the space of effective strain vs. stress triaxiality assuming isotropy.*

By also considering isotropy, equation (3.6) results in the following one, which allows for the graphical representation in Figure 3.6:

$$\frac{\sigma_1}{\bar{\sigma}} = \frac{(27\eta^2 - 6) - 3\eta\sqrt{-3(9\eta^2 - 4)}}{9\eta^2 - 3\eta\sqrt{-3(9\eta^2 - 4)}}\eta \tag{3.10}$$

It is clear from Figure 3.6 that beyond states of uniaxial tension, multiple values of stress triaxiality, η, may result in the same value for the normalized major principal stress component, $\sigma_1/\bar{\sigma}$, due to the parabolic-like behavior of the function, which also gives the curve a global maximum at $\eta = 1/\sqrt{3}$ (through-thickness plane strain).
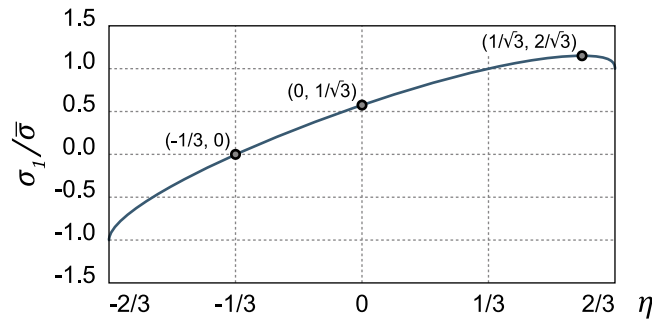
Figure 3.6 *Variation of the $\sigma_1/\bar{\sigma}$ ratio with stress triaxiality.*

A detailed step-by-step procedure for the obtainment of equations (3.4) to (3.6) is presented in Appendix A (Section A.4).

3.3 A new single uncoupled damage criterion built on the concept of fracture mode competition

Because of the existance of the uncertainty region that was introduced in Section 2.3, one can conclude that neither the McClintock (mode I) nor the normalized Cockcroft-Latham (mode III) ductile damage criteria are able to modulate the experimental fracture locus of a given material for stress-triaxiality values in the range $-1/3 \leq \eta \leq 2/3$, unless all fracture points fall solely on the mode III curve.

Nevertheless, the normalized Cockcroft-Latham criterion works well for stress states between uniaxial compression and uniaxial tension, $-1/3 \leq \eta < 1/3$, where cracks are triggered by out-of-plane shear (mode III). The suitability of the McClintock criterion (and an ever-present mode I) for the range $1/3 \leq \eta \leq 1/\sqrt{3}$ can be called into question due to the works of Kuhn et al. (1973), Erman et al. (1983), and Gouveia et al. (1996), which point out to single rather than dual fracture loci and culminate in the definition of the uncertainty region and fracture mode competition.

These results justify the creation of a new uncoupled ductile damage criterion that tackles this mode competition and that can properly handle the fracture forming limits in bulk forming for

$\eta \geq 1/3$ while maintaining the normalized Cockcroft-Latham criterion's suitability for $-1/3 \leq \eta < 1/3$.

Cerik and Choung (2020) proposed an uncoupled ductile damage criterion based on the combination of the integrands of the normalized maximum shear and Cockcroft-Latham criteria, $\tau_{max}/\bar{\sigma}$ and $\sigma_1/\bar{\sigma}$, as follows:

$$\left(C_1 \frac{\tau_{max}}{\bar{\sigma}} + (1 + C_1) \frac{\langle \sigma_1 \rangle}{\bar{\sigma}} \right)^{C_2} \bar{\varepsilon}_f =$$

$$\left(C_1 \left(\frac{1}{\sqrt{3}} cos \left[\frac{\pi}{6} \bar{\theta} \right] \right) + (1 - C_1) \left(\frac{\left\langle 3\eta + 2cos \left[\frac{\pi}{6}(1 - \bar{\theta}) \right] \right\rangle}{3} \right) \right)^{C_2} \bar{\varepsilon}_f = C_3 \tag{3.11}$$

where C_i are parameters to be experimentally determined and $\bar{\theta}$ is the normalized Lode angle.

Li et al. (2021) also proposed an uncoupled damage criterion resultant of the combination of the normalized Cockcroft-Latham and maximum shear criteria, claiming these are responsible for the coalescence of voids under tension and shear, respectively, and adding an exponential function of stress triaxiality to model void growth as in equation (3.12), where C_i are parameters to be experimentally determined.

$$\left[\left(\frac{2\tau_{max}}{\bar{\sigma}} \right)^{C_1} + \left\langle \frac{\sigma_1}{\bar{\sigma}} - 1 \right\rangle \right]^{C_2} exp \left(C_3 \left(\eta - \frac{1}{3} \right) \right) \bar{\varepsilon}_f = C_4 \tag{3.12}$$

However, due to the relation between the normalized Cockcroft-Latham criterion and the crack opening mode III (out-of-plane shear) that was addressed in Section 2.2.3, it may be concluded that the physics behind equation (3.11) is based on a weighted combination of two shear-based criteria, thus accounting only for distortional effects on void growth and coalescence while completely disregarding for dilatational ones. In Li et al.'s (2021) proposal the normalized Cockcroft-Latham criterion is also interpreted as a tension-based criterion, when it is in fact a shear-based one. Moreover, the stated control mechanisms of void growth and coalescence are not compatible with the theory developed by McClintock (1968), where voids grow and coalesce controlled by the same parameters in the two stages, whether this happens because of tension (equation (2.1)), shear (equation (2.2)), or a combination of both.

Nevertheless, equation (3.11) provides a relation between the integrand of the normalized Cockcroft-Latham criterion, $\sigma_1/\bar{\sigma}$, and the normalized Lode angle, $\bar{\theta}$, which can be rewritten in terms of the Lode angle parameter, ξ, as follows:

$$\frac{\sigma_1}{\bar{\sigma}} = \frac{3\eta + 2cos \left[\frac{\pi}{6}(1 - \bar{\theta}) \right]}{3} = \eta + \frac{2}{3} cos \left(\frac{cos^{-1} \xi}{3} \right) \tag{3.13}$$

The detailed procedure for the obtainment of equation (3.13) is presented in Section B.5 of Appendix B.

Figure 3.7 presents the graphical representation of equation (3.13), which has some similarities with the relation between stress-triaxiality, η, and the Lode angle parameters, ξ and $\bar{\theta}$, in Figure 2.13. However, contrary to $\eta = f(\xi)$, $\sigma_1/\bar{\sigma} = f(\xi)$ is not a true function for stress states beyond uniaxial tension (i.e., for $\sigma_1/\bar{\sigma} > 1$ or $1/3 \leq \eta \leq 2/3$) since different values of ξ, or $\bar{\theta}$, may result in equal values of $\sigma_1/\bar{\sigma}$. This, along with the local maximum for states of through-thickness plane strain, is compatible with the observations for the dependance of the normalized major stress component on stress triaxiality made in the previous section (Figure 3.6).
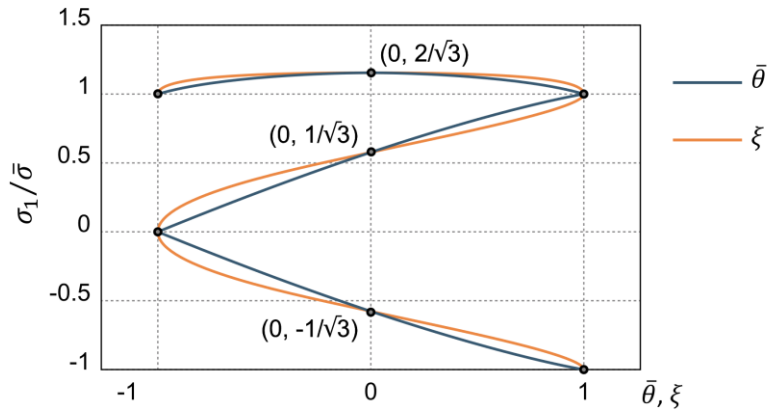
Figure 3.7 *Variation of $\sigma_1/\bar{\sigma}$ with the normalized Lode angle, $\bar{\theta}$, (blue curve) and the Lode angle parameter, ξ, (orange curve).*

Since the concept of fracture mode competition suggests an intertwining of mode I and III beyond uniaxial tension, similar to what did Cerik and Choung (2020) with equation (3.11), a new uncoupled ductile damage criterion may be proposed by combining the integrands of different criteria, one of them being the normalized Cockcroft-Latham one, since it presents a great suitability for out-of-plane shear-triggered cracking ($-1/3 \leq \eta < 1/3$). However, instead of using two shear-based criteria, a function that accounts for the dilatational effects on void growth and coalescence (that are directly related with crack opening by tension) should be considered when these effects start to be relevant ($\eta \geq 1/3$ – the uncertainty region). This justifies the following expression for the critical value of accumulated damage D_{crit}^{new} of the new criterion,

$$D_{crit}^{new} = \int_0^{\bar{\varepsilon}_f} \frac{\sigma_1}{\bar{\sigma}} d\bar{\varepsilon} + C \int_0^{\bar{\varepsilon}_f} \left\langle \eta - \frac{1}{3} \right\rangle^2 d\bar{\varepsilon} \equiv D(\mu) + D(\eta) \tag{3.14}$$

where C is a material parameter to be determined from experiments, and the second term in the right-hand side is a modified version of the McClintock criterion that due to the usage of the Macaulay brackets is only active in the 'uncertainty region' and that is squared to ensure a smooth transition with the remaining fracture locus modelled by the Cockcroft-Latham criterion, which by still being accounted for $\eta \geq 1/3$ states, along with a stress triaxiality-based term, proposes a combined influence of both shear and tension in the range of the uncertainty region, thus being

based on the concept of fracture mode competition (similarly to what occurs with Işık's, 2018, fracture risk criterion). The material parameter C is responsible for controlling the influence of tension in fracture in the uncertainty region, and its effect in the overall shape of the fracture locus is schematically depicted in Figure 3.8a.

Moreover, it makes sense that the normalized maximum shear criterion is not used for bulk forming, since the maximum shear stress does not always correspond to the largest through-thickness shear stress (see Figure 2.6), which is the one responsible for fracture initiation in mode III.

Figure 3.8b is a three-dimensional representation of the new damage criterion (with $C < 0$), in which the influence of the normalized Lode angle is observable. As in Figure 2.15, the damage criterion is represented by the red curve on the surface. This surface has no physical meaning in plane stress conditions and is used just for providing an easier spatial perception. The projection of this curve on a single $\bar{\varepsilon}_f = f(\eta)$ plane results in Figure 3.8a. The projection of the curve in a single $\eta = f(\bar{\theta})$ space results in the blue curve in Figure 2.13.
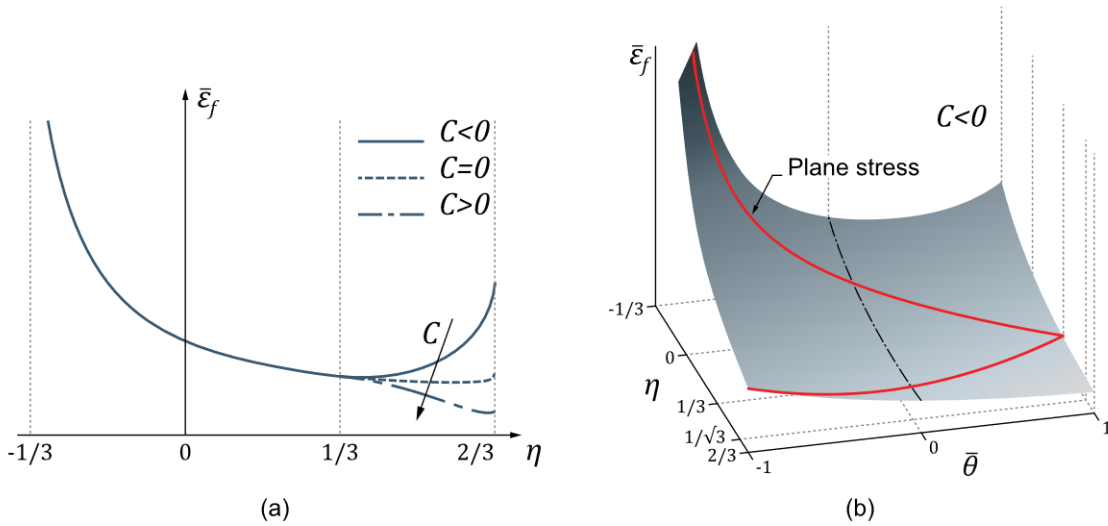
Figure 3.8 *Schematic representation of the fracture loci obtained with the newly proposed uncoupled ductile damage criterion in (a) the space of effective strain vs. stress triaxiality, evidencing the influence of the material parameter, C, and (b) the three dimensional space of η vs. $\bar{\theta}$ vs. $\bar{\varepsilon}_f$ with $C < 0$, evidencing the influence of the normalized Lode angle parameter, $\bar{\theta}$.*

The $\bar{\varepsilon}_f = f(\eta)$ curve depicted in Figure 3.8a can be easily obtained with the same procedure used for the McClintock and normalized Cockcroft-Latham in Section 3.2 and Işık's criteria in Section 2.2.7. By assuming proportional strain loading paths, equation (3.14) may be rewritten as follows:

$$\bar{\varepsilon}_f = \frac{D_{crit}^{new}}{\sigma_1/\bar{\sigma} + C\langle \eta - 1/3 \rangle^2} \tag{3.15}$$

By considering isotropy, the normalized major principal stress component, $\sigma_1/\bar{\sigma}$, can be expressed in terms of stress triaxiality, η, as in equation (3.10) and equation (3.15) results in the following one:

$$\bar{\varepsilon}_f = \frac{D_{crit}^{new}}{\frac{(27\eta^2 - 6) - 3\eta\sqrt{-3(9\eta^2 - 4)}}{9\eta^2 - 3\eta\sqrt{-3(9\eta^2 - 4)}}\eta + C\langle\eta - 1/3\rangle^2} \tag{3.16}$$

3.4 An Excel workbook to calibrate four uncoupled damage criteria

For purposes of damage evaluation and damage criteria calibration, an Excel workbook was developed with two widely used uncoupled ductile damage criteria, the McClintock one (due to Ayada et al., 1987, after McClintock, 1968) and the normalized Cockcroft-Latham one (due to Oh et al., 1979, after Cockcroft and Latham, 1968), and also with the fracture risk criterion (due to Işık, 2018) and the newly proposed damage criterion.

The Excel is therefore composed by seven sheets dedicated to:

   a. The McClintock damage criterion.
   b. The normalized Cockcroft-Latham damage criterion.
   c. The fracture risk criterion.
   d. The newly proposed damage criterion.
   e. A plot of the four criteria with the experimental data for comparison purposes.
   f. Plots of the stress triaxiality and the $\sigma_1/\bar{\sigma}$ ratio vs. the normalized Lode angle and the Lode angle parameter (Figure 2.13 and Figure 3.7) and another of the normalized maximum shear stress and the $\sigma_1/\bar{\sigma}$ ratio vs. stress triaxiality (Figure 2.14 and Figure 3.6) for illustration purposes.
   g. The calculations for the graphical representations of the damage criteria in the first sheets.

3.4.1 Worksheets for the criteria

The sheets for each individual criterion are all very similar. In these, one starts by inputting the various experimental results of stress triaxiality, η, and effective strain at fracture, $\bar{\varepsilon}_f$, and a scatter chart representing these results in the space of effective strain vs. stress triaxiality is presented.

Then, the criterion parameters are varied in order to adjust each criterion to the experimental values, i.e., the critical damage values for the McClintock and the normalized Cockcroft-Latham criteria, the material parameters A and B for the fracture risk criterion and the critical damage value and the material parameter C for the newly proposed criterion. The criteria are plotted (as schematically represented in Figure 3.5, Figure 2.16, and Figure 3.8, respectively) onto the scatter plot of the experimental results to allow the referred adjustment.

The four criteria are also plotted together onto the experimental data on the fifth worksheet in order to choose the best one out of those for the tested material.

Figure 3.9 presents a flow chart for the general procedure of damage evaluation and damage criteria calibration with this approach.
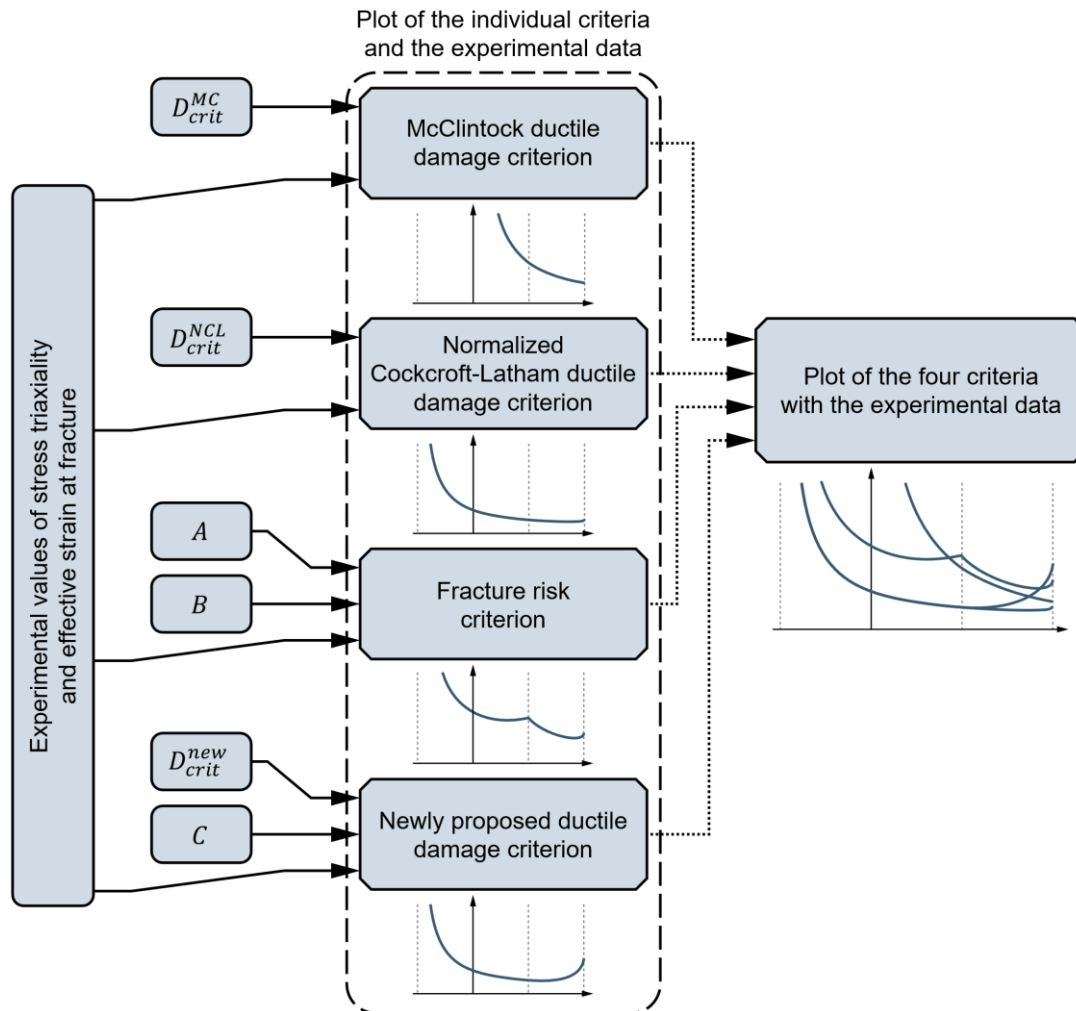
Figure 3.9 *Flow chart for the general procedure for damage evaluation and damage criteria calibration with a graphical approach considering the McClintock and normalized Cockcroft-Latham ductile damage criteria, the fracture risk criterion, and the newly proposed ductile damage criterion.*

It is important to notice that, since they are only calibrated with the value of critical damage, the damage evaluation for the McClintock and the normalized Cockcroft-Latham criteria could be done with a FEM analysis by simulating the material deformation until the point when experimental strains at fracture are achieved and recording the damage value at that instant at the site of fracture. However, this is not so easily accomplished when using Işık's (2018) criterion or the newly proposed one, since these rely on two material parameters rather than a single one. Hence, a graphical approach to damage evaluation and damage criteria calibration must be preferred, especially when considering criteria with multiple parameters.

In fact, as these criteria only provide estimates for the fracture loci, it is logical that the critical values of damage will not be the same for different stress states or even different test specimens, which means that a slight adjust of the obtained damage value is inevitable. Therefore, even single variable-based criteria should be calibrated with a graphical approach.

3.4.2 Calculations for the criteria

The plots of the criteria in their respective worksheets are based on calculations derived from equations (2.51), (3.1), and (3.2) for the case of the three first criteria, and from equation (3.15) for the newly proposed one.

In order to easily formulate all four criteria, the calculations of effective strain at fracture are not necessarily established on stress triaxiality. Instead, values for the principal stress components are introduced, varying as $0 \leq \sigma_1 \leq 1$, $-1 \leq \sigma_2 \leq 1$, and $-1 \leq \sigma_3 \leq 0$ and ensuring that, for every stress state, at least one of them is zero to create plane stress conditions. The fact that these components vary only between -1 and 1 is not problematic, as all final calculations are performed considering non-dimensional values.

With these values for the principal stress components, the effective, $\bar{\sigma}$, (considering the von Mises' yield criterion) and hydrostatic, σ_m, stresses for each stress state can be calculated from equations (3.17) and (3.18), respectively.

$$\bar{\sigma} = \sqrt{1/2} \left[(\sigma_1 - \sigma_2)^2 + (\sigma_2 - \sigma_3)^2 + (\sigma_3 - \sigma_1)^2 \right]^{1/2} \tag{3.17}$$

$$\sigma_m = \frac{\sigma_1 + \sigma_2 + \sigma_3}{3} \tag{3.18}$$

Then, the stress triaxiality, η, and the normalized maximum shear stress, $2\tau_{max}/\bar{\sigma}$, values (considering Tresca's yield criterion for the latter) are calculated from equations (3.19) and (3.20).

$$\eta = \frac{\sigma_m}{\bar{\sigma}} \tag{3.19}$$

$$\frac{2\tau_{max}}{\bar{\sigma}} = \frac{\sigma_1 - \sigma_3}{\bar{\sigma}} \tag{3.20}$$

These values already allow for the calculations necessary to represent the fracture locus for the McClintock damage criterion, since its integrand is the stress triaxiality itself, $g_{Mc} = \eta$. For the normalized Cockcroft-Latham criterion, the integrand is readily computed by just dividing the major principal stress component, σ_1, by the effective stress, $\bar{\sigma}$, i.e., $g_{NCL} = \sigma_1/\bar{\sigma}$. For the fracture risk criterion case, the integrand is calculated from equation (3.21), where A and B are the material parameters to be adjusted in the worksheet dedicated to this criterion, and for the new damage criterion, the integrand is calculated from equation (3.22), where C is the material parameter also to be adjusted in the dedicated worksheet.

$$g_{I\c{s}} = A\langle 1 + 3\eta \rangle + B\left(\frac{2\tau_{max}}{\bar{\sigma}} - 1\right) \tag{3.21}$$

$$g_{new} = {}^{\sigma_1}\!/_{\bar{\sigma}} + C\left\langle \eta - {}^1\!/_3 \right\rangle^2 \tag{3.22}$$

Finally, the effective strains at fracture for the several stress states according to the three criteria are calculated from equations (3.23) to (3.26), where proportional strain loading paths are assumed, and plotted against stress triaxiality in each criterion-dedicated sheet and in the one conceived for comparing the four criteria.

$$\left(\bar{\varepsilon}_f\right)_{Mc} = \frac{D_{crit}^{Mc}}{g_{Mc}} \tag{3.23}$$

$$\left(\bar{\varepsilon}_f\right)_{NCL} = \frac{D_{crit}^{NCL}}{g_{NCL}} \tag{3.24}$$

$$\left(\bar{\varepsilon}_f\right)_{I\c{s}} = \frac{1}{g_{I\c{s}}} \tag{3.25}$$

$$\left(\bar{\varepsilon}_f\right)_{new} = \frac{D_{crit}^{new}}{g_{new}} \tag{3.26}$$

where D_{crit}^{Mc}, D_{crit}^{NCL}, and D_{crit}^{new} are the critical values of damage for the McClintock, the normalized Cockcroft-Latham, and the newly proposed criteria, which are to be adjusted in each criterion-dedicated worksheet.

Additionally, a worksheet that provides a representation for the variation of the normalized maximum shear stress, $2\tau_{max}/\bar{\sigma}$, with stress triaxiality, η, and of the latter with both the normalized Lode angle, $\bar{\theta}$, and the Lode angle parameter, ξ, (as in Figure 2.13 and Figure 2.14) and of the normalized major principal stress component, $\sigma_1/\bar{\sigma}$, with stress triaxiality, η, and with both the normalized Lode angle, $\bar{\theta}$, and the Lode angle parameter, ξ, (as in Figure 3.6 and Figure 3.7) is provided, which allows for an easier understanding of the Lode parameters' influence on Işık's (2018) fracture risk criterion and the new ductile damage criterion. However, this worksheet was purely designed for this illustration purpose, since the normalized maximum shear stress used when computing the fracture locus according to Işık's (2018) criterion is calculated with the values for the principal stress components as in equation (3.20) and the normalized major principal stress component is calculated as already explained in this section. Nevertheless, these calculations would be necessary if the initially provided values were of stress triaxiality rather than the principal stress components, but this approach was chosen for making calculations easier for the normalized Cockcroft-Latham and the newly proposed ductile damage criteria.

Chapter 4

Experimental work

This chapter presents the experimental work performed during this thesis. First, the utilized testing equipment and methodology are described (Section 4.1), then the mechanical characterization of the tested material is presented (Section 4.2), and finally the bulk formability test specimens geometries that were used for the characterization of the fracture forming limits are provided and tabled (Section 4.3).

4.1 Testing equipment and methodology

Three main equipment were utilized throughout the experimental work: a hydraulic testing machine used for the material characterization and the upsetting of the bulk formability test specimens, a digital image correlation (DIC) system for the analysis of the strain vs. time evolutions during the upsetting, and a scanning electron microscope (SEM) for fractography analysis.

The hydraulic testing machine used, an Instron SATEC 1200 (Figure 4.1a), is able to perform both tensile and compression tests and presents a maximum loading capacity of 1200 kN, with crosshead velocities ranging from 0 to 200 mm/min and a maximum vertical opening of 2311 mm. For the upsetting, two parallel compression platens were coupled to the testing machine.

This machine is equipped with an Instron 5500 controller and connected to a load cell and a displacement transducer with a 0.001 mm resolution for the reading of both the applied force and the vertical displacement during testing. Test data is read and recorded using a computer equipped with the Instron *Bluehill 2* testing software.

To know and understand the history of fracture initiation and propagation contained in the surface morphology of visible cracks, fractography analyses by means of a Hitachi S-2400 scanning electron microscope (SEM) were conducted (Figure 4.1b). This SEM is equipped with Bruker *Quantax* energy dispersive X-ray spectrometer (EDS) light elements detector. It allows for the evaluation of samples with dimensions up to 40 x 40 x 40 [mm] with a maximum magnification of 5000 X.

The Q-400 3D digital image correlation (DIC) system from Dantec Dynamics (Figure 4.1c) was utilized in all the formability tests for the evaluation of the evolution of the on-surface (or in-plane) strains with time. It is equipped with a light source to illuminate the measuring regions on the

specimen and two 6 megapixels-resolution cameras with 50.2 focal lenses and f/8 aperture. The system is connected to a computer equipped with the *Instra 4D* software, which allows for an automatic calculation of strains through correlation of the images obtained from the two cameras.

(a)

(b)

(c)
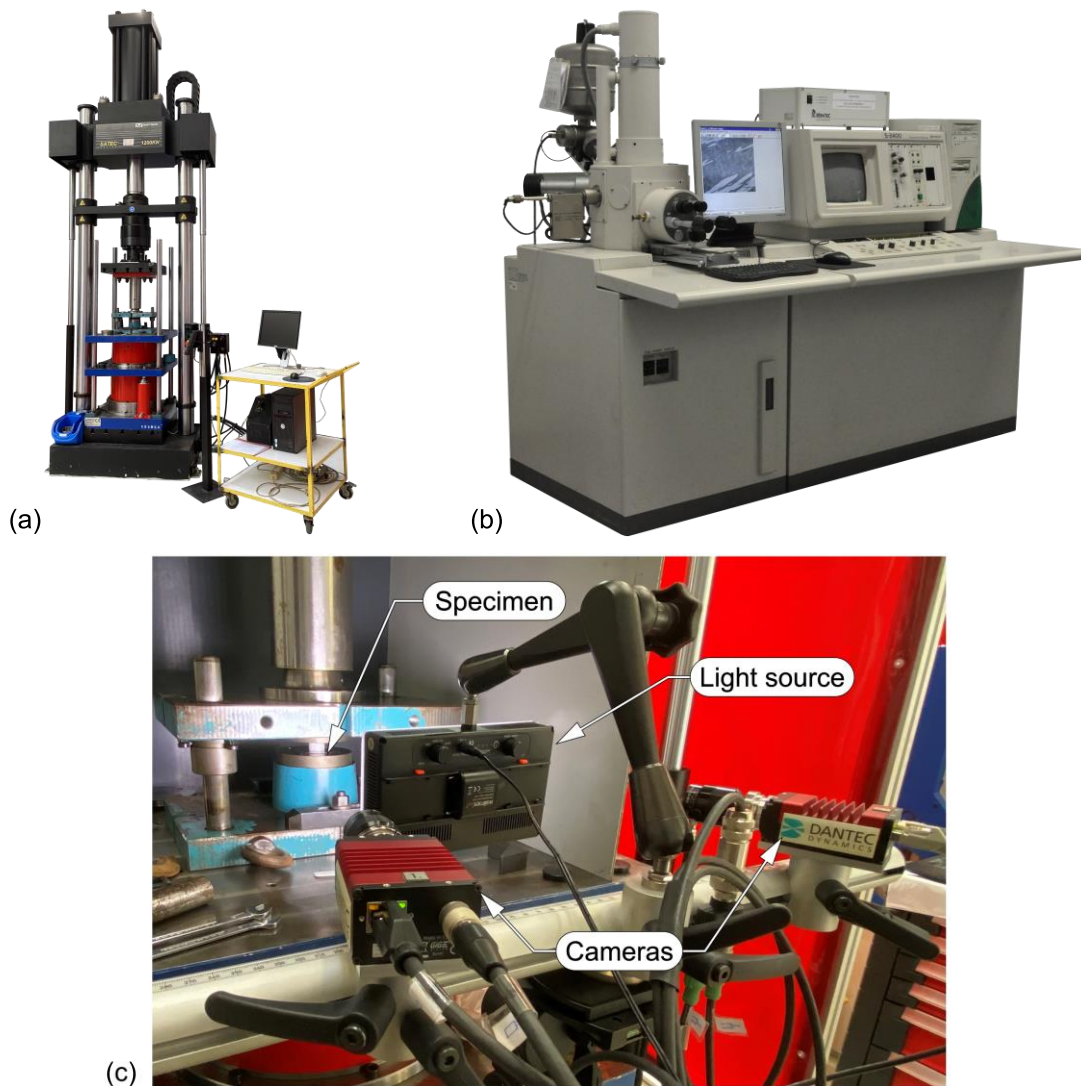
Figure 4.1 *(a) Instron SATEC 1200 hydraulic testing machine, (b) Hitachi S2400 scanning electron microscope with Bruker Quantax EDS light elements detector, and (c) Q-400 3D digital image correlation system in use during a cylinder upseting test.*

For the evaluation of the strain evolutions, the test specimens were made as large as possible to minimize the curvature on the surfaces of interest where cracks were triggered. These measuring regions were painted in white and then sprayed along the original gauge length to create a stochastic black speckle pattern, which allows for the strain calculations from image correlation. The cameras must be pointing at the illuminated measuring region, creating an angle between 40º and 60º (Figure 4.2a). During testing images were acquired with a frequency of 10 Hz (10 images per second).

Combining the evolutions of the on-surface strains and the upset force with time, the exact instant of the onset of cracking was acquired (Magrinho et al., 2018 – see Figure 4.2b). This experimental

procedure relies on the fact that a drop in the upset force marks the onset of cracking. The following crack propagation comes also with a sudden relief of stresses which makes it impossible for the DIC system to correlate the digital images obtained from the cracked regions of the specimens with accuracy.

The evolution of the strain loading paths in the principal in-plane strain space, $\varepsilon_1 = f(\varepsilon_2)$, (Figure 4.2c) is then computed by combining the evolutions of the major and minor strains with time. The evolutions in the strain vs. stress-triaxiality space, $\bar{\varepsilon} = f(\eta)$, (Figure 4.2d) are obtained from the transformation of the loading paths assuming plane stress conditions (see Section 2.2.4), which is admissible for the free outer surfaces where cracks are triggered.
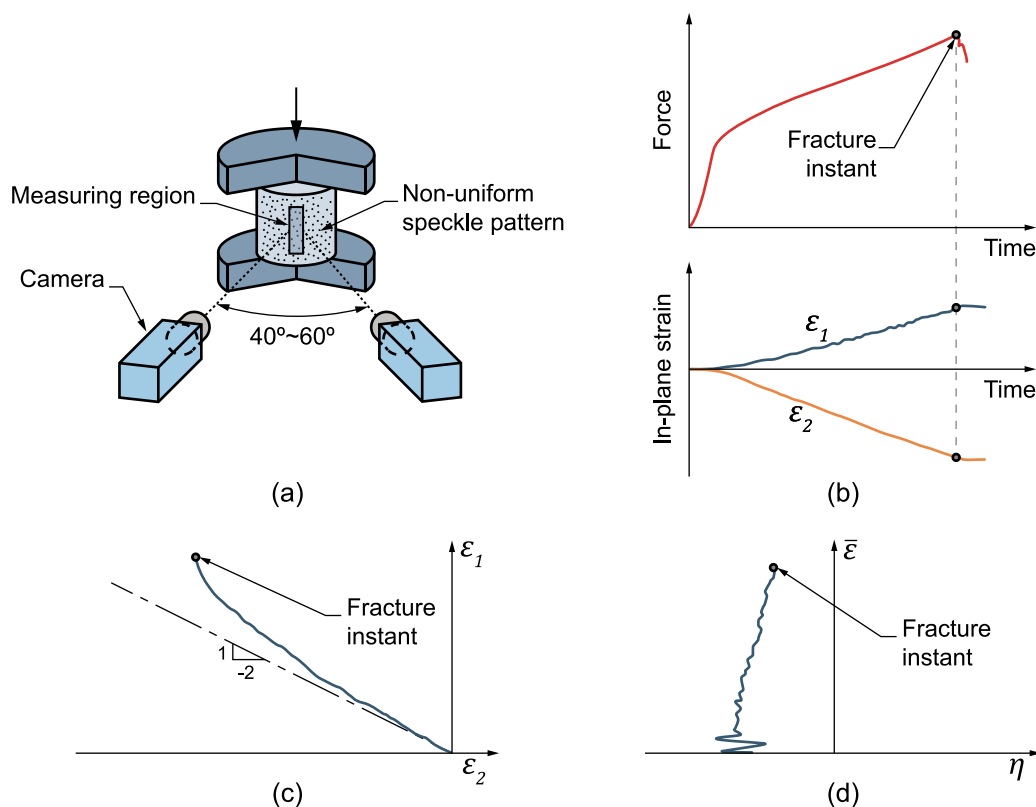
Figure 4.2 *Methodology to determine and plot the results obtained from the bulk formability tests: (a) schematic representation of the experimental setup utilized in digital image correlation (DIC), (b) combination of the load-time and strain-time evolutions showing the onset of cracking, (c) typical plot of a strain loading path determined by DIC in the principal strain space and (d) alternative representation in the effective strain vs. stress-triaxiality space.*

4.2 Mechanical characterization of the material

The experimental work was performed on commercial aluminum AA7075-T6 that was supplied in the form of solid rods with 200 mm diameter. The 'T6' in the material's name is for the heat treatment procedure utilized, meaning the material suffered a solution treatment, or anneal, and artificial ageing to allow precipitation hardening.

The flow stress curve (depicted in Figure 4.3) was determined by means of compression tests carried out on cylindrical test specimens with 25 mm of both height and diameter machined from the rods. The tests were conducted at room temperature on the Instron SATEC 1200 hydraulic testing machine described in Section 4.1 with a constant moving crosshead speed of 5 mm/min (0.083 mm/s) and the force vs. displacement results were converted to true stress vs. true strain through the following equations:

$$\bar{\varepsilon} = \ln\frac{h_0}{h_i} \quad \text{with} \quad h_i = h_0 - d \tag{4.1}$$

$$\bar{\sigma} = \frac{F_i}{A_i} \quad \text{with} \quad A_i = \frac{A_0 h_0}{h_i} \tag{4.2}$$

where h_0 and A_0 are the initial specimen height and area, and h_i and A_i are the specimen height and area for each instant of the test. F_i and d are the compressive force and the crosshead displacement at each instant that are registered by the testing machine.

As the right-hand side of equation (4.2) indicates, volume conservation is assumed for the calculations of the instantaneous area, A_i.
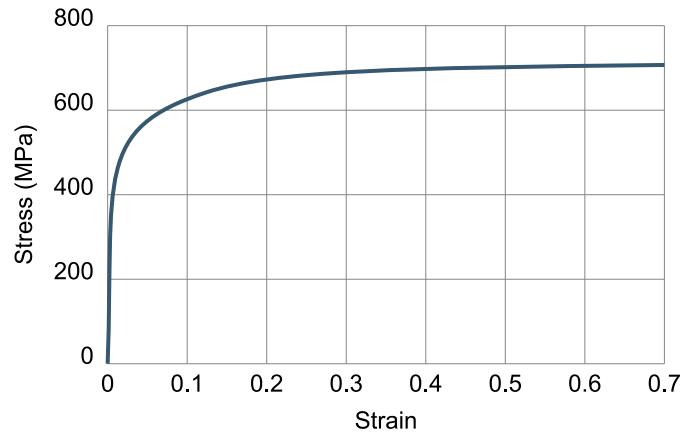
Figure 4.3 *Flow stress of the AA7075-T6 aluminum alloy.*

A molybdenum disulfide (MoS$_2$) based lubricant was applied on the top and bottom surfaces of the specimens in order to ensure near frictionless conditions and the compression platens had an average roughness, R_a, of 0.06 mm.

4.3 Bulk formability testing

The bulk formability tests were carried out at room temperature on the same hydraulic testing machine that was used in the mechanical characterization of the material. The same compression platens were used, but no lubricant was applied to avoid image caption problems if lubricant was to smudge the specimen when the DIC system was in use, or if the specimen was to flatten so much that the DIC system could not capture adequate pictures to correlate.

Axially-loaded conventional bulk formability specimens (cylindrical, tapered, and flanged) were tested along with the new barreled ring test specimen. These were machined in a CNC machining center from the supplied AA7075-T6 aluminum rods according to the geometries provided in Table 4.1, and later degreased before being compressed between flat parallel platens with a crosshead speed of 5 mm/min.

Figure 4.4 shows the experimental setup for the testing of the new barreled ring specimen. The black on white speckle pattern is evident in Figure 4.4b.

Table 4.1 *Geometry and lubrication conditions for the bulk formability test specimens.*

Geometry (mm)	Cylindrical	Tapered		Flanged	Barreled ring
H	25	25	25	25	50
D	25	30	35	35	170
d	–	25	25	25	90
t	–	5	5	5	6
h	–	–	–	–	28
D_i	–	–	–	–	158
Lubrication	Dry	Dry	Dry	Dry	Dry
Identification	c	t1	t2	f	br
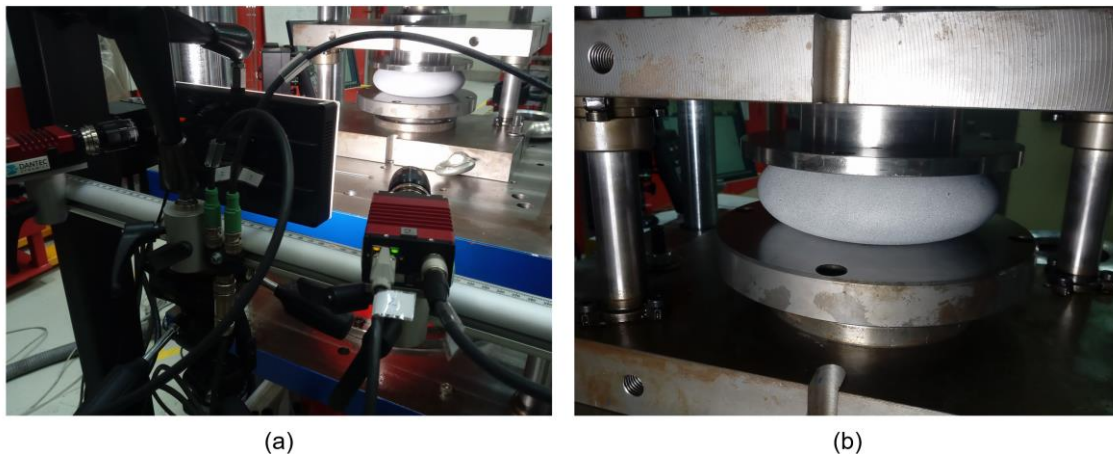
Figure 4.4 *(a) Experimental setup for the upset testing of the barreled ring specimen and (b) close-up photography of the specimen.*

Chapter 5

Results and discussion

Throughout this chapter, all the results from the experimental tests will be presented and discussed, starting from the distribution of the fracture points in the in-plane principal strain space, and subsequently shifting them to the space of effective strain vs. stress triaxiality (Section 5.1). Then, a fractography analysis of the fracture surface of the new barreled ring specimen is presented in order to, with the results provided in Section 5.1, discuss the crack opening mode for this specimen (Section 5.2). Finally, the suitability of some uncoupled damage criteria is assessed, namely that of the new one proposed in Section 3.3 (Section 5.3).

5.1 Bulk formability limits

The employment of the methodology described in Section 4.1 for the case of the barreled ring specimen is depicted in Figure 5.1a. Figure 5.1b portrays a comparison of the experimentally obtained loading paths with the one predicted by the FEM (see Section 3.1), proving a very good agreement between them. Figure 5.1c shows the graphical results obtained with DIC, in which 'Point 1' is the location where cracks were triggered, or the fracture initiation site.
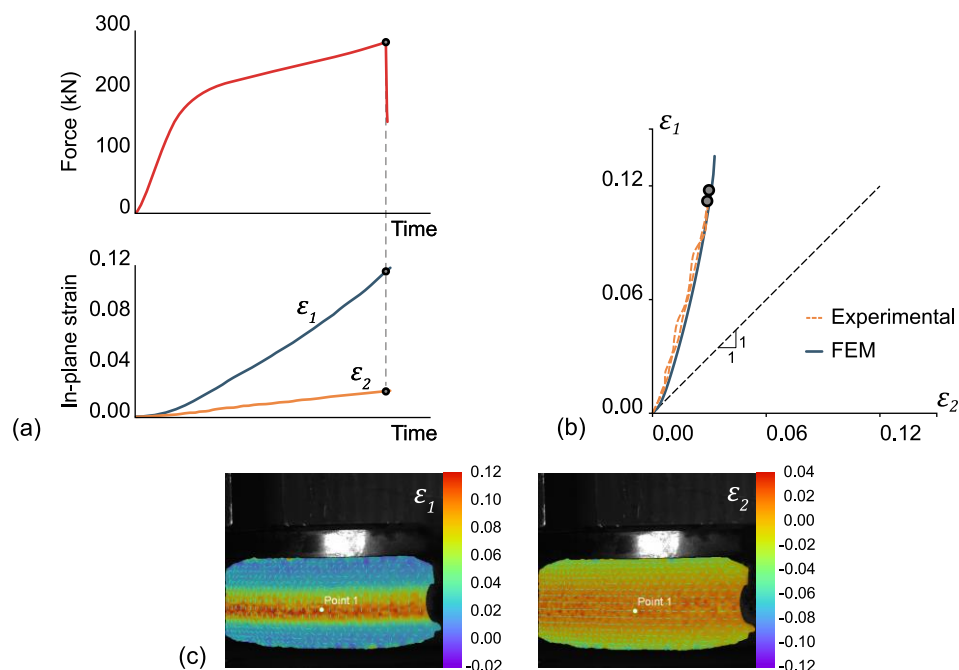
Figure 5.1 *(a) Summary of the methodology for determining the strain loading paths up to fracture for the new barreled ring specimen, (b) comparison between the FEM-predicted strain loading path and the experimental ones, and (c) DIC results at the instant of time right before fracture.*

Figure 5.2a shows the non-deformed and the fractured conventional test specimens, while Figure 5.2b shows the fractured barreled ring. It is interesting to note that the fracture runs radially on this last specimen, being a result of the opening mechanism in the longitudinal direction described in Section 3.1. However, the detail in Figure 5.2b reveals 'steps' on the crack, that indicate the existence of several crack initiation sites that are always located near the equatorial plane (as predicted) and that propagate until eventually find others and culminate in a single one.

(a)

(b)
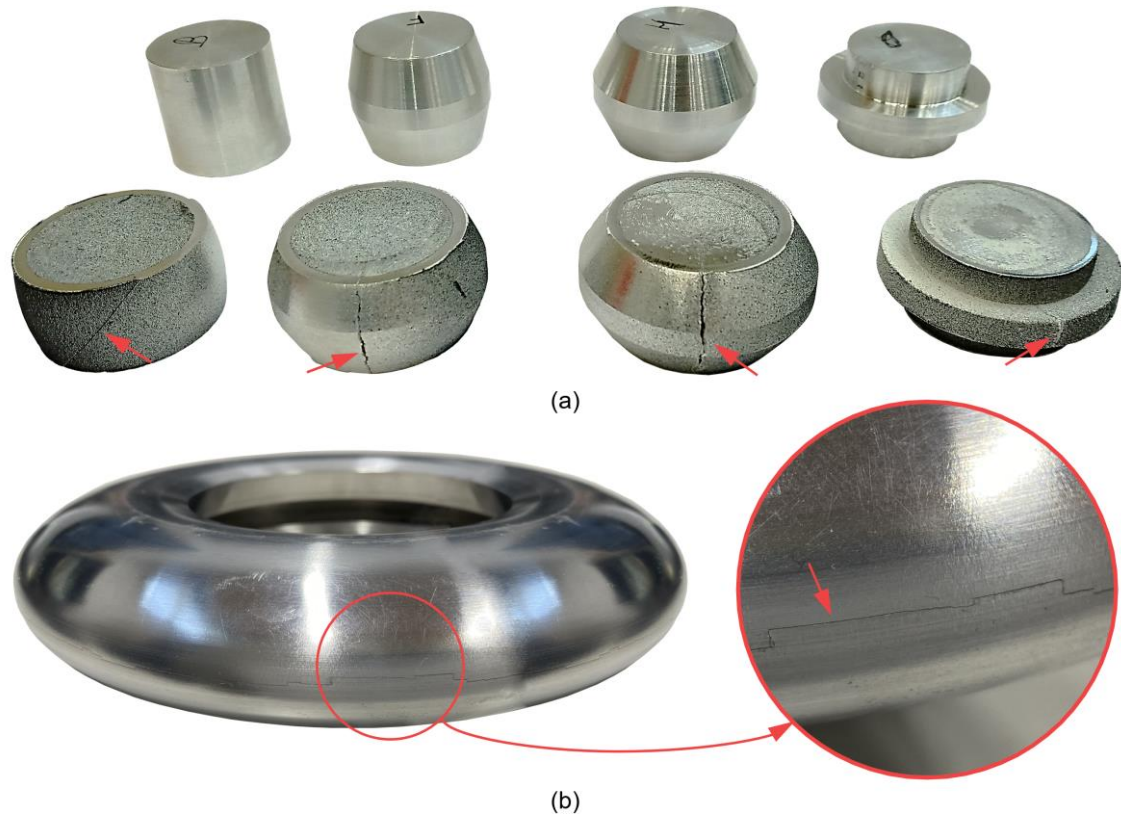
***Figure 5.2** (a) Non-deformed and fractured conventional bulk formability specimens, and (b) already fractured barreled ring specimen evidencing a radially-run fracture with detail depicting the 'crack steps'.*

The experimental loading paths up to fracture determined from DIC for all the specimens in Table 4.1 were obtained and plotted in the in-plane principal strain space (Figure 5.3a), $\varepsilon_1 = f(\varepsilon_2)$, and then shifted to the space of effective strain at fracture vs. stress triaxiality (Figure 5.3b), $\bar{\varepsilon}_f = f(\eta)$, using the transformation in equation (2.35). The lines for modes I and III in Figure 5.3a were adjusted to best fit the experimental results. The curves for the modes I and III of fracture mechanics in Figure 5.3b were obtained by using the expressions for $\bar{\varepsilon}_f = f(\eta)$ according to the McClintock (3.2) and normalized Cockcroft-Latham (3.9) criteria, respectively.

Every specimen geometry was tested at least thrice, but very close results were omitted from Figure 5.3. Nevertheless, there are two very close points for the barreled ring, as all tests performed with this specimen geometry resulted in very high agreement, with highly closeness when portraying the fracture loci in the in-plane principal strain space and in the space of effective strain at fracture vs. stress triaxiality.
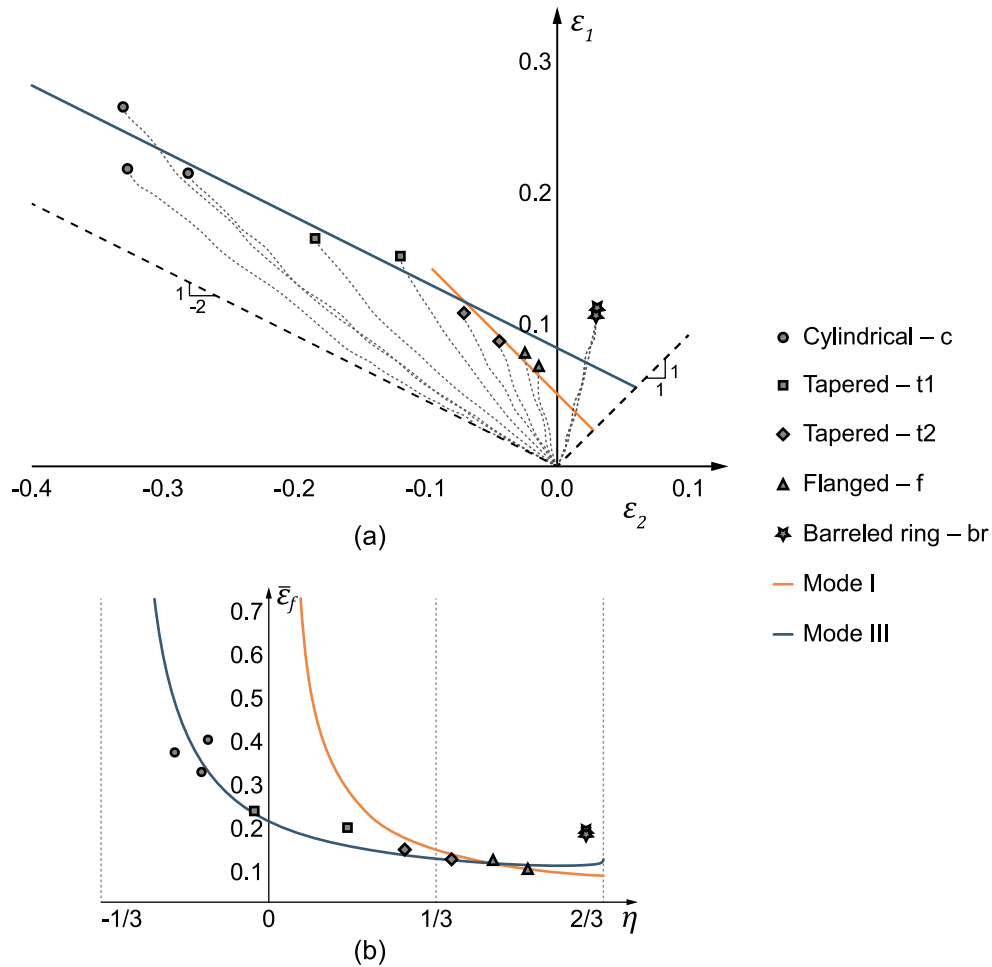
Figure 5.3 *Fracture loci corresponding to cracking by modes I and III together with the experimental values at fracture for the entire set of test cases in Table 4.1 (a) in the in-plane principal strain space with the respective strain loading paths, and (b) in the space of effective strain vs. stress triaxiality.*

As seen in Figure 5.3a, the fracture strains on the free surfaces of the various cylindrical and the four different tapered test specimens fall on a line with a slope of '-1/2', which is related to crack opening by out-of-plane shear (mode III), which are in close agreement with the ones obtained by Oh and Kobayashi (1976) for the same aluminum alloy, whereas the two flanged test specimens fall on a line with a slope of '-1', which is related to crack opening by tension (mode I). These results confirm the existence of a bilinear fracture locus as it was originally verified by Erman et al. (1983) and recently confirmed by Silva et al. (2015). However, the experimental results obtained for the barreled ring specimen do not fall on either of the previously mentioned fracture forming limit lines, defying the definition of bilinear fracture loci.

The fact that the tapered specimens are the ones defining the mode III to mode I transition is also in agreement with the works by Silva et al. (2015) and Magrinho et al. (2018) – see Section 2.2.5.

These results comply with the representation in the space of effective strain at fracture vs. stress triaxiality (Figure 5.3b), in which a bilinear fracture locus is also suitable for the conventional bulk specimens, but not for the barreled ring one, whose values of effective strain at fracture surpass both limit curves.

51

This non-compliance of the barreled ring with either crack opening mode limit line manifests the existence of an 'uncertainty region' that can slightly spread beyond the triangular area limited by the two fracture forming lines (see Figure 2.18) corresponding to the McClintock (mode I) and normalized Cockcroft-Latham (mode III) damage criteria. In fact, the maximum value of damage for the barreled ring considering the normalized Cockcroft-Latham criterion is $D_{max}^{NCL} = 0.18$, while the fracture locus for the mode III of fracture mechanics corresponds to $D_{crit}^{NCL} = 0.10$. For the McClintock criterion the values are $D_{max}^{Mc} = 0.10$ and $D_{crit}^{Mc} = 0.04$.

Additionally, a round tension specimen with the geometry portrayed in Figure 5.4a (ASTM, 2013) was tested on an Instron 4507 universal testing machine with a capacity of 200 kN and analyzed with the DIC system. The strain loading paths obtained from this analysis are depicted in Figure 5.4b, where it is clear that the resultant principal strains at fracture fall very close to those of one of the tapered-t2 specimens, meaning that the latter fairly replicates tension conditions on the specimen's outer surface with the benefit of having a bulk specimen under upsetting conditions, therefore approaching circumstances present in bulk manufacturing processes.
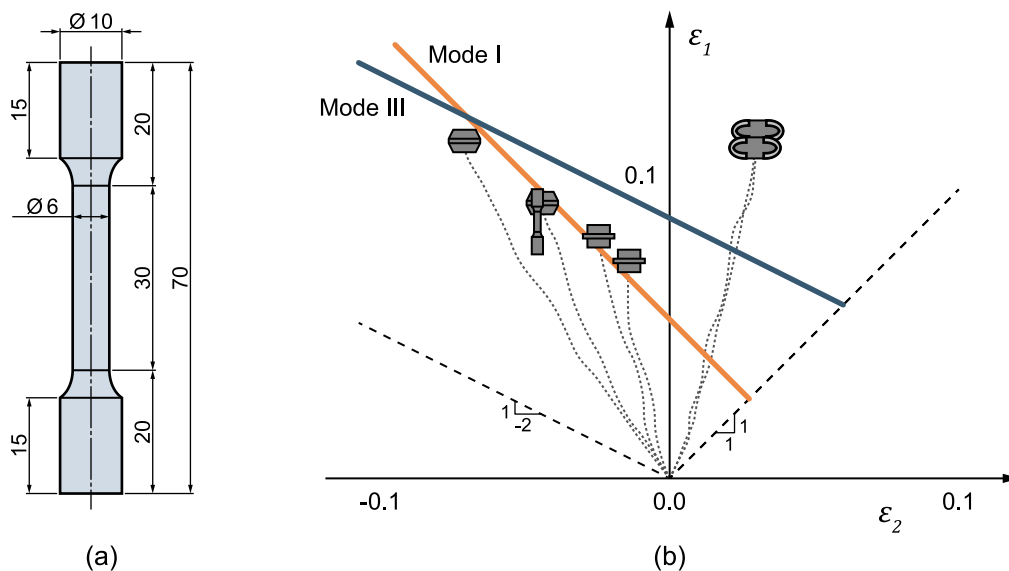
Figure 5.4 *(a) Geometry of the round tension specimen utilized (in conformance with the ASTM E8 / E8M - 13a standard – ASTM, 2013) and (b) representation of the principal strains at fracture for this specimen in the in-plane principal strain space, together with the ones already obtained and depicted in Figure 5.3 for the tapered-t2, flanged, and barreled ring specimens.*

5.2 Crack opening mode for the barreled ring

Although there were encountered differences between the critical values of damage at fracture and the maximum accumulated ones that were observed for the barreled ring specimen, numerical simulation and scanning electron microscope (SEM) observations point to a crack opening by out-of-plane shear (mode III).
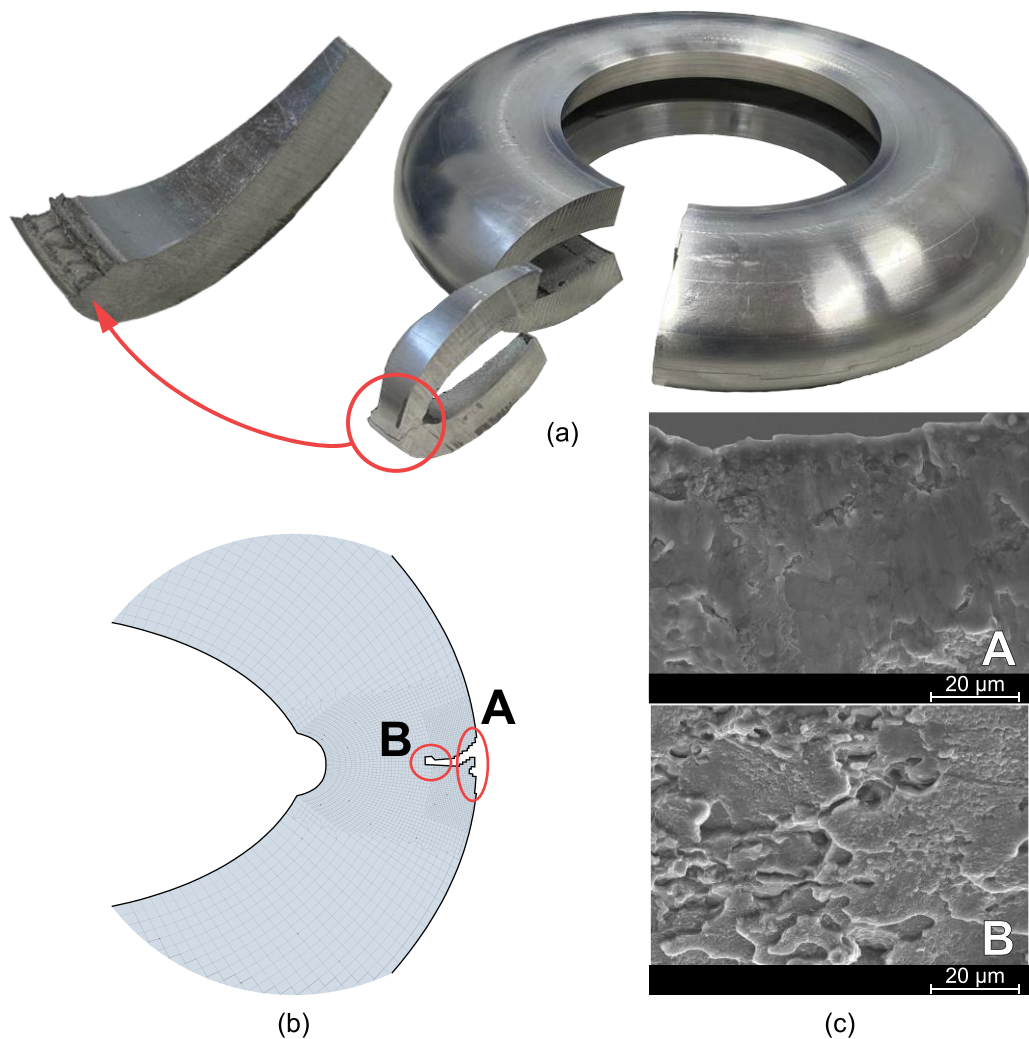
Figure 5.5 *(a) Picture of the barreled ring specimen after cracking, (b) finite element predicted onset and propagation of cracks and (c) fractography details disclosing crack opening by out-of-plane shear and subsequent propagation by tension.*

Figure 5.5b presents a FEM-predicted fracture onset and propagation using the normalized Cockcroft-Latham damage criterion, where elements were deleted upon reaching a critical value of damage. The image shows that element deletion may begin either on the upper or the lower side of the specimen, but always near the equator. This deletion eventually results in an inclined onset of fracture, typical of the crack opening mode III of fracture mechanics. This is in accordance with the fracture profile that is depicted in Figure 5.5a and the results from the SEM observations (refer to 'A' in Figure 5.5c), where a smooth crack surface, typical of shear, is visible.

Moreover, the fact that this inclined propagation may be located in the upper or lower surroundings of the specimen's equator, but then runs to the equatorial symmetry plane, explains the existence of the 'crack steps' visible in Figure 5.2b. This suggests that various crack fronts develop in the specimen at the same time, rapidly growing until connecting to each other, creating a single crack with 'crack steps', as speculated in the beginning of Section 5.1.

Further crack propagation occurs along the radial direction (refer to 'B' in Figure 5.5b). The crack surface morphology in this area is characterized by a dimple-based structure (refer to 'B' in Figure 5.5c), which is compatible with a tension-based fracture mechanism (mode I of fracture mechanics).

5.3 Assessing uncoupled ductile damage criteria: the advantage of the new one

The main conclusion that can be withdrawn from Figure 5.3 is that neither the McClintock (mode I) nor the normalized Cockcroft-Latham (mode III) ductile damage criteria can properly replicate the experimental values of effective strain at fracture, $\bar{\varepsilon}_f$, for the entire range of stress-triaxiality values that may exist in plane stress conditions, $-1/3 \leq \eta \leq 2/3$.

Figure 5.6 portrays the application of these two uncoupled damage criteria, along with the fracture risk criterion and the newly proposed one to the test specimens of Table 4.1 in the space of effective strain vs. stress triaxiality. The adjustment of the values for the various damage criteria (also in Figure 5.6) was made by means of the Excel program described in Section 3.4.
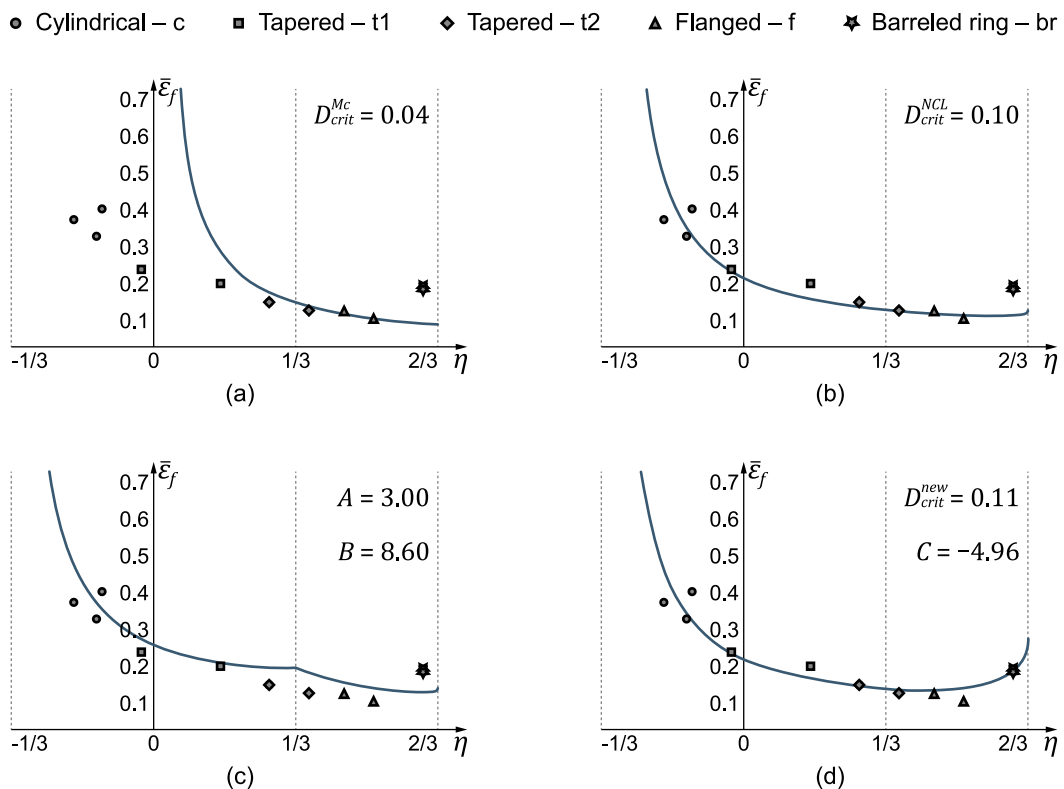
Figure 5.6 Application of different ductile damage criteria to the test specimens in Table 4.1 in the space of effective strain vs. stress triaxiality: (a) the McClintock, (b) the normalized Cockcroft-Latham, (c) the fracture risk, and (d) the newly proposed one.

As in this space the McClintock criterion is represented by a hyperbole with a vertical asymptote in $\eta = 0$ (Figure 5.6a), defined by equation (3.2), it can never modulate the whole range of stress triaxiality. Furthermore, as it is characterized by being a monotonically decreasing curve, it cannot replicate the experimental values for the barreled ring and for the rest of the specimens with a single curve, since the values for the effective strain at fracture, $\bar{\varepsilon}_f$, are higher for the barreled ring than those for the flanged or the tapered-t2 specimens. Nevertheless, as this criterion characterizes mode I of fracture mechanics, it adapts well to the results from the flanged specimens, $1/3 \leq \eta \leq 1/\sqrt{3}$, in which cracks are triggered by tension rather than shear.

Since it characterizes mode III of fracture mechanics (see Section 2.2.3), the normalized Cockcroft-Latham criterion works well in the range $-1/3 \leq \eta < 1/3$, where cracks are triggered by out-of-plane shear. This criterion is also defined by a hyperbolic-like curve with a vertical asymptote at $\eta = -1/3$ and that rises slightly when approaching states of equibiaxial expansion, $\eta = 2/3$ (Figure 5.6b). However, this rising is so minimal that it is not enough to replicate the experimental values of effective strain at fracture, $\bar{\varepsilon}_f$, for the barreled ring specimen (states of expansion $1/\sqrt{3} < \eta \leq 2/3$), when also considering the other specimens.

The fracture risk criterion cannot be adjusted to these values of effective strain at fracture without creating a local maximum at $\eta = 1/3$ (Figure 5.6c), a characteristic feature of sheet formability, due to the passage of modes II to I of fracture mechanics. In Section 3.3 the unsuitability of damage criteria built on the maximum shear criterion was already stated, but because this criterion was developed for the replication of formability limits in sheet-bulk forming, it was decided for it to be studied for bulk formability to assess how it would fit.

As the experimental results in this work do not point to the existence of a local maximum at $\eta = 1/3$, and this is not a characteristic of bulk forming, it can be concluded that this criterion does not fit well to bulk formability.

Considering now the newly proposed ductile damage criterion, it is clear that, although one of the flanged specimens falls somewhat below the curve, there is an equal amount of points that fall above and below it (Figure 5.6d). Moreover, the characteristic drop in the values of effective strain at fracture for stress triaxiality ranging from $-1/3$ to $1/3$ is present, while still creating the rising behavior for $\eta > 1/3$. This result proves that it is in fact possible to use a single criterion to define the formability limits by fracture in bulk metal forming.

Additionally, a FEM-predicted damage distribution in the barreled ring specimen according to the newly proposed damage criterion was obtained (Figure 5.7). As one can see, the damage still accumulates mostly at the specimen's equator and on the outer surface, where fracture was seen to initiate (Figure 5.5), proving the new criterion predicts well the damage concentration regions.
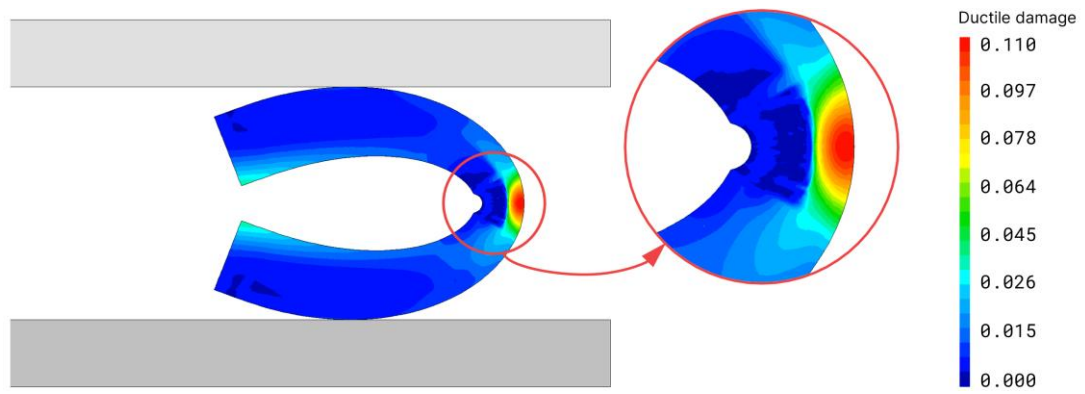
Figure 5.7 *FEM-predicted ductile damage distribution in the barreled ring specimen according to the newly proposed ductile damage criterion.*

Chapter 6

Conclusions and future work

This last chapter presents the most relevant conclusions that can be drawn from the results presented in the previous sections. Furthermore, it closes with proposals for eventual future works and studies to follow the ones presented in this thesis.

The barreled ring specimen allows, for the first time ever, to replicate biaxial tension states on a free external surface (providing plane stress conditions) in bulk metal forming, while allowing for a DIC evaluation of the on-surface strain evolutions. This, together with the conventional bulk formability test specimens, allows for the full characterization of the fracture limits in bulk metal forming.

Experimental results of effective strain at fracture for the barreled ring show that the 'uncertainty region' can spread past the modes I and III defining curves, and fractographies of the fracture surface morphology allow for the understanding of a competition between these modes – the new barreled ring specimen is a good example of this competition because cracks are triggered by shear and propagate radially by tension. Hence, it can be concluded that the usually employed McClintock and normalized Cockcroft-Latham damage criteria cannot be considered past stress triaxiality values of $\eta = 1/\sqrt{3}$.

Based on this competition, an uncoupled ductile damage criterion was developed, whose single-handed utilization allows for the characterization of the fracture loci in the whole range of stress triaxiality values compatible with plane stress conditions, $-1/3 \leq \eta \leq 2/3$. However, for being a result of mode competition, this criterion is incapable of distinguishing between fracture triggering in mode I or mode III of fracture mechanics beyond uniaxial tension, $\eta \geq 1/3$. Nevertheless, the curve defined by this criterion is able to fairly fit all the experimental values of effective strain at fracture presented in this thesis. The criterion is also still able to correctly predict the location of damage accumulation in a bulk formability specimen.

This new criterion, together with the new barreled ring specimen, is highly important for manufacturing processes where localized plastic deformation creates biaxial tensile stress states.

An analytical expression for the integrand of the normalized Cockcroft-Latham damage criterion (and thus mode III of fracture mechanics) was derived. That, combined with another that already existed for mode I, allows for the shift from the in-plane principal strain space to the space of effective strain vs. stress triaxiality in bulk metal forming for the whole range of stress triaxiality values compatible with plane stress conditions, $-1/3 \leq \eta \leq 2/3$. The graphical variation of the

normalized major principal stress component, $\sigma_1/\bar{\sigma}$, with both stress triaxiality and the Lode parameters was also portrayed.

An observation that arises from the relations that the normalized major principal stress component and the normalized maximum shear stress, $\tau_{max}/\bar{\sigma}$, have with the Lode parameters is that the importance of the latter in the formulation of damage criteria for plane stress conditions can be interpreted as a significance for the accounting of shear, and thus the distortional effects of void growth.

Moreover, it was proved that damage or fracture criteria developed for sheet-bulk forming are not appropriate to be applied to bulk forming, for they have a strong dependency on the rising of effective strains at fracture when approaching uniaxial tension, a characteristic feature of mode II of fracture mechanics, and thus sheet metal forming. Normalized maximum shear stress-based criteria are also not suitable for analyzing bulk formability, since the maximum shear stress is not always acting on the planes normal to the outer surface of the material (through-thickness – see Figure 2.6). In fact, this non suitability of the maximum shear criteria in bulk forming can also be verified by comparing the graphical representations of the normalized maximum shear stress and the normalized major principal stress component with stress triaxiality (Figure 2.14 and Figure 3.6), which show, respectively, double and single local maxima, where the rightmost one in Figure 2.14 corresponds to the single one in Figure 3.6, meaning the leftmost local maximum in the former corresponds to the accounting for in-plane shear stresses that are larger than the out-of-plane (or through-thickness) ones for stress states between uniaxial compression and uniaxial tension $(-1/3 < \eta < 1/3)$.

Additionally, it was shown that resulting values for strains at fracture for wider tapered specimens and round tension specimens are in very close agreement, meaning that the former fairly replicate tensile stress conditions on the specimen's surface, thus being these the specimens that dictate the mode III to mode I transition.

The logical path to follow this thesis involves the development of a series of new specimens, or configurations, based on the barreled ring that allow for the total sweep of the whole range of stress triaxiality values for plane stress conditions in bulk metal forming.

The utilization of different materials, both more and less ductile and anisotropic, together with these future configurations of the barreled ring is also suggested to truly verify the behavior in the uncertainty region and the aptitude of the new criterion.

More than that, different configurations that allow for expansion with the azimuthal strain, ε_θ, being larger than the longitudinal one, ε_z, (rather than the opposite, as it occurs in the specimen developed in this thesis) may simplify the geometry of the barreled ring, allowing for an easier manufacturing.

References

ASTM International. (2013). *ASTM E8 / E8M - 13ª: Standard Test Methods for Tension Testing of Metallic Materials*. Wes Conshohocken, PA: American Society for Testing and Materials.

Atkins, A. G. (1996). Fracture in forming. *Journal of Materials Processing Technology*, *56*(1), 609–618. https://doi.org/10.1016/0924-0136(95)01875-1.

Atkins, A. G., & Mai, Y.-M. (1985). *Elastic and Plastic Fracture: Metals, Polymers, Ceramics, Composites, Biological Materials* (1st ed.). New York, NY: John Wiley & Sons.

Ayada, M., Higashino, T., & Mori, K. (1987). Central Bursting in Extrusion of Inhomogeneous Materials. *Proceedings of the Second International Conference on Technology of Plasticity, Vol. I*, 553–558. Stuttgart.

Bai, Y., & Wierzbicki, T. (2008). A new model of metal plasticity and fracture with pressure and Lode dependence. *International Journal of Plasticity*, *24*(6), 1071–1096. https://doi.org/10.1016/j.ijplas.2007.09.004.

Bai, Y., & Wierzbicki, T. (2010). Application of extended Mohr–Coulomb criterion to ductile fracture. *International Journal of Fracture*, *161*(1), 1. https://doi.org/10.1007/s10704-009-9422-8.

Bao, Y., & Wierzbicki, T. (2004). On fracture locus in the equivalent strain and stress triaxiality space. *International Journal of Mechanical Sciences*, *46*(1), 81–98. https://doi.org/10.1016/j.ijmecsci.2004.02.006.

Brozzo, P., Deluca, B., & Rendina, R. (1972). A new method for the prediction of formability limits in metal sheets, sheet metal forming and formability. *7th Biennial Conference of the International Deep Drawing Research Group*. Amsterdam.

Caddell, R. M., & Atkins, A. G. (1968). The Influence of Redundant Work When Drawing Rods Through Conical Dies. *Journal of Engineering for Industry*, *90*(2), 411–416. https://doi.org/10.1115/1.3604653.

Cerik, B. C., & Choung, J. (2020). Ductile Fracture Behavior of Mild and High-Tensile Strength Shipbuilding Steels. *Applied Sciences, 10*(20). https://doi.org/10.3390/app10207034.

Chen, W.-F. (1982). *Plasticity in Reinforced Concrete* (1st ed.). New York, NY: McGraw-Hill.

Christiansen, P., Nielsen, C. V., Bay, N., & Martins, P. A. F. (2016). Internal shear cracking in bulk metal forming. *Proceedings of the Institution of Mechanical Engineers, Part L: Journal of Materials: Design and Applications*, *233*(4), 603–614. https://doi.org/10.1177/1464420716681592.

Cockcroft, M. G., & Latham, D. J. (1968). Ductility and the Workability of Metals. *Journal of the Institute of Metals*, *96*, 33–39.

Erman, E., Kuhn, H. A., & Fitzsimons, G. (1983). Novel Test Specimens for Workability Testing. In R. Chait & R. Papirno (Eds.), *Compression Testing of Homogeneous Materials and Composites* (pp. 279–290). West Conshohocken, PA: ASTM International. https://doi.org/10.1520/STP36209S.

Freudenthal, A. M. (1950). *The Inelastic Behavior of Engineering Materials and Structures* (1st ed.). New York, NY: John Wiley & Sons.

Goodwin, G. M. (1968). *Application of Strain Analysis to Sheet Metal Forming Problems in the Press Shop*. SAE technical paper 680093. https://doi.org/10.4271/680093.

Gouveia, B. P. P. A., Rodrigues, J. M. C., & Martins, P. A. F. (1996). Fracture predicting in bulk metal forming. *International Journal of Mechanical Sciences*, *38*(4), 361–372. https://doi.org/10.1016/0020-7403(95)00069-0.

Gurson, A. L. (1977). Continuum Theory of Ductile Rupture by Void Nucleation and Growth: Part I—Yield Criteria and Flow Rules for Porous Ductile Media. *Journal of Engineering Materials and Technology*, *99*(1), 2–15. https://doi.org/10.1115/1.3443401.

Hancock, J. W., & Mackenzie, A. C. (1976). On the mechanisms of ductile failure in high-strength steels subjected to multi-axial stress-states. *Journal of the Mechanics and Physics of Solids*, *24*, 147–169. https://doi.org/10.1016/0022-5096(76)90024-7.

Hill, R. (1948). A theory of the yielding and plastic flow of anisotropic metals. *Proceedings of the Royal Society of London. Series A. Mathematical and Physical Sciences*, *193(1033)*, 281–297. https://doi.org/10.1098/rspa.1948.0045.

Işık, K. (2018). *Modelling and characterization of damage and fracture in sheet-bulk metal forming* (Doctoral dissertation). Technischen Universität Dortmund, Dortmund.

Johnson, G. R., & Cook, W. H. (1985). Fracture characteristics of three metals subjected to various strains, strain rates, temperatures and pressures. *Engineering Fracture Mechanics*, *21*(1), 31–48. https://doi.org/10.1016/0013-7944(85)90052-9.

Kachanov, L. M. (1958). О времени разрушения в условиях ползучести [Rupture time under creep conditions]. *Izvestiya Akademii Nauk SSSR, Otdelenie Teckhnicheskikh Nauk*, *8*, 26–31. https://doi.org/10.1023/A:1018671022008.

Keeler, S. P. (1968). *Circular Grid System — A Valuable Aid for Evaluating Sheet Metal Formability*. SAE technical paper 680092. https://doi.org/10.4271/680092.

Kobayashi, S. (1970). Deformation Characteristics and Ductile Fracture of 1040 Steel in Simple Upsetting of Solid Cylinders and Rings. *Journal of Engineering for Industry*, *92*(2), 391–398. https://doi.org/10.1115/1.3427752.

Kuhn, H. A., & Lee, P. W. (1971). Strain instability and fracture at the surface of upset cylinders. *Metallurgical and Materials Transactions B*, *2*(11), 3197–3202. https://doi.org/10.1007/BF02814972.

Kuhn, H. A., Lee, P. W., & Erturk, T. (1973). A Fracture Criterion for Cold Forming. *Journal of Engineering Materials and Technology*, *95*(4), 213–218. https://doi.org/10.1115/1.3443155.

Lemaitre, J. (1985). A Continuous Damage Mechanics Model for Ductile Fracture. *Journal of Engineering Materials and Technology*, *107*(1), 83–89. https://doi.org/10.1115/1.3225775.

Lemaitre, J., & Chaboche, J.-L. (1985). *Mécanique des matériaux solides* (1st ed.). Paris: Dunod.

Leonardo, P. N. C., Magrinho, J. P., Bragança, I. M. F., Silva, M. B., Silva, C. M. A., & Martins, P. A. F. (2020). Formability limits in sheet-bulk forming. *International Journal of Machine Tools and Manufacture*, *149*. https://doi.org/10.1016/j.ijmachtools.2019.103509.

Li, X., Yang, W., Xu, D., Ju, K., & Chen, J. (2021). A new ductile fracture criterion considering both shear and tension mechanisms on void coalescence. *International Journal of Damage Mechanics*, *30*(3), 374–398. https://doi.org/10.1177/1056789520962831.

Lode, W. (1926). Versuche über den Einfluß der mittleren Hauptspannung auf das Fließen der Metalle Eisen, Kupfer und Nickel. *Zeitschrift Für Physik*, *36*(11), 913–939. https://doi.org/10.1007/BF01400222.

Lou, Y., Huh, H., Lim, S., & Pack, K. (2012). New ductile fracture criterion for prediction of fracture forming limit diagrams of sheet metals. *International Journal of Solids and Structures*, *49*(25), 3605–3615. https://doi.org/10.1016/j.ijsolstr.2012.02.016.

Magrinho, J. P., Silva, M. B., Alves, L. M., Atkins, A. G., & Martins, P. A. F. (2018). New methodology for the characterization of failure by fracture in bulk forming. *The Journal of Strain Analysis for Engineering Design*, *53*(4), 242–247. https://doi.org/10.1177/0309324718758842.

Marciniak, Z., & Kuczyński, K. (1967). Limit strains in the processes of stretch-forming sheet metal. *International Journal of Mechanical Sciences*, *9*(9), 609–620. https://doi.org/10.1016/0020-7403(67)90066-5.

Martins, P. A. F., Bay, N., Tekkaya, A. E., & Atkins, A. G. (2014). Characterization of fracture loci in metal forming. *International Journal of Mechanical Sciences*, *83*, 112–123. https://doi.org/10.1016/j.ijmecsci.2014.04.003.

McClintock, F. A. (1968). A Criterion for Ductile Fracture by the Growth of Holes. *Journal of Applied Mechanics*, *35*(2), 363–371. https://doi.org/10.1115/1.3601204.

Mendelson, A. (1986). *Plasticity: Theory and Application* (1st ed.). New York, NY: Macmillan.

Nielsen, C. V., & Martins, P. A. F. (2021). *Metal Forming: Formability, Simulation, and Tool Design* (1st ed.). New York, NY: Academic Press.

Nielsen, C. V., Zhang, W., Alves, L. M., Bay, N., & Martins, P. A. F. (2013). *Modeling of Thermo-Electro-Mechanical Manufacturing Processes: Applications in Metal Forming and Resistance Welding* (P. Davim (ed.); 1st ed.). London: Springer-Verlag.

Oh, S. I., Chen, C. C., & Kobayashi, S. (1979). Ductile Fracture in Axisymmetric Extrusion and Drawing—Part 2: Workability in Extrusion and Drawing. *Journal of Engineering for Industry*, *101*(1), 36–44. https://doi.org/10.1115/1.3439471.

Oh, S. I., & Kobayashi, S. (1976). Workability of aluminum alloy 7075-T6 in upsetting and rolling. *Journal of Manufacturing Science and Engineering*, *98*(3), 800–806. https://doi.org/10.1115/1.3439032.

Oyane, M. (1972). Criteria of Ductile Fracture Strain. *Bulletin of JSME*, *15*(90), 1507–1513. https://doi.org/10.1299/jsme1958.15.1507.

Rice, J. R., & Tracey, D. M. (1969). On the ductile enlargement of voids in triaxial stress fields. *Journal of the Mechanics and Physics of Solids*, *17*(3), 201–217. https://doi.org/10.1016/0022-5096(69)90033-7.

Rodrigues, J. M. C., & Martins, P. A. F. (2010). *Tecnologia Mecânica – Tecnologia da Deformação Plástica: Vol. I – Fundamentos teóricos* (2nd ed.). Lisboa: Escolar Editora.

Sachs, G., Eisbein, W., Kuntze, W., & Linicus, W. (1931). Versuche über die Eigenschaften gezogener Drähte und den Kraftbedarf beim Drahtziehen. In G. Sachs, W. Eisbein, W. Kuntze, & W. Linicus (Eds.), *Spanlose Formung der Metalle* (pp. 38–67). Springer Berlin Heidelberg. https://doi.org/10.1007/978-3-642-99086-1_3.

Shima, S., & Oyane, M. (1976). Plasticity theory for porous metals. *International Journal of Mechanical Sciences*, *18*(6), 285–291. https://doi.org/10.1016/0020-7403(76)90030-8.

Silva, C. M. A., Alves, L. M., Nielsen, C. V., Atkins, A. G., & Martins, P. A. F. (2015). Failure by fracture in bulk metal forming. *Journal of Materials Processing Technology*, *215*, 287–298. https://doi.org/10.1016/j.jmatprotec.2014.08.023.

Tai, W. H., & Yang, B. X. (1987). A new damage mechanics criterion for ductile fracture. *Engineering Fracture Mechanics*, *27*(4), 371–378. https://doi.org/10.1016/0013-7944(87)90174-3.

Tekkaya, A. E. (2018). Energy saving by manufacturing technology. Procedia Manufacturing, 21, 392–396. https://doi.org/10.1016/j.promfg.2018.02.146.

Tvergaard, V. (1981). Influence of voids on shear band instabilities under plane strain conditions. *International Journal of Fracture*, *17*(4), 389–407. https://doi.org/10.1007/BF00036191.

Tvergaard, V., & Needleman, A. (1984). Analysis of the cup-cone fracture in a round tensile bar. *Acta Metallurgica*, *32*(1), 157–169. https://doi.org/10.1016/0001-6160(84)90213-X.

Vujovic, V., & Shabaik, A. H. (1986). A New Workability Criterion for Ductile Metals. *Journal of Engineering Materials and Technology*, *108*(3), 245–249. https://doi.org/10.1115/1.3225876.

Weck, A., & Wilkinson, D. S. (2008). Experimental investigation of void coalescence in metallic sheets containing laser drilled holes. *Acta Materialia*, *56*(8), 1774–1784. https://doi.org/10.1016/j.actamat.2007.12.035.

Westergaard, H. M. (1920). On the resistance of ductile materials to combined stresses in two or three directions perpendicular to one another. *Journal of the Franklin Institute*, *189*(5), 627–640. https://doi.org/10.1016/S0016-0032(20)90373-3.

Zamel, N., & Li, X. (2006). Life cycle comparison of fuel cell vehicles and internal combustion engine vehicles for Canada and the United States. *Journal of Pow*er Sources, 162(2 SPEC. ISS.), 1241–1253. https://doi.org/10.1016/j.jpowsour.2006.08.007.

Appendix A – Thorough formulation of the forming limit diagram

A.1 – Mode I of fracture mechanics

In this analysis, the principal stress directions will be considered. However, to facilitate in terms of nomenclature, the in-plane principal stresses (acting tangent to the specimen surface) will be called σ_1 and σ_2, but since the stress normal to the surface is always 0 on a free surface, it cannot be called σ_3, but will rather be called $\sigma_t = 0$, even though it acts in a principal direction. This way, we have σ_1 and σ_2 properly defined considering the solid mechanics definition ($\sigma_1 > \sigma_2$), but σ_t is not necessarily smaller or larger than the others (see Figure 2.6).

Expressing the integrand, $\sigma_m/\bar{\sigma}$, and the variable of integration, $d\bar{\varepsilon}$, in the McClintock damage criterion in equation (2.9) as the product of three partial ratios involving the major principal stress, σ_1, and its correspondent strain increment, $d\varepsilon_1$, we get the following expression for the critical value of ductile damage for the mode I of fracture mechanics:

$$D_{crit} = \int_0^{\bar{\varepsilon}_f} \frac{\sigma_m}{\bar{\sigma}} \, d\bar{\varepsilon} = \int_0^{\varepsilon_{1f}} \frac{\sigma_m}{\sigma_1} \frac{\sigma_1}{\bar{\sigma}} \frac{d\bar{\varepsilon}}{d\varepsilon_1} \, d\varepsilon_1 \tag{A.1}$$

From Hill's (1948) anisotropic yield criterion, assuming plane stress, $\sigma_t = 0$, and rotational symmetry anisotropy, $r_\alpha = r = \bar{r}$, we get the constitutive equations in equation (A.2) and the equations for the effective stress and strain increment in equations (A.3) and (A.4), respectively.

$$d\varepsilon_1 = \frac{d\bar{\varepsilon}}{\bar{\sigma}} \left[\frac{1}{1+r} \right] [\sigma_1 + r(\sigma_1 - \sigma_2)]$$

$$d\varepsilon_2 = \frac{d\bar{\varepsilon}}{\bar{\sigma}} \left[\frac{1}{1+r} \right] [\sigma_2 + r(\sigma_2 - \sigma_1)] \tag{A.2}$$

$$\bar{\sigma} = \sqrt{\frac{3}{2} \frac{1}{(2+r)}} \sqrt{\sigma_1^2 + \sigma_2^2 + r(\sigma_1 - \sigma_2)^2}$$

$$= \sqrt{\frac{3}{2} \left(\frac{1+r}{2+r} \right)} \sqrt{\sigma_1^2 + \sigma_2^2 - \frac{2r\sigma_1\sigma_2}{1+r}} \tag{A.3}$$

$$d\bar{\varepsilon}^2 = \frac{2}{3} \frac{2+r}{(1+2r)^2} [(d\varepsilon_1 - rd\varepsilon_3)^2 + (d\varepsilon_2 - rd\varepsilon_3)^2 + r(d\varepsilon_1 - d\varepsilon_2)^2] \tag{A.4}$$

Using a condition of uniaxial loading, $\sigma_1 = \sigma_x = \bar{\sigma}$ and $\sigma_y = \sigma_z = \tau_{ij} = 0$, as a mean for simplification, equation (A.3) results in the following relation:

$$\frac{3}{2} \left(\frac{1+r}{2+r} \right) = 1 \tag{A.5}$$

Introducing the relation in equation (A.5) into equation (A.3), we get:

$$\bar{\sigma} = \sqrt{\sigma_1^2 + \sigma_2^2 - \frac{2r\sigma_1\sigma_2}{1+r}} \tag{A.6}$$

Assuming incompressibility, $d\varepsilon_1 + d\varepsilon_2 + d\varepsilon_3 = 0$, and after some mathematical manipulation, equation (A.4) results in the following one:

$$d\bar{\varepsilon} = \sqrt{\frac{2(2+r)(1+r)}{1+2r}}\sqrt{d\varepsilon_1^2 + d\varepsilon_2^2 + \frac{2r}{1+r}d\varepsilon_1 d\varepsilon_2} \tag{A.7}$$

Using the relation in equation (A.5) to simplify equation (A.7) we get:

$$d\bar{\varepsilon} = \frac{1+r}{\sqrt{1+2r}}\sqrt{d\varepsilon_1^2 + d\varepsilon_2^2 + \frac{2r}{1+r}d\varepsilon_1 d\varepsilon_2} \tag{A.8}$$

With some manipulation, the expressions in equation (A.2) result in the following ones:

$$(1+r)\frac{d\bar{\varepsilon}}{\bar{\sigma}} = \frac{(1+r)\sigma_1 - r\sigma_2}{d\varepsilon_1}$$

$$(1+r)\frac{d\bar{\varepsilon}}{\bar{\sigma}} = \frac{(1+r)\sigma_2 - r\sigma_1}{d\varepsilon_2} \tag{A.9}$$

Making the right-hand sides of both expressions in equation (A.9) equal and considering $\alpha = \sigma_2/\sigma_1$ and $\beta = d\varepsilon_2/d\varepsilon_1$, thus being defined as the slope of a general proportional strain loading path, we get:

$$\alpha = \frac{\sigma_2}{\sigma_1} = \frac{(1+r)\beta + r}{(1+r) + r\beta} \tag{A.10}$$

Combining equations (A.6) and (A.10), an expression for the major principal stress, σ_1, is obtained:

$$\sigma_1 = \frac{\bar{\sigma}}{\sqrt{1 - \frac{2r}{2+r}\alpha + \alpha^2}} \tag{A.11}$$

Since the hydrostatic stress is the average of the principal stresses and a condition of plane stress was assumed, $\sigma_m = (\sigma_1 + \sigma_2 + \sigma_3)/3 = (\sigma_1 + \alpha\sigma_1)/3$, the ratio σ_m/σ_1 results in:

$$\frac{\sigma_m}{\sigma_1} = \frac{(1+2r)(1+\beta)}{3[(1+r)+r\beta]} = \frac{1+\alpha}{3} \tag{A.12}$$

Combining, now, equation (A.11) with equation (A.10), an expression for the $\sigma_1/\bar{\sigma}$ is easily obtained:

$$\frac{\sigma_1}{\bar{\sigma}} = \frac{1}{\sqrt{1 - \frac{2r}{1+r}\alpha + \alpha^2}}$$

$$= \frac{(1+r) + r\beta}{\sqrt{[(1+r)+r\beta]^2 - \frac{2r}{1+r}[(1+r)+r\beta][(1+r)\beta + r] + [(1+r)\beta + r]^2}} \tag{A.13}$$

Expanding equation (A.13) in order to simplify it, results in equation (A.14).

$$\frac{\sigma_1}{\bar{\sigma}} = \frac{(1+r) + r\beta}{\sqrt{(1+r)^2 + 2r(1+r)\beta + r^2\beta^2 - 2r(1+r)\beta - 2r^2\beta^2 - 2r^2 - \frac{2r^3\beta}{1+r} + (1+r)^2\beta + 2(1+r)r\beta + r^2}}$$

$$\frac{\sigma_1}{\bar{\sigma}} = \frac{1}{\sqrt{1+2r}} \frac{(1+r) + r\beta}{\sqrt{1 + \frac{2r}{1+r}\beta + \beta^2}} \tag{A.14}$$

From equation (A.8), since $\beta = d\varepsilon_2/d\varepsilon_1$, we get:

$$\frac{d\bar{\varepsilon}}{d\varepsilon_1} = \frac{1+r}{\sqrt{1+2r}}\sqrt{1 + \frac{2r}{1+r}\beta + \beta^2} \tag{A.15}$$

Now, replacing all the three partial ratios, σ_m/σ_1, $\sigma_1/\bar{\sigma}$, and $d\bar{\varepsilon}/d\varepsilon_1$, that are obtained from equations (A.12), (A.14), and (A.15) into equation (A.1), we get an expression for the critical value of ductile damage for the mode I of fracture mechanics as follows:

$$D_{crit} = \int_0^{\varepsilon_{1f}} \frac{1+r}{3}(1+\beta)\,d\varepsilon_1 \tag{A.16}$$

Performing the integration in equation (A.16) and considering $\beta = d\varepsilon_2/d\varepsilon_1 = cte.$, the critical value of damage can be rewritten as follows:

$$D_{crit} = \frac{1+r}{3}(1+\beta)\varepsilon_{1f} = \frac{1+r}{3}\left(\varepsilon_{1f} + \varepsilon_{2f}\right) \tag{A.17}$$

If the lower limit in the integral in equation (A.16) was to be a threshold value of strain, $\bar{\varepsilon}_0$, rather than zero:

$$D_{crit} = \frac{1+r}{3}(1+\beta)\left(\varepsilon_{1f} - \varepsilon_0\right) = \frac{1+r}{3}\left[\varepsilon_{1f} + \varepsilon_{2f} - (1+\beta)\varepsilon_0\right] \tag{A.18}$$

A.2 – Mode II of fracture mechanics

Considering now the mode II of fracture mechanics, the McClintock damage criterion in equation (2.9) results in the following:

$$D_{crit}^s = \int_0^{\bar{\varepsilon}_f} \frac{\tau_{12}}{\bar{\sigma}}\,d\bar{\varepsilon} = \int_0^{\varepsilon_{1f}} \frac{\tau_{12}}{\bar{\sigma}}\frac{d\bar{\varepsilon}}{d\varepsilon_1}\,d\varepsilon_1 \tag{A.19}$$

Since $\tau_{12} = (\sigma_1 - \sigma_2)/2$, which results in $\tau_{12} = \sigma_1(1-\alpha)/2$, an expression for the partial ratio $\tau_{12}/\bar{\sigma}$ can be obtained from equation (A.14):

$$\frac{\tau_{12}}{\bar{\sigma}} = \frac{1-\alpha}{2}\frac{\sigma_1}{\bar{\sigma}} \tag{A.20}$$

Using equation (A.10) to have the ratio written as a function of the strain loading path rather than the stress ratio, α, equation (A.20) results in the following one:

$$\frac{\tau_{12}}{\bar{\sigma}} = \frac{1}{2}\frac{1}{\sqrt{1+2r}}\frac{1-\beta}{\sqrt{1+\frac{2r}{1+r}\beta+\beta^2}}$$

(A.21)

Hence, by introducing equation (A.21) into equation (A.19), the following expression for the McClintock ductile damage by in-plane shear is obtained:

$$D_{crit}^s = \int_0^{\varepsilon_{1f}}\frac{1}{2}\frac{1+r}{1+2r}(1-\beta)\,d\varepsilon_1$$

(A.22)

Performing the integration in equation (A.22) and considering $\beta = d\varepsilon_2/d\varepsilon_1 = cte.$, the value for the critical value of damage by in-plane shear can be written as in equation (A.23). Once again if a threshold value of strain is considered, equation (A.24) is obtained.

$$D_{crit}^s = \frac{1}{2}\frac{1+r}{1+2r}(1-\beta)\varepsilon_{1f} = \frac{1}{2}\frac{1+r}{1+2r}\left(\varepsilon_{1f}-\varepsilon_{2f}\right)$$

(A.23)

$$D_{crit}^s = \frac{1}{2}\frac{1+r}{1+2r}(1-\beta)\left(\varepsilon_{1f}-\varepsilon_0\right) = \frac{1}{2}\frac{1+r}{1+2r}\left[\varepsilon_{1f}-\varepsilon_{2f}-(1-\beta)\varepsilon_0\right]$$

(A.24)

A.3 – Mode III of fracture mechanics

For the case of mode III of fracture mechanics, the normalized maximum shear damage criterion is written as:

$$D_{crit}^{ts} = \int_0^{\bar{\varepsilon}_f}\frac{\tau_{ti}}{\bar{\sigma}}\,d\bar{\varepsilon} = \int_0^{\varepsilon_{1f}}\frac{\tau_{t1}}{\bar{\sigma}}\frac{d\bar{\varepsilon}}{d\varepsilon_1}\,d\varepsilon_1$$

(A.25)

Since plane stress, $\sigma_t = 0$, was assumed, the out-of-plane (or through-thickness) shear stress can be written as $\tau_{ti} = |\sigma_i - \sigma_t|/2 = |\sigma_i|/2$. From Figure 2.6, one can easily notice that from a state of pure shear to equibiaxial tension (tension dominated stress states), τ_{t1} dominates the out-of-plane shear and from equibiaxial compression to pure shear (compression dominated stress states), τ_{t2} does it. Hence, it is clear that the pure shear stress state representation as Mohr circles is a symmetry state, thus $(\tau_{t2})_{comp}\,d\varepsilon_2 = (|\sigma_2|/2)d\varepsilon_2 \equiv (\tau_{t1})_{tens}\,d\varepsilon_1 = (|\sigma_1|/2)d\varepsilon_1$ and an expression for the partial ratio $\tau_{t1}/\bar{\sigma}$ can be obtained from equation (A.14).

$$\frac{\tau_{t1}}{\bar{\sigma}} = \frac{1}{2}\frac{\sigma_1}{\bar{\sigma}} = \frac{1}{2\sqrt{1+2r}}\frac{(1+r)+r\beta}{\sqrt{1+\frac{2r}{1+r}\beta+\beta^2}}$$

(A.26)

Introducing this last expression in equation (A.25), allows for writing an expression for an adaptation of the McClintock ductile damage criterion to out-of-plane shear:

$$D_{crit}^{ts} = \int_0^{\varepsilon_{1f}}\frac{1}{2}\frac{1+r}{1+2r}[(1+r)+r\beta]\,d\varepsilon_1$$

(A.27)

Performing the integration in equation (A.27) and considering $\beta = d\varepsilon_2/d\varepsilon_1 = cte.$, the value for the critical value of damage by out-of-plane shear can be written as in equation (A.28). And if a threshold value of strain, $\bar{\varepsilon}_0$, is considered, equation (A.29) is obtained.

$$D_{crit}^{ts} = \frac{1}{2}\frac{1+r}{1+2r}[(1+r)+r\beta]\varepsilon_{1f} = \frac{1}{2}\frac{(1+r)^2}{1+2r}\left(\varepsilon_{1f}+\frac{r}{1+r}\varepsilon_{2f}\right)$$

(A.28)

$$D_{crit}^{ts} = \frac{1}{2}\frac{1+r}{1+2r}[(1+r)+r\beta](\varepsilon_{1f}-\varepsilon_0)$$

$$= \frac{1}{2}\frac{(1+r)^2}{1+2r}\left[\varepsilon_{1f} + \frac{r}{1+r}\varepsilon_{2f} - \left(1+\frac{r}{1+r}\beta\right)\varepsilon_0\right] \qquad (A.29)$$

It is also worth noting that by multiplying equation (A.12) by equation (A.14), an expression for stress triaxiality, $\eta = \sigma_m/\bar{\sigma}$, as a function of the anisotropy factor, r, and the strain loading path, β, is obtained:

$$\eta = \frac{\sqrt{1+2r}(1+\beta)}{3\sqrt{1+\frac{2r}{1+r}\beta+\beta^2}} \qquad (A.30)$$

A.4 – The normalized Cockcroft-Latham criterion

The normalized version of the Cockcroft and Latham (1968) ductile damage criterion proposed by Oh et al. (1979), stated in equation (2.8), can be rewritten as follows:

$$D_{crit}^{NCL} = \int_0^{\bar{\varepsilon}_f} \frac{\sigma_1}{\bar{\sigma}}d\bar{\varepsilon} = \int_0^{\varepsilon_{1f}} \frac{\sigma_1}{\bar{\sigma}}\frac{d\bar{\varepsilon}}{d\varepsilon_1}d\varepsilon_1 \qquad (A.31)$$

In this criterion the weighting function is given by $g = \sigma_1/\bar{\sigma}$, being thus the ratio represented in equation (A.14). Hence, the ratios $\sigma_1/\bar{\sigma}$ and $d\bar{\varepsilon}/d\varepsilon_1$ in equation (A.31) can be replaced by the expressions in equations (A.14) and (A.15), which will eventually result in:

$$D_{crit}^{NCL} = \int_0^{\varepsilon_{1f}} \frac{1+r}{1+2r}[(1+r)+r\beta]\,d\varepsilon_1$$

$$D_{crit}^{NCL} = \frac{1+r}{1+2r}[(1+r)+r\beta]\varepsilon_{1f} = \frac{(1+r)^2}{1+2r}\left(\varepsilon_{1f}+\frac{r}{1+r}\varepsilon_{2f}\right) \qquad (A.32)$$

Again, a strain threshold, $\bar{\varepsilon}_0$, may be considered for the lower integral limit in equation (A.32), that results in:

$$D_{crit}^{NCL} = \frac{1+r}{1+2r}[(1+r)+r\beta](\varepsilon_{1f}-\varepsilon_0)$$

$$= \frac{(1+r)^2}{1+2r}\left[\varepsilon_{1f}+\frac{r}{1+r}\varepsilon_{2f}-\left(1+\frac{r}{1+r}\beta\right)\varepsilon_0\right] \qquad (A.33)$$

Another way to write the normalized version of the Cockcroft and Latham (1968) ductile damage criterion is by writing it as a function of stress triaxiality, η, rather than the $\sigma_1/\bar{\sigma}$ ratio. To start, the $\sigma_1/\bar{\sigma}$ ratio may be acquired by dividing the stress triaxiality, $\eta = \sigma_m/\bar{\sigma}$, by the σ_1/σ_m ratio, i.e., equation (A.30) by equation (A.12):

$$\frac{\sigma_1}{\bar{\sigma}} = \frac{\eta}{\sigma_m/\sigma_1} = \frac{3[(1+r)+r\beta]}{(1+2r)(1+\beta)}\eta \qquad (A.34)$$

To fully write the $\sigma_1/\bar{\sigma}$ ratio in terms of stress triaxiality, η, the slope of strain loading path, β, must also be written in terms of η. This is achievable by inverting the expression in equation (A.30). Equations (A.35) to (A.52) provide the major steps in this transformation.

$$\frac{\sqrt{1+\frac{2r}{1+r}\beta+\beta^2}}{(1+\beta)}=\frac{\sqrt{1+2r}}{3\eta}\Rightarrow\frac{1+\frac{2r}{1+r}\beta+\beta^2}{(1+\beta)^2}=\frac{1+2r}{9\eta^2} \tag{A.35}$$

$$\frac{1+\frac{2r}{1+r}\beta+\beta^2}{1+2\beta+\beta^2}=1+\frac{\frac{2r}{1+r}-2}{1+2\beta+\beta^2}\beta=1+\frac{-2}{(1+\beta)^2(1+r)}\beta=\frac{1+2r}{9\eta^2} \tag{A.36}$$

$$\frac{2}{(1+\beta)^2}\beta=\left(1-\frac{1+2r}{9\eta^2}\right)(1+r)=\frac{(9\eta^2-1-2r)(1+r)}{9\eta^2} \tag{A.37}$$

$$\frac{(1+\beta)^2}{\beta}=\frac{18\eta^2}{(9\eta^2-1-2r)(1+r)} \tag{A.38}$$

$$\frac{1+2\beta+\beta^2}{\beta}=\frac{1}{\beta}+2+\beta=\frac{18\eta^2}{(9\eta^2-1-2r)(1+r)} \tag{A.39}$$

$$\beta+\frac{1}{\beta}=\frac{18\eta^2}{(9\eta^2-1-2r)(1+r)}-2=\frac{-18\eta^2r+2(1+2r)(1+r)}{9\eta^2(1+r)-(1+2r)(1+r)} \tag{A.40}$$

For simplification purposes, equation (A.40) can be rewritten into an expression whose inverse function is easier to obtain:

$$\beta+\frac{1}{\beta}=-2\frac{\frac{9\eta^2r}{(1+r)}-(1+2r)}{9\eta^2-(1+2r)}=f(\eta) \tag{A.41}$$

Multiplying equation (A.41) by β and taking all the terms to the left-hand side results in:

$$\beta^2-f(\eta)\times\beta+1=0 \tag{A.42}$$

Using the quadratic formula to calculate the roots of equation (A.42) provides an expression for β in terms of $f(\eta)$ that is represented in equation (A.43). By then substituting $f(\eta)$ inside the square root by the expression in terms of η given in equation (A.41), equation (A.44) is obtained. In order to treat the term in the square root independently for simplification purposes, the whole square root will be treated as a new function, A, as shown in equation (A.44).

$$\beta=\frac{f(\eta)\pm\sqrt{f(\eta)^2-4}}{2} \tag{A.43}$$

$$\beta=\frac{f(\eta)\pm\sqrt{\left(-2\frac{\frac{9\eta^2r}{(1+r)}-(1+2r)}{9\eta^2-(1+2r)}\right)^2-4}}{2}=\frac{f(\eta)}{2}\pm\frac{A}{2} \tag{A.44}$$

Equations (A.45) to (A.50) represent the major steps in the simplification of the square root term in equation (A.44), A.

$$A = \sqrt{\left(-2\frac{\dfrac{9\eta^2 r}{(1+r)} - (1+2r)}{9\eta^2 - (1+2r)}\right)^2 - 4} \tag{A.45}$$

$$= \sqrt{\frac{4\left(\dfrac{9\eta^2 r}{(1+r)}\right)^2 - 8\dfrac{9\eta^2 r}{(1+r)}(1+2r) + 4(1+2r)^2}{(9\eta^2)^2 - 2(1+2r)9\eta^2 + (1+2r)^2} - 4}$$

$$A = \sqrt{\frac{4\left(\dfrac{9\eta^2 r}{(1+r)}\right)^2 - 8\dfrac{9\eta^2 r}{(1+r)}(1+2r) - 4(9\eta^2)^2 + 8(1+2r)9\eta^2}{[9\eta^2 - (1+2r)]^2}} \tag{A.46}$$

$$A = \frac{\sqrt{9\eta^2\left(4\dfrac{9\eta^2 r^2}{(1+r)^2} - 8\dfrac{r}{(1+r)}(1+2r) - 4\times 9\eta^2 + 8(1+2r)\right)}}{9\eta^2 - (1+2r)} \tag{A.47}$$

$$A = \frac{3\eta\sqrt{4\dfrac{9\eta^2 r^2}{(1+r)^2} - 8\dfrac{r}{(1+r)}(1+2r) - 4\times 9\eta^2 + 8\dfrac{(1+r)}{(1+r)}(1+2r)}}{9\eta^2 - (1+2r)} \tag{A.48}$$

$$A = \frac{3\eta\sqrt{4\dfrac{9\eta^2 r^2}{(1+r)^2} - 4\dfrac{9\eta^2(1+r)^2}{(1+r)^2} + \dfrac{8}{(1+r)}(1+2r)}}{9\eta^2 - (1+2r)} \tag{A.49}$$

$$A = \frac{3\eta\sqrt{-4\left(\dfrac{9\eta^2(1+2r)}{(1+r)^2} - \dfrac{2}{(1+r)}(1+2r)\right)}}{9\eta^2 - (1+2r)} \tag{A.50}$$

$$= \frac{6\eta\sqrt{-\left(\dfrac{9\eta^2}{(1+r)^2} - \dfrac{2}{(1+r)}\right)(1+2r)}}{9\eta^2 - (1+2r)}$$

By now introducing the expression for $f(\eta)$ in the leftmost term of the right-hand side of equation (A.44) by the expression in equation (A.41) and also introducing the expression for A in equation (A.50), the slope of strain loading path, β, can finally be fully expressed in terms of stress triaxiality, η:

$$\beta = \frac{-2\left(\dfrac{9\eta^2 r}{(1+r)} - (1+2r)\right) \pm 6\eta\sqrt{-\left(\dfrac{9\eta^2}{(1+r)^2} - \dfrac{2}{(1+r)}\right)(1+2r)}}{2\left(9\eta^2 - (1+2r)\right)} \tag{A.51}$$

Since, for current bulk and sheet formability tests, the strain loading path varies between uniaxial compression and equibiaxial tension, its slope varies as $-2 \leq \beta \leq 1$ with the stress triaxiality varying as $-1/3 \leq \eta \leq 2/3$. This is only achieved when considering the subtraction of the root squared term in the previous equation, as can be perceived from Figure A.1; in fact this is the only way to get a strain loading path $\beta = 1$ to correspond to a stress triaxiality state of $\eta = 2/3$. Hence, β is now written as in equation (A.52).
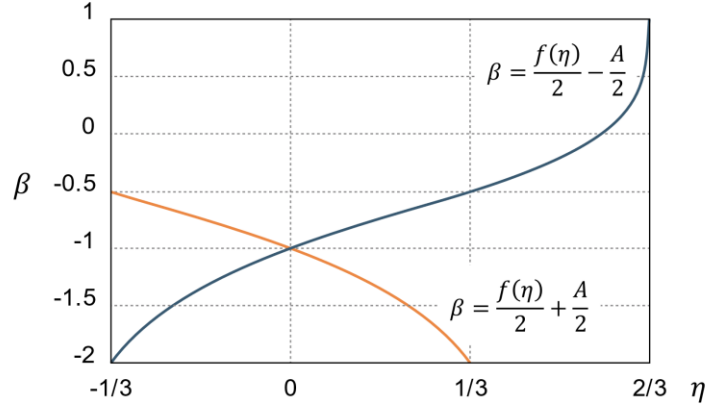
Figure A.1 *Graphical representation of the variation of the roots of equation (A.42) with η, using the notation introduced in equation (A.44) and considering isotropy ($r = 1$).*

$$\beta = \frac{-2\left(\frac{9\eta^2 r}{(1+r)} - (1+2r)\right) - 6\eta\sqrt{-\left(\frac{9\eta^2}{(1+r)^2} - \frac{2}{(1+r)}\right)(1+2r)}}{2(9\eta^2 - (1+2r))} \tag{A.52}$$

This expression may now be introduced into equation (A.34) to write the $\sigma_1/\bar{\sigma}$ ratio as a function of stress triaxiality, η:

$$\frac{\sigma_1}{\bar{\sigma}} = \frac{3\left((1+r) + r\dfrac{-2\left(\frac{9\eta^2 r}{(1+r)} - (1+2r)\right) - 6\eta\sqrt{-\left(\frac{9\eta^2}{(1+r)^2} - \frac{2}{(1+r)}\right)(1+2r)}}{2(9\eta^2 - (1+2r))}\right)}{(1+2r)\left(1 + \dfrac{-2\left(\frac{9\eta^2 r}{(1+r)} - (1+2r)\right) - 6\eta\sqrt{-\left(\frac{9\eta^2}{(1+r)^2} - \frac{2}{(1+r)}\right)(1+2r)}}{2(9\eta^2 - (1+2r))}\right)}\eta \tag{A.53}$$

Appendix B – Obtaining the Lode parameters via geometric analysis

B.1 – The Lode coefficient

From Lode's (1926) original work, the Lode coefficient may be defined as a way to analyze the influence of the intermediate principal stress component, σ_2, on yielding according to Tresca's and von Mises' yield criteria:

$$\sigma_2 = \frac{\sigma_1 + \sigma_3}{2} + \mu \frac{\sigma_1 - \sigma_3}{2} \tag{B.1}$$

$$\mu = \frac{\sigma_2 - \frac{1}{2}(\sigma_1 + \sigma_3)}{\frac{1}{2}(\sigma_1 - \sigma_3)} = \frac{2\sigma_2 - \sigma_1 - \sigma_3}{\sigma_1 - \sigma_3} = \frac{2\sigma_2 - \sigma_3}{\sigma_1 - \sigma_3} - 1 \tag{B.2}$$

Considering the notation introduced in Figure 2.11 (Section 2.2.6), equation (B.2) may be rewritten as follows:

$$\mu = \frac{\sigma_2 - \sigma_{13}}{\tau_{13}} \tag{B.3}$$

For the case of the von Mises' yield criterion, the effective stress, $\bar{\sigma}$, is written as in equation (B.4). Following Mendelson's (1986) procedure, equation (B.1) can be introduced into equation (B.4), as shown in equation (B.5), and after some manipulation equation (B.6) is obtained.

$$\bar{\sigma} = \frac{1}{\sqrt{2}}[(\sigma_1 - \sigma_2)^2 + (\sigma_2 - \sigma_3)^2 + (\sigma_3 - \sigma_1)^2]^{\frac{1}{2}} \tag{B.4}$$

$$\bar{\sigma} = \frac{1}{\sqrt{2}}\left[\left(\sigma_1 - \frac{\sigma_1 + \sigma_3}{2} + \mu\frac{\sigma_1 - \sigma_3}{2}\right)^2 + \left(\frac{\sigma_1 + \sigma_3}{2} + \mu\frac{\sigma_1 - \sigma_3}{2} - \sigma_3\right)^2 + (\sigma_3 - \sigma_1)^2\right]^{\frac{1}{2}} \tag{B.5}$$

$$\frac{\sigma_1 - \sigma_3}{\bar{\sigma}} = \frac{2}{\sqrt{3 + \mu^2}} \tag{B.6}$$

Since the principal stress components, σ_i, can be written in terms of the hydrostatic stress, σ_m, and the principal deviatoric stress components, σ_i', as $\sigma_i = \sigma_m + \sigma_i'$ (with $i = 1,2,3$), the introduction of the Lode coefficient as defined in equations (B.1) and (B.2) results in the following:

$$\sigma_1 = \sigma_m + \sigma_1' = \sigma_m + \frac{2\sigma_1 - \sigma_2 - \sigma_3}{3} = \sigma_m + \frac{3(\sigma_1 - \sigma_3) - \mu(\sigma_1 - \sigma_3)}{6} \tag{B.7}$$

$$\sigma_2 = \sigma_m + \sigma_2' = \sigma_m + \frac{2\sigma_2 - \sigma_1 - \sigma_3}{3} = \sigma_m + \frac{\mu(\sigma_1 - \sigma_3)}{3} \tag{B.8}$$

$$\sigma_3 = \sigma_m + \sigma_3' = \sigma_m + \frac{2\sigma_3 - \sigma_1 - \sigma_2}{3} = \sigma_m - \frac{3(\sigma_1 - \sigma_3) + \mu(\sigma_1 - \sigma_3)}{6} \tag{B.9}$$

By now introducing the relation in equation (B.6) into equations (B.7) to (B.9), and recalling that the stress triaxiality is defined as $\eta = \sigma_m/\bar{\sigma}$, the principal stress components may be expressed in terms of the stress triaxiality, η, the Lode coefficient, μ, and the effective stress, $\bar{\sigma}$, as follows:

$$\sigma_1 = \sigma_m + \frac{(3-\mu)\bar{\sigma}}{3\sqrt{3+\mu^2}} = \left(\eta + \frac{(3-\mu)}{3\sqrt{3+\mu^2}} \right)\bar{\sigma} \tag{B.10}$$

$$\sigma_2 = \sigma_m + \frac{2\mu\bar{\sigma}}{3\sqrt{3+\mu^2}} = \left(\eta + \frac{2\mu}{3\sqrt{3+\mu^2}} \right)\bar{\sigma} \tag{B.11}$$

$$\sigma_3 = \sigma_m - \frac{(3+\mu)\bar{\sigma}}{3\sqrt{3+\mu^2}} = \left(\eta - \frac{(3+\mu)}{3\sqrt{3+\mu^2}} \right)\bar{\sigma} \tag{B.12}$$

B.2 – The Lode angle and the Lode angle parameter

Considering the representation of a given stress state, P, in the Haigh-Westergaard stress space (Figure 2.12a), the magnitude of the hydrostatic stress state vector, $|ON|$, is simply written as:

$$|ON| = \frac{1}{\sqrt{3}}\sigma_1 + \frac{1}{\sqrt{3}}\sigma_2 + \frac{1}{\sqrt{3}}\sigma_3 = \sqrt{3}\sigma_m = \frac{I_1}{\sqrt{3}} \tag{B.13}$$

And the magnitude of the deviatoric stress vector, $|OS| = |NP|$ can be expressed as follows:

$$|PN| = \sqrt{|OP|^2 - |ON|^2} = \sqrt{(\sigma_1^2 + \sigma_2^2 + \sigma_3^2) - 3\sigma_m^2}$$

$$= \sqrt{(\sigma_1 - \sigma_m)^2 + (\sigma_2 - \sigma_m)^2 + (\sigma_3 - \sigma_m)^2} \tag{B.14}$$

$$= \sqrt{\sigma_1'^2 + \sigma_2'^2 + \sigma_3'^2} = \sqrt{2J_2}$$

Another way to obtain the magnitude of the deviatoric stress vector, $|PN|$, is by considering the projection of point P on the π-plane, where the principal stress σ_1 is at -30⁰ from a horizontal line (Figure 2.12b), and follow Mendelson's (1986) approach, in which one starts by expressing the projections of P onto the horizontal line, a, and onto the vertical axis (σ_2), b.

$$a = \sqrt{\frac{2}{3}}\sigma_1 \cos 30° - \sqrt{\frac{2}{3}}\sigma_3 \cos 30° = \frac{\sigma_1 - \sigma_3}{\sqrt{2}} \tag{B.15}$$

$$b = \sqrt{\frac{2}{3}}\sigma_2 - \sqrt{\frac{2}{3}}\sigma_1 \sin 30° - \sqrt{\frac{2}{3}}\sigma_3 \sin 30° = \frac{2\sigma_2 - \sigma_1 - \sigma_3}{\sqrt{6}} \tag{B.16}$$

Now, the magnitude of the deviatoric stress vector may be calculated as:

$$|PN| = \sqrt{a^2 - b^2} = \sqrt{\frac{(\sigma_1 - \sigma_3)^2}{2} + \frac{(2\sigma_2 - \sigma_1 - \sigma_3)^2}{6}}$$

$$= \sqrt{\frac{2}{3}\sigma_1^2 + \frac{2}{3}\sigma_2^2 + \frac{2}{3}\sigma_3^2 - \frac{2}{3}\sigma_1\sigma_3 - \frac{2}{3}\sigma_1\sigma_2 - \frac{2}{3}\sigma_2\sigma_3} \tag{B.17}$$

$$= \sqrt{(\sigma_1^2 + \sigma_2^2 + \sigma_3^2) - 3\sigma_m^2} = \sqrt{2J_2}$$

This approach also makes it possible for an easier obtainment of the angle between the deviatoric stress vector and the σ_1 axis on the π-plane, θ. By noting the relation between a and b, and introducing the Lode coefficient definition in equation (B.2), one obtains equation (B.18). By, now, calculating θ as $\theta = (\tan^{-1}(b/a) + 30°)$, equation (B.20) is obtained:

$$\frac{b}{a} = \sqrt{\frac{1}{3}\frac{2\sigma_2 - \sigma_1 - \sigma_3}{\sigma_1 - \sigma_3}} = \sqrt{\frac{1}{3}}\mu \tag{B.18}$$

$$\theta = \tan^{-1}\left(\frac{b}{a}\right) + 30° \Rightarrow \tan\theta = \frac{\frac{1}{\sqrt{3}}\mu + \frac{1}{\sqrt{3}}}{1 - \frac{\mu}{3}} \tag{B.19}$$

$$\tan\theta = \frac{\sqrt{3}(\mu + 1)}{3 - \mu} \tag{B.20}$$

where θ is the positive Lode angle.

Equation (B.22) presents the characteristic polynomial of the deviatoric stress tensor, σ'_{ij}, in terms of its invariants, presented in equation (B.21).

$$\begin{cases} J_1 = \sigma'_1 + \sigma'_2 + \sigma'_3 = 0 \\ J_2 = \frac{1}{2}\left(\sigma'^2_1 + \sigma'^2_2 + \sigma'^2_3\right) \\ J_3 = \sigma'_1\sigma'_2\sigma'_3 \end{cases} \tag{B.21}$$

$$|\sigma'_{ij} - s\delta_{ij}| = 0$$
$$\Rightarrow s^3 - J_1 s^2 - J_2 s - J_3 = s^3 - J_2 s - J_3 = 0 \tag{B.22}$$

where $\delta_{ij} = \begin{cases} 0, & i \neq j \\ 1, & i = j \end{cases}$ is the Kronecker delta and s represents the eigenvalues of the deviatoric stress tensor, i.e., the principal deviatoric stress components.

Considering the trigonometric identity in equation (B.23) and following Chen's (1982) analysis, from the representation of the stress state on the π-plane (Figure 2.12b), s can be defined as in equation (B.24) (in which $\rho = \sqrt{2/3}\,|PN|$ is used just for simplification of following calculations) and introduced into equation (B.22), resulting in equation (B.25).

$$\cos 3\theta = 4\cos^3\theta - 3\cos\theta$$
$$\Rightarrow \cos^3\theta - \frac{3}{4}\cos\theta - \frac{1}{4}\cos 3\theta = 0 \tag{B.23}$$

$$s \equiv s_1 = \sigma'_1 = \rho\cos\theta = \sqrt{\frac{2}{3}}|PN|\cos\theta \tag{B.24}$$

$$\rho^3\cos^3\theta - J_2\rho\cos\theta - J_3 = \cos^3\theta - \frac{J_2}{\rho^2}\cos\theta - \frac{J_3}{\rho^3} = 0 \tag{B.25}$$

Comparing the terms in equations (B.23) and (B.25), we can once again obtain the expression for the magnitude of the deviatoric stress vector, $|PN|$, and for $\cos 3\theta$:

$$\frac{J_2}{\rho^2} = \frac{3}{4} \Rightarrow \rho = \frac{2\sqrt{J_2}}{\sqrt{3}} = \sqrt{\frac{2}{3}}|PN| \tag{B.26}$$

$$\Rightarrow |PN| = \sqrt{2J_2}$$

$$\frac{J_3}{\rho^3} = \frac{1}{4}\cos 3\theta \tag{B.27}$$

Introducing the result of equation (B.26) into equation (B.27):

$$\cos 3\theta = 4\frac{J_3}{\rho^3} = \frac{3\sqrt{3}}{2}\frac{J_3}{J_2^{3/2}} \tag{B.28}$$

This last parameter is referred to as the normalized third deviatoric stress invariant, or Lode angle parameter, ξ:

$$\xi = \cos 3\theta = \frac{3\sqrt{3}}{2}\frac{J_3}{J_2^{3/2}} \tag{B.29}$$

B.3 – Relating the Lode parameters to stress triaxiality

The second invariant of the deviatoric stress tensor, J_2, may also be written as:

$$J_2 = \frac{1}{6}[(\sigma_1 - \sigma_2)^2 + (\sigma_2 - \sigma_3)^2 + (\sigma_3 - \sigma_1)^2] = \frac{\bar{\sigma}^2}{3}$$
$$\Rightarrow \bar{\sigma} = \sqrt{3J_2} \tag{B.30}$$

Hence, the Lode angle parameter in equation (B.29) may rewritten as:

$$\xi = \cos 3\theta = \frac{27}{2}\frac{J_3}{\bar{\sigma}} \tag{B.31}$$

If plane stress, $\sigma_3 = 0$, is assumed (reasonable for sheet forming or for free surfaces in bulk forming), the third invariant of the deviatoric stress tensor, J_3, may be expressed as follows:

$$J_3 = -\sigma_m(\sigma_1 - \sigma_m)(\sigma_2 - \sigma_m) = -\sigma_m(\sigma_1\sigma_2 - \sigma_1\sigma_m - \sigma_2\sigma_m + \sigma_m^2)$$

$$\text{or, } J_3 = -\sigma_m\left[\sigma_m^2 - \frac{1}{3}\frac{1}{2}(\sigma_1^2 + \sigma_2^2 + \sigma_1^2 - 2\sigma_1\sigma_2 + \sigma_2^2)\right] \tag{B.32}$$

$$\Rightarrow J_3 = -\sigma_m\left[\sigma_m^2 - \frac{1}{3}\frac{1}{2}[\sigma_1^2 + \sigma_2^2 + (\sigma_1 - \sigma_2)^2]\right]$$

Considering von Mises' yield criterion, equation (B.32) results in equation (B.33), that can be introduced into equation (B.31), resulting in a relation between the Lode angle parameter, ξ, and the stress triaxiality, η, as in equation (B.34).

$$J_3 = -\sigma_m\left(\sigma_m^2 - \frac{1}{3}\bar{\sigma}\right) = -\eta\left(\eta^2 - \frac{1}{3}\right)\bar{\sigma} \tag{B.33}$$

$$\xi = \cos 3\theta = -\frac{27}{2}\eta\left(\eta^2 - \frac{1}{3}\right) \tag{B.34}$$

B.4 – Relating the Lode parameters to the normalized maximum shear stress

From equations (B.28) and (B.30) results $\rho = (2/3)\bar{\sigma}$, which can be introduced in the calculation of the principal deviatoric stress components when considering the π-plane in Figure 2.12b:

$$\sigma_1' = \rho\cos\theta = \frac{2}{3}\bar{\sigma}\cos\theta \tag{B.35}$$

$$\sigma_2' = \rho \cos\left(\frac{2}{3}\pi - \theta\right) = \frac{2}{3}\bar{\sigma}\cos\left(\frac{2}{3}\pi - \theta\right) \tag{B.36}$$

$$\sigma_3' = \rho \cos\left(\frac{2}{3}\pi + \theta\right) = \frac{2}{3}\bar{\sigma}\cos\left(\frac{2}{3}\pi + \theta\right) \tag{B.37}$$

Following the work by Bai and Wierzbicki (2010), and writing the principal stress components as $\sigma_i = \sigma_m + \sigma_i'$ (with $i = 1,2,3$), these can be expressed as:

$$\sigma_1 = \sigma_m + \frac{2}{3}\bar{\sigma}\cos\theta = \sigma_m\left(1 + \frac{2}{3\eta}\cos\theta\right)$$
$$\text{or, } \sigma_1 = \bar{\sigma}\left(\eta + \frac{2}{3}\cos\theta\right) \tag{B.38}$$

$$\sigma_2 = \sigma_m + \frac{2}{3}\bar{\sigma}\cos\left(\frac{2}{3}\pi - \theta\right) = \sigma_m\left[1 + \frac{2}{3\eta}\cos\left(\frac{2}{3}\pi - \theta\right)\right]$$
$$\text{or, } \sigma_2 = \bar{\sigma}\left[\eta + \frac{2}{3}\cos\left(\frac{2}{3}\pi - \theta\right)\right] \tag{B.39}$$

$$\sigma_3 = \sigma_m + \frac{2}{3}\bar{\sigma}\cos\left(\frac{2}{3}\pi + \theta\right) = \sigma_m\left[1 + \frac{2}{3\eta}\cos\left(\frac{2}{3}\pi - \theta\right)\right]$$
$$\text{or, } \sigma_3 = \bar{\sigma}\left[\eta + \frac{2}{3}\cos\left(\frac{2}{3}\pi + \theta\right)\right] \tag{B.40}$$

Following the approach of Lou et al. (2012), by considering, now, Tresca's yield criterion, $\tau_{max} = (\sigma_1 - \sigma_3)/2$, and introducing equations (B.38) and (B.40), the normalized maximum shear stress, $2\tau_{max}/\bar{\sigma}$, can be written as:

$$\frac{2\tau_{max}}{\bar{\sigma}} = \frac{\sigma_1 - \sigma_3}{\bar{\sigma}} = \frac{2}{3}\left[\cos\theta - \cos\left(\frac{2}{3}\pi + \theta\right)\right] \tag{B.41}$$

From equation (B.34), the Lode angle can be written as:

$$\theta = \frac{\cos^{-1}\left(-\frac{27}{2}\eta\left(\eta^2 - \frac{1}{3}\right)\right)}{3} \tag{B.42}$$

This way, the normalized maximum shear stress can also be written in terms of stress triaxiality as follows:

$$\frac{2\tau_{max}}{\bar{\sigma}} = \frac{2}{3}\left\{\cos\left[\frac{1}{3}\cos^{-1}\left(-\frac{27}{2}\eta\left(\eta^2 - \frac{1}{3}\right)\right)\right]\right.$$
$$\left. - \cos\left[\frac{2}{3}\pi + \frac{1}{3}\cos^{-1}\left(-\frac{27}{2}\eta\left(\eta^2 - \frac{1}{3}\right)\right)\right]\right\} \tag{B.43}$$

B.5 – Relating the Lode parameters to the normalized major principal stress component

Manipulating equation (B.38) allows for writing the $\sigma_1/\bar{\sigma}$ ratio, or the normalized major principal stress component, in terms of both stress triaxiality and the Lode angle, θ (B.44). This expression can be further handled to write the $\sigma_1/\bar{\sigma}$ ratio in terms of the normalized Lode angle, $\bar{\theta}$, or the Lode angle parameter, ξ (B.45).

$$\frac{\sigma_1}{\bar{\sigma}} = \eta + \frac{2}{3}\cos\theta \tag{B.44}$$

$$\frac{\sigma_1}{\bar{\sigma}} = \eta + \frac{2}{3}\cos\left[\frac{\pi}{6}(1-\bar{\theta})\right] = \eta + \frac{2}{3}\cos\left(\frac{\cos^{-1}\xi}{3}\right) \tag{B.45}$$

Because $\xi = f(\eta)$ is a non-invertible function, equation (B.45) can never be fully written solely in terms of either Lode parameter, being this its final form.